# Investigations of Heat Transfer and Fluid Flow in the Pocket Region of a Gas Turbine Engine and Cooling of a Turbine Blade

Liu, Jian

2019

*Document Version:*
Publisher's PDF, also known as Version of record

# Investigations of Heat Transfer and Fluid Flow in the Pocket Region of a Gas Turbine Engine and Cooling of a Turbine Blade

Jian Liu

DOCTORAL DISSERTATION
by due permission of the Faculty of Engineering at Lund University, will be publicly defenced on Friday 17 May 2019, at 10:15 a.m. in Lecture Hall E in the M-building, Ole Römers väg 1, Lund, Sweden.

**Faculty opponent**
Professor Björn Laumert
KTH, School of Industrial Engineering and Management (ITM)
Energy Technology, Heat and Power Technology

| Organization | Document name |
|---|---|
| LUND UNIVERSITY | DOCTORAL DISSERTATION |
| | Date of issue<br>March 18, 2019 |
| Author(s)<br>Jian Liu | Sponsoring organization<br>China Scholarship Council (CSC) |


Title and subtitle

**Investigations of Heat Transfer and Fluid Flow in the Pocket Region of a Gas Turbine Engine and Cooling of a Turbine Blade**


Abstract

In the present work, heat transfer within gas turbine applications are investigated both experimentally and numerically. The main content concerns heat transfer and fluid flow over the pocket region and cooling of a turbine blade.

A pocket cavity is generated at the junction part of the low pressure turbine (LPT) and the outlet guide vane (OGV) in the rear part of a gas turbine engine. The heat transfer distribution and fluid flow over the pocket cavity have significant effects on the incoming flow of the OGV placed downstream. These pocket cavities are built with different radii to find out improved heat transfer distributions and flow patterns. The effects of a pocket cavity on heat transfer and flow characteristics onthe endwall with a symmetric vane are also investigated. The relative location between the pocket cavity and the symmetric vane is varied. In addition, the effect of incoming flow attack angle of the pocket cavity upstream of an OGV is investigated numerically. Liquid Crystal Thermography (LCT) is employed to measure the heat transfer of the tested surfaces. The results show that the smaller fillet radius provides a higher heat transfer peak value with a stronger recirculating flow inside the pocket cavity. When a pocket cavity is placed upstream of the symmetric vane, the high heat transfer areas around the symmetric vane are decreased. The attack angles of the incoming flow over the pocket cavity affect the forming of horseshoe vortices in leading edge of the vane and then affect the heat transfer distribution.

Rib turbulators are widely employed in internal cooling passages of a turbine blade. Firstly, truncated ribs with various truncation types and arrangements are considered. Secondly, perforated ribs with differently shaped penetration holes and perforation ratios are investigated. LCT is employed to measure surface temperature and derive heat transfer coefficients over the ribbed surfaces in the tested channels. The turbulent flow details are presented by numerical calculations with an established turbulence model, i.e., the k-ω SST model. From the results, the truncated ribs can reduce the pressure loss penalty without reducing the heat transfer enhancement. By changing the configurations to staggered arrangements, the heat transfer can be further enhanced associated with a moderate pressure drop. By using perforated ribs, the low heat transfer regions downstream of the rib rows are greatly improved.

Endwall film cooling is a significant cooling method to protect the endwall region where the flow structures are complex due to horseshoe vortices and generated secondary flows. This study firstly concentrates on film cooling holes arranged upstream of the leading edge of a turbine vane. Several arrangements are designed aiming at improving the coolant coverage. Based on the calculated results, the film cooling holes upstream the leading edge have cooling effects on both the vane surfaces and the endwall. A case with two rows of compound angle holes in staggered arrangement shows relatively high overall averaged cooling effectiveness independent of the blowing ratios. Then full-scale endwall film cooling is also investigated in this study. The film holes arrangements are designed based on the pressure coefficient distribution, streamline distribution and heat transfer distribution on the endwall. With compound angle holes, the design based on the pressure distribution forces the flows to the suction side, which creates benefits for cooling the vane surfaces. The design based on the streamline distribution has more uniform coolant coverage on the endwall. The design based on the heat transfer distributions has relatively large coolant coverage and is effective in removing the high temperature region.



Key words:

pocket cavity, symmetrical vane, Liquid Crystal Thermography, truncated ribs, staggered arrangement, perforated ribs, secondary flows, endwall film cooling, leading edge, turbine vane, coolant coverage

Classification system and/or index terms (if any)

| Supplementary bibliographical information | | Language<br>English |
|---|---|---|
| ISSN and key title<br>ISRN: LUTMDN/TMHP-19/1144-SE<br>ISSN: 0282-1990 | | ISBN<br>978-91-7895-038-6 (print)<br>978-91-7895-039-3 (pdf) |
| Recipient's notes | Number of pages 79 | Price |
| | Security classification | |




Signature 刘建 Date March 18, 2019

# Investigations of Heat Transfer and Fluid Flow in the Pocket Region of a Gas Turbine Engine and Cooling of a Turbine Blade

Doctoral Dissertation

Jian Liu


LUND UNIVERSITY

Thesis for the degree of Doctor of Philosophy in Engineering.



Division of Heat Transfer
Department of Energy Sciences
Faculty of Engineering (LTH)
Lund University
Box 118
SE-221 00 LUND
SWEDEN

ISBN: 978-91-7895-038-6 (print)
ISBN: 978-91-7895-039-3 (pdf)
ISRN: LUTMDN/TMHP-19/1144-SE
ISSN: 0282-1990

# Popular Science

Gas turbines have been widely used in aircraft engines, warship engines and for land-based power generation for many years. The efficiency of gas turbines is directly related to the turbine inlet temperature (TIT). Engines usually increase the turbine efficiency by increasing the TIT, which has already exceeded the melting point of turbine components, especially for turbine blades. Nowdays, heat transfer and fluid flow in a gas turbine is still an important issue receiving considerable attention. In the newly designed gas turbines, one usually searched for high turbine efficiency which brings high design requirements for heat transfer components and cooling structures. In the future, hydrogen-rich fuels maybe used in gas turbines to reduce carbon dioxide emissions. Then higher exhaust gas temperature can be found at the inlet of nozzle guide vanes. Accordingly, more effective and complex cooling systems are needed.

Research works on gas turbine heat transfer to increase efficiency usually contains two aspects, using advanced materials and searching for optimized heat transfer structures. A better understanding of fundamental heat transfer around the vane within a gas turbine is necessary before an optimization design process. Heat transfer within a gas turbine is complex due to the extremely severe flow conditions. So for instance, high turbulence intensity of the exhaust gas, flow separation and transitions on the suction side, wake flows, flow accelerations and secondary flows on the endwall all increase the complexity of heat transfer around a turbine blade. Turbine blades are cooled both internally and externally. Internal cooling mainly contains three aspects, impingement cooling at the leading edge, ribbed turbulators in the middle, pin-fins in the trailing edge. The coolant, which is directly taken from the compressor of the gas turbine, goes through serpentine passages. The coolant ejected from the holes on the blades surface, endwall and protecting adjacent regions creates external cooling, also called film cooling.

This work contains two parts, heat transfer and fluid flow in the pocket region of a gas turbine engine and cooling of a turbine blade. For the first part, the effect of fillet radii of the pocket cavity, the effect of relative location between the pocket and the vane, flow attack angle are investigated. The research works present heat transfer and fluid flow details in the pocket region in the rear part of a gas turbine. For the second part, i.e., cooling of a turbine blade, internal cooling using ribbed channels and endwall film cooling are both included in this thesis. Some newly cooling structures and cooling design ideas are proposed in this part aiming to improve the cooling efficiency of a turbine blade.

# Abstract

In the present work, heat transfer within gas turbine applications are investigated both experimentally and numerically. The main content concerns heat transfer and fluid flow over the pocket region and cooling of a turbine blade.

A pocket cavity is generated at the junction part of the low pressure turbine (LPT) and the outlet guide vane (OGV) in the rear part of a gas turbine engine. The heat transfer distribution and fluid flow over the pocket cavity have significant effects on the incoming flow of the OGV placed downstream. These pocket cavities are built with different radii to find out improved heat transfer distributions and flow patterns. The effects of a pocket cavity on heat transfer and flow characteristics onthe endwall with a symmetric vane are also investigated. The relative location between the pocket cavity and the symmetric vane is varied. In addition, the effect of incoming flow attack angle of the pocket cavity upstream of an OGV is investigated numerically. Liquid Crystal Thermography (LCT) is employed to measure the heat transfer of the tested surfaces. The results show that the smaller fillet radius provides a higher heat transfer peak value with a stronger recirculating flow inside the pocket cavity. When a pocket cavity is placed upstream of the symmetric vane, the high heat transfer areas around the symmetric vane are decreased. The attack angles of the incoming flow over the pocket cavity affect the forming of horseshoe vortices in leading edge of the vane and then affect the heat transfer distribution.

Rib turbulators are widely employed in internal cooling passages of a turbine blade. Firstly, truncated ribs with various truncation types and arrangements are considered. Secondly, perforated ribs with differently shaped penetration holes and perforation ratios are investigated. LCT is employed to measure surface temperature and derive heat transfer coefficients over the ribbed surfaces in the tested channels. The turbulent flow details are presented by numerical calculations with an established turbulence model, i.e., the $k$-$\omega$ SST model. From the results, the truncated ribs can reduce the pressure loss penalty without reducing the heat transfer enhancement. By changing the configurations to staggered arrangements, the heat transfer can be further enhanced associated with a moderate pressure drop. By using perforated ribs, the low heat transfer regions downstream of the rib rows are greatly improved.

Endwall film cooling is a significant cooling method to protect the endwall region where the flow structures are complex due to horseshoe vortices and generated secondary flows. This study firstly concentrates on film cooling holes arranged upstream of the leading edge of a turbine vane. Several arrangements are designed aiming at improving the coolant coverage. Based on the calculated results, the film cooling holes upstream the leading edge have cooling effects on both the vane surfaces and the endwall. A case with two rows of compound angle holes in staggered

arrangement shows relatively high overall averaged cooling effectiveness independent of the blowing ratios. Then full-scale endwall film cooling is also investigated in this study. The film holes arrangements are designed based on the pressure coefficient distribution, streamline distribution and heat transfer distribution on the endwall. With compound angle holes, the design based on the pressure distribution forces the flows to the suction side, which creates benefits for cooling the vane surfaces. The design based on the streamline distribution has more uniform coolant coverage on the endwall. The design based on the heat transfer distributions has relatively large coolant coverage and is effective in removing the high temperature region.

**Keywords:** pocket cavity, symmetric vane, Liquid Crystal Thermography, truncated ribs, staggered arrangement, perforated ribs, secondary flows, endwall film cooling, leading edge, turbine vane, coolant coverage

# Acknowledgments

This research work has been carried out at the Division of Heat Transfer, Department of Energy Sciences at Lund University, Lund, Sweden.

Firstly, I want to give my great appreciation to my main supervisor, Professor Bengt Sundén, for providing me the opportunity to perform my PhD study at the Department of Energy Sciences at Lund University. His guidance and kindness make me feel comfortable to carry out research in our division. I also express my gratitude to my co-supervisors Lei Wang and Gongnan Xie. They have given me some guidance and support in my research during the past four years.

In addition, I should express thanks to my colleagues in our division, especially the PhD colleagues, Chenglong Wang, Jiatang Wang and Safeer Hussain, who have helped me a lot in the research and life. Many thanks are also given to the staff and administrators at the Department of Energy Sciences.

I want to thank the visiting PhD students, Wei Wang and Wei Du, for the help when we share the same office. Thank you to all colleagues and friends in the Department of Energy Sciences. I really had a good time during the PhD life in the department.

I want to express my great appreciations to my friends, Xiuqin Zhong, and other friends in Lund who give a lot of happiness and help during the past four years.

Finally, special thanks to my family members, my parents Jiagui Liu and Dianguo Lu, My sister Manman Liu, for their support at any time.

I acknowledge the Swedish Research Council (VR), GKN Aerospace Engine Systems and Siemens Industrial Turbomachinery and the China Scholarship Council (CSC) for the financial support.

# List of Publications

**Publications included in this thesis:**

**I.** **J. Liu**, S. Hussain, L. Wang, G. Xie, B. Sundén, Heat transfer and turbulent flow characteristics over pocket cavity in the junction part of an outlet guide vane in a gas turbine, Applied Thermal Engineering 124 (2017) 831-843.

**II.** **J. Liu**, S. Hussain, W. Wang, L. Wang, G. Xie, B. Sundén, Effect of the relative location of a pocket cavity on heat transfer and flow structures of the downstream endwall with a symmetrical vane, submitted to International Journal of Thermal Sciences, under review.

**III.** **J. Liu**, S. Hussain, C. Wang, L. Wang, G. Xie, B. Sundén, Effects of the pocket cavity on heat transfer and fluid flow of the downstream outlet guide vane at different flow attacking angles, Numerical Heat Transfer, Part A: Applications 74 (2018) 1087-1104.

**IV.** **J. Liu**, S. Hussain, J. Wang, L. Wang, G. Xie, B. Sundén, Heat transfer enhancement and turbulent flow in a high aspect ratio channel (4: 1) with ribs of various truncation types and arrangements, International Journal of Thermal Sciences 123 (2018) 99-116.

**V.** **J. Liu**, S. Hussain, L. Wang, G. Xie, B. Sundén, Experimental and numerical investigations of heat transfer and turbulent flow in a rectangular channel mounted with perforated ribs, submitted to International communications in Heat Mass Transfer, under review.

**VI.** **J. Liu**, W. Du, S. Hussain, L. Wang, B. Sundén, Improvement of film cooling effectiveness upstream of the leading edge of a turbine vane, prepared for journal publication.

**VII.** **J. Liu**, W. Du, S. Hussain, L. Wang, B. Sundén, Design of full-scale endwall film cooling of a turbine vane, prepared for journal publication.

**Publications not included in this thesis:**

**I.** **J. Liu**, S. Hussain, W. Wang, L. Wang, G. Xie, B. Sundén, Heat transfer enhancement and turbulent flow in a rectangular channel using perforated ribs with inclined holes, ASME Journal of Heat Transfer 141 (2019) paper No. 041702.

**II.** **J. Liu**, S. Hussain, J. Wang, L. Wang, G. Xie, B. Sundén, Application of fractal theory in the arrangement of truncated ribs in a rectangular cooling channel (4:1) of a turbine blade, Applied Thermal Engineering 139 (2018) 488-505.

**III.** **J. Liu**, G.N. Xie, B. Sunden, Flow pattern and heat transfer past two tandem arranged cylinders with oscillating inlet velocity, Applied Thermal Engineering 120 (2017) 614-625.

**IV.** **J. Liu**, S. Hussain, L. Wang, G. Xie, B. Sundén, Effects of a pocket cavity on heat transfer and flow characteristics of the endwall with a bluff body in a gas turbine engine, Applied Thermal Engineering 143 (2018) 935-946.

**V.** **J. Liu**, , G. Xie, B, Sundén, L. Wang, M. Andersson, Enhancement of heat transfer in a square channel by roughened surfaces in rib-elements and turbulent flow manipulation, International Journal of Numerical Methods for Heat & Fluid Flow 27 (2017) 1571-1595.

**VI.** S. Hussain, **J. Liu**, L. Wang, and B. Sundén, Suppression of endwall heat transfer in the junction region with a symmetric airfoil by a vortex generator pair. International Journal of Thermal Sciences 136 (2019) 135-147.

**VII.** S. Hussain, **J. Liu**, L. Wang, B. Sundén, Effects on endwall heat transfer by a winglet vortex generator pair mounted upstream of a cylinder, Journal of Enhanced Heat Transfer 23 (2016).

# Nomenclature

**Latin Characters**

| | |
|---|---|
| $A$ | area of the selected region ($m^2$) |
| $C$ | chord of the vane (m) |
| $C_p$ | pressure coefficient |
| $d$ | depth of the pocket cavity or diameter of cooling holes (m) |
| $D$ | distance between leading edge and upstream film cooling holes |
| $D_h$ | hydraulic diameter (m) |
| $e$ | height of the ribs (m) |
| $f$ | Fanning friction factor |
| $f_0$ | Fanning friction factor of a smooth channel |
| $F$ | film hole mass flow rate/mainstream mass flow rate |
| $H$ | channel height (m) |
| $h$ | heat transfer coefficient ($W/m^2 \cdot K$) |
| $I_{hole}$ | interval of adjacent two perforated holes (m) |
| $k$ | turbulent kinetic energy per unit mass ($m^2/s^2$) |
| $L_{\text{channel}}$ | total length of the channel (m) |
| $L_{\text{hole}}$ | length of the perforated holes of film cooling holes |
| $L_{\text{back}}$ | length of the downstream extended channel (m) |
| $L_{\text{d}}$ | distance between the pocket edge and the symmetrical vane (m) |
| $L_{\text{front}}$ | length of the upstream extended channel (m) |
| $Nu$ | Nusselt number |
| $Nu_0$ | Nusselt number of a smooth plate |
| $\overline{Nu}$ | averaged Nusselt number |
| $P$ | pitch distance of two rib rows, two vanes or two cooling holes |
| $Pr$ | Prandtl number |
| $p$ | pressure (Pa) |
| $p_{\text{ref}}$ | reference pressure (Pa) |
| $q_{\text{w}}$ | wall heat flux ($W/m^2$) |
| $q_{\text{loss}}$ | heat loss ($W/m^2$) |
| $R$ | fillet radius (cm) |
| $Re$ | Reynolds number |
| $S$ | slot mass flow rate/mainstream mass flow rate |

| | |
|---|---|
| $S_p$ | span of vane (m) |
| $T$ | temperature (K) |
| $T_c$ | coolant flow temperature (K) |
| $T_g$ | mainstream temperature (K) |
| $T_f$ | fluid temperature (K) |
| $T_w$ | wall temperature (K) |
| $u$ | flow velocity (m/s) |
| $x$ | streamwise direction (m) |
| $y$ | spanwise direction (m) |
| $z$ | normal direction (m) |
| W | channel width (m) |

**Greek symbols**

| | |
|---|---|
| $\alpha$ | attack angle of pocket or film cooling holes<br>streamwise inclination angle (degree) |
| $\beta$ | film cooling holes spanwise inclination angle (degree) |
| $\eta$ | film cooling effectiveness |
| $\theta$ | perforated ratio |
| $\Delta L$ | truncated length (m) |
| $\Delta p$ | pressure drop (Pa) |
| $\lambda$ | thermal conductivity (W/m·K) |
| $\mu$ | fluid dynamic viscosity (Pa·s) |
| $\rho$ | fluid density (kg/m$^3$) |

**Subscripts**

| | |
|---|---|
| 1 | the row close to the vane |
| 2 | the row relatively far to the vane |
| b | bottom surface |
| c | coolant |
| f | fluid |
| in | inlet |
| m | average/overall |
| max | maximum |
| out | outlet |
| s | smooth channel |
| vane | vane |
| w | wall |

# Contents

# 1 Introduction

Gas turbines are widely used in propulsion systems and some power plant applications. Heat transfer and fluid flow issues within gas turbines are still significant and engines search for the optimized structures to improve the efficiency.

This work consists of two parts, heat transfer and fluid flow related to the pocket cavity region and cooling of a turbine blade. The cooling of a turbine blade concerns internal cooling using ribbed channels and endwall film cooling design.

## 1.1 Background

### 1.1.1 Pocket cavity and outlet guide vane

Outlet guide vanes (OGVs) are placed in the gas turbine engine rear part and provide support to the main engine frame [1, 2]. They control the exhaust gas leaving the gas turbine and then affect the propulsion of the engine. In the design of advanced aero engines, flow manipulations of the OGV become more significant. A pocket cavity is generated at the junction position of the low pressure turbine (LPT) and the OGV when these are assembled together, as shown in Figure 1.1. This triangular pocket cavity is not designed for heat transfer purposes but is difficult to avoid in the mechanical assembly. Then a flow separation and recirculation region is formed over the pocket region. This kind of pocket cavities, due to the high Reynolds number and the specific shapes, are hardly investigated in previous research works. The heat transfer and flow pattern of pocket cavities have significant effects on the incoming flow of the OGVs. Accordingly, this work is concentrated on revealing heat transfer characteristics and flow details in the pocket cavity region.

The effects of the pocket cavity on heat transfer and flow characteristics of the endwall with a symmetric vane are investigated. In addition, the effects of the flow attack angle on the pocket cavity are considered because the flows driven by turbine blades are always oscillating and not so perpendicular. This will provide basic knowledge and good references for designers to place some support or aerodynamic structures in the rear part of a gas turbine engine.

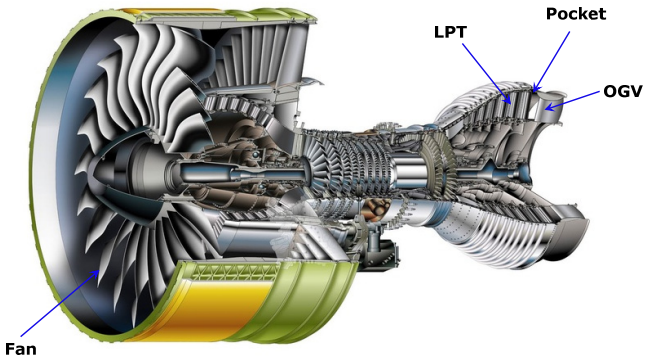


(a) A gas turbine engine (downloaded from Google).

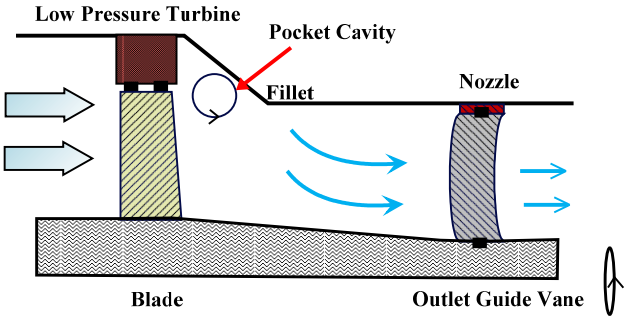


(b) A sketch of the pocket cavity.

Figure 1.1 A pocket cavity at the connecting part of outlet guide vane. (a) A gas turbine engine; (b) A sketch of the pocket cavity.

### 1.1.2 Internal cooling of a turbine blade

To improve thermal efficiency, gas turbine stages are being designed to operate at increasingly higher inlet temperature. To achieve higher thermal efficiency and power output in advanced gas turbines, the rotor inlet temperatures exceed the melting point of the blade material. In order to allow the gas turbine designer to increase the turbine inlet temperature while maintaining an acceptable blade temperature, sophisticated cooling methods are thus required. There are many heat transfer enhancement and cooling methods used for turbine blades to protect the blade material from exceeding the maximum allowable temperature [3], e.g., film cooling, impingement cooling, rib turbulated cooling and pin-fin cooling, as illustrated in Figure 1.2.

For the internal cooling of the blades, ribbed ducts are usually employed to increase the convective heat transfer. The presence of ribs, also called roughness elements or turbulators, enhances the heat transfer coefficients by creating redevelopment of the boundary layer after flow reattachment between the ribs and induced secondary flows [4, 5].

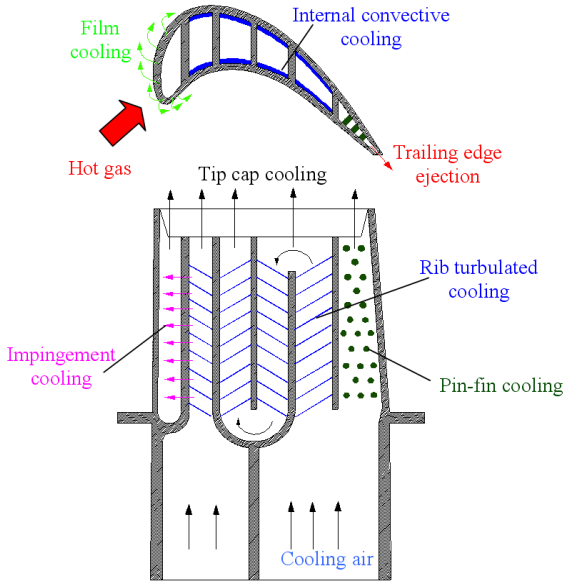


Figure 1.2 Internal cooling approaches of a turbine blade.

### 1.1.3 External cooling of a turbine blade

Film cooling, also called external cooling, is an effective method to protect a solid surface from a high temperature mainstream by injecting coolant flows [6, 7]. This kind of cooling method is widely used in the cooling of a turbine blade, such as endwalls, blade surfaces, blade body and tip regions [8]. Endwall film cooling is a significant cooling method to protect the endwall region and the junction region of endwall and a turbine vane, where usually a relatively high temperature load exists. Endwall film holes eject coolant air and form a protective film between the endwall and mainstream. Endwall film cooling works together with convective cooling methods but mainly used for high pressure turbine vanes which are located just downstream of the combustor chamber.

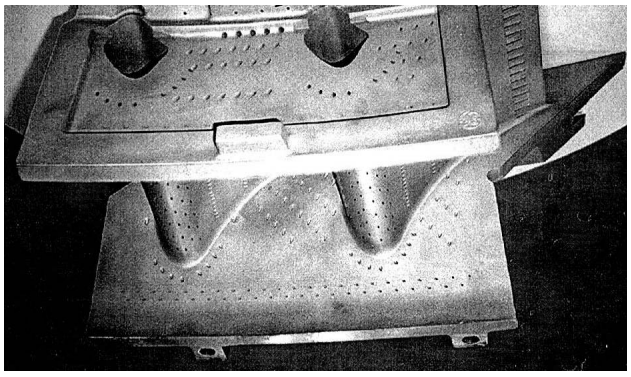

Figure 1.3 Endwall film cooling around nozzle guide vanes [9].

## 1.2 Contents and objectives

The research contents are about heat transfer in the pocket cavity and outlet guide vane regions, internal cooling using ribbed channels and endwall film cooling design. Both experimental and numerical works are included. Liquid Crystal Thermography (LCT) is employed to measure heat transfer over the surfaces. Numerical calculations are mainly performed by the commercial software, ANSYS Fluent 17.1.

The main contents are as follows:

**Pocket cavity and outlet guide vane:**

The specified triangular pocket cavities are built in a high aspect ratio channel and heat transfer and fluid flow over the pocket surface are investigated experimentally and numerically. These pocket cavities are built with different radii to find out improved heat transfer distributions and flow patterns (**Paper I**). Effect of the pocket cavity on the downstream endwall with a symmetrical vane is also considered in this work aiming to provide a reference for placing an outlet guide vane in the rear part of a gas turbine engine (**Paper II**). At last, effects of flow attack angle on the pocket cavity are considered. For the last part, only numerical calculations are included (**Paper III**).

**Internal cooling using ribbed channels:**

Firstly, truncated ribs are applied to improve thermal performances in a high aspect ratio channel (**Paper IV**). Eight different ribbed channels with various truncation types and arrangements of truncated ribs are designed. The optimized thermal performance of ribbed channels is attempted for by taking both heat transfer and pressure drop into consideration. The second part uses perforated ribs to improve thermal performance of ribbed channels (Paper V). Three different types of perforated ribbed channels are designed and compared. For the section of internal cooling using ribbed channels, both experimental and numerical works are included.

**Endwall film cooling:**

In this part, the work concentrates on the film cooling upstream of the leading edge and full scale endwall film cooling design. A number of film cooling holes are placed upstream of the leading edge and six various arrangements of the film cooling holes are designed and compared (**Paper VI**). The full scale endwall film cooling designs are, respectively, based on the pressure coefficient distribution, streamline distribution and heat transfer coefficient distribution on the endwall with a turbine vane (**Paper VII**). Four kinds of full-scale endwall film cooling arrangements are proposed and compared. This section is performed by numerical calculations.

## 1.3 Thesis outline

The background and overview of the thesis is presented in Chapter 1. Chapter 2 provides a literature review of related research works. Chapter 3 provides a detailed

description of the related measurement techniques and experimental setup, including experimental facilities, basic flow field measurements, validation of the test rig, tested models, data reduction and uncertainty analysis. The numerical investigation procedures are presented in Chapter 4. Each independent numerical analysis contain four parts, geometric model, mesh generation, governing equations and boundary conditions settings. Chapter 5 presents some results and discussions with detailed heat transfer and fluid flow characteristics. Chapter 6 presents main conclusions emerged from these works and highlights the future works.

# 2 Literature Survey

## 2.1 Pocket cavity and outlet guide vane

Outlet guide vanes (OGVs) are important components in the rear part of a gas turbine engine. They connect low pressure turbines to straighten the exhaust gas ejected from the engine. Though the temperature and pressure are not extremely high at OGV regions [2, 10], outlet ejected flows directly affect the thrust. In the rear part of an engine, it is designed as a contracted part to obtain high ejection velocity. A pocket cavity is formed at the connection part when the OGV and the LPT are assembled together.

### 2.1.1 Heat transfer over the pocket

Unlike gas turbines, pockets, grooves or similar structures are usually designed as heat transfer enhancement elements in heat exchangers and cooling devices. Researchers have done a lot of fundamental research works on the rectangular and triangular grooves [11-14]. Lorenz et al. [11] measured heat transfer coefficients along channel walls with rectangular grooves under fully-developed periodic turbulent flow and thermal developing boundary layer in the Reynolds number range of $10^4$ to $10^5$. They concluded that the Nusselt number augmentation ratio of the grooved surfaces was about $1.52 \leqslant Nu/Nu_0 \leqslant 1.75$ normalized by a smooth channel. A correlation between heat transfer and pressure drop was established by Adachi and Uehara [12] in channels mounted with expanded and contracted grooves. The channel with expanded grooves has better thermal performance than the one with contracted grooves. These contracted grooves were similar to conventional rib turbulators. Another hot topic about grooved structures is the combination with other heat transfer elements to augment heat transfer [14-17]. Jaurker et al. [14] aimed to improve heat transfer of a rectangular solar air heater duct using rib and groove combined structures. They found that the combined structures had enhanced heat transfer with reduced pressure loss penalty compared with rib-only channels. Similarly, Eiamsa-ard and Promvonge [15] measured the characteristics of heat transfer and turbulent flows in a rib-grooved channel. The rib-groove combined structures also presented significant heat transfer enhancement compared with a smooth duct. Gutierrez et al. [16] investigated heat transfer in a grooved channel with curved flow deflectors experimentally and numerically. The deflectors above the grooves could release the trapped fluid in the flow recirculation region inside the grooves and increase the fluid motion. The reduced flow recirculation inside the grooves increased the local heat transfer. Skullong et al. [17] combined wavy-groove and perforated-delta Wing Vortex Generators (WVG) in a solar air heater channel. The combination of wavy-groove and

perforated-delta WVG had 37.7-46.3% heat transfer enhancement compared to the groove only channel and 1.5-12.5% heat transfer enhancement compared to the combination of groove and non-perforated WVG. Researchers have paid more attention to novel shaped grooves to find the optimal configuration for best thermal performance in the past years [18-21]. In addition, as heat transfer enhancement structures, grooved structures have been tested together with nanofluids to find higher performance [22-25]. Several nanofluids are tested or simulated, e.g., copper-water, $Al_2O_3$-water, CuO-water, $SiO_2$-water and ZnO-water. Al-Shamani et al. [23] investigated heat transfer enhancement characteristics in a channel with trapezoidal rib-grooves using nanofluids. The study showed that these trapezoidal rib-grooves with nanofluids had the potential to dramatically increase heat transfer characteristics and thus might be very useful for high efficiency heat exchanger devices.

It should be noted that use of rounded corner of grooved structures to improve thermal performance, i.e., a fillet, has been proved useful in some previous literatures. Chen et al. [26] provided details of heat transfer enhancement over dimpled surfaces in turbulent channel flows. Their new-designed dimple geometry with a rounded corner at the imprinted boundary, presented better thermal performance than ordinary dimples. Liu et al. [27] designed novel grooved geometries, which were conventional cylindrical grooves with rounded transitions to the adjacent flat surfaces and with modifications at their bases. For the rounded transition grooves, the recirculating flow inside the groove was reduced and reattachment developed more smoothly.

### 2.1.2 Endwall heat transfer

Heat transfer and fluid flow on the endwall mounted with an obstacle, such as a bluff body or a vane or other combined structures, have received a lot of research interest. The three dimensional vortical structure produced by the obstacle greatly affects heat transfer on the endwall. Wang et al. [28] measured the endwall heat transfer characteristics with crossflow past bluff bodies using Liquid Crystal Thermography (LCT). The endwall heat transfer of a single bluff body and two bluff bodies arranged in tandem were both enhanced due to the horseshoe vortex. The power index of heat transfer correlated with Reynolds number was found and it was flow dependent. Praisner and Smith [29, 30] measured the endwall heat transfer and vortex structures formed upstream of an airfoil using simultaneous Particle Image Velocimetry (PIV) and LCT. Two high heat transfer zones were found upstream of the symmetric airfoil due to the vortex. Incidence angle was found to play a pivotal role in instabilities and vortex shedding for flow impingement on the vane leading edge. Kang et al. [31, 32] measured the heat transfer and flow fields on the endwall of the first-stage nozzle guide vane. They found that the generated secondary flows also caused large heat transfer enhancement near the trailing edge especially at the high Reynolds number. In addition, Reynolds number has some effects on the turbulence level and stagnation region in the leading edge of the vane.

Effects of the incoming flow condition on the endwall heat transfer and turbulent flow of turbine blades have received some interest [33-37]. Rhee and Cho [33, 34] investigated local heat/mass transfer characteristics on a stationary blade for various

relative positions of the blade in a stationary annular turbine cascade. They found that the change in blade position, which causes a much different interaction between vane and blade, altered the incoming flow condition. Qureshi et al. [35] investigated the effect of swirl flows on the aerodynamic and heat transfer characteristics of a high pressure turbine stage using a combustor swirl simulator. Zhang et al. [36] studied the effects of inlet turbulence and endwall boundary layer on aerothermal performance of a transonic turbine blade. They observed noticeable changes in heat transfer on the suction side near the tip surface due to the different inlet boundary layer profiles. Lynch and Thole [37] compared three-dimensional boundary layers formed on flat and contoured turbine endwalls. Elevated turbulence levels were found in the contoured endwall compared to the flat endwall.

### 2.1.3 Outlet Guide Vane heat transfer

An OGV provides the support and straightens the exhaust gas leaving the gas turbine. Because OGVs are not working under extreme high temperature and high pressure condition, the research works about OGVs do not receive so much attention. The incoming flows of OGVs are highly turbulent and unsteady and it is necessary to perform detailed heat transfer and fluid flow investigations for the OGVs. Hjarne et al. [38, 39] experimentally investigated the evolution of secondary flow characteristics in a low pressure turbine OGV. They found the intensity of the passage vortex and blade shed vorticity strongly dependent on the inlet flow angle and turbulence level. Chernoray et al. [40] focused on the aerodynamic performance of an OGV in a linear cascade. The surface non-conformances were designed as a generic welding race and a surface repair patch which were placed at different locations. They found the non-conformances had no great effects on the aerodynamic performance of the OGV even the roughness was large when the roughness are placed in special regions. Koch et al. [41] performed an optimization study of an OGV cascade experimentally and numerically. The research work presented the results of vorticity by five hole probe traverse, surface oil flow visualization and transition region measurement by pitot probe. In their study, the inlet flow angles were also considered and these were proved to have significant effects on transition regions.

The heat transfer and flow pattern of pocket cavities have significant effects on the incoming flow condition of the OGV. Research works about this kind of pocket cavity need to be deeply investigated to provide sufficient guidelines for the design of gas turbines. However, the heat transfer and fluid flow details are not fully-presented due to relatively high Reynolds numbers and the specific shape. Previous research works on pockets or grooves mainly focused on common grooves to enhance the overall heat transfer.

## 2.3 Internal cooling using ribbed channels

Ribbed passages are commonly used to increase the convective heat transfer for internal cooling of turbine blades by creating flow reattachment and boundary layer flow development and inducing secondary flows. Studies on ribs have paid attention

to many configuration parameters of ribbed channels, such as rib shapes, aspect ratio, pitch ratio ($P/e$), blockage ratio ($e/D_h$), rib angle of attack ($\alpha$), inclination of ribs, rotation of ribs and arrangement (staggered or parallel) [3-5]. However, previous research works have shown that ribs enhanced the heat transfer along with relatively large pressure drops. Recently, Chung et al. [42] used intersecting ribs in rectangular channels with different aspect ratios to enhance the thermal performance. Additional vortices were generated at the intersection region with the angled ribs and then heat/mass transfer performance was significantly enhanced. Alfarawi et al. [43] measured the heat transfer enhancement in a rectangular duct with hybrid ribs. They found that the hybrid ribs provided high thermal performance compared with those of the rectangular and semi-circular rib cases. New correlations for ($Nu/Nu_s$), ($f/f_s$) and $(Nu/Nu_s)/(f/f_s)^{1/3}$, were established as functions of Re and $P/e$ ratio based on all investigated geometries and configurations. Abraham et al. [44] measured heat transfer and pressure drops in a square cross-section converging channel with V and W shaped rib turbulators. They found that the local variations of the heat transfer coefficients in the spanwise direction were more significant for the V ribs than for the W ribs, which makes the W ribs a better choice as enhancement device considering the uniformity of the temperature field. Yang et al. [45] performed an experimental study on heat transfer characteristics of a high blockage ribbed channel. They found that the heat transfer coefficient of symmetrically arranged ribs is higher than for staggered ribs but with high pressure losses. Singh et al. [46, 47] combined rib turbulators and cylindrical dimples in a two-pass square duct mounted to enhance the heat transfer. It was observed that 45° angled ribs and V ribs compound configurations provided higher heat transfer augmentation as well as higher thermal hydraulic performance as compared with the corresponding ribs alone and dimples alone configurations.

It has been found that truncated ribs can effectively reduce the pressure drop with reducing heat transfer enhancement in some literatures [48]. Liou et al. [49] presented distributions of the full field Nusselt number and flow field by steady-state Infrared Thermography (IR) and PIV in two-pass channels with attached and detached transverse ribs. They created an empirical correlation evaluating the area-averaged Nusselt number and friction factors. Kumar et al. [50] investigated the heat transfer and pressure loss in an air passage with multi discrete V-blockages. The investigation confirmed the achievement of high thermohydraulic performance by truncated ribs. The best achievement was obtained by the case with a relative blockage height of 0.5, relative blockage pitch of 10, discrete blockage distance of 0.67, relative discrete width of 1.0, flow attack angle of 60° and relative blockage width of 5.0 compared to an air passage without blockages.

Perforated ribs or other perforated structures, also have received much attention in recent years [51-59]. Liou and Chen [51] measured the periodic turbulent heat transfer and friction in a rectangular passage with perforated ribs using laser holographic interferometry, smoke-steak flow visualization and pressure probing. The detached perforated-type ribs gave better heat transfer at a moderate rib height. Sara et al. [53] presented heat transfer enhancement and the corresponding pressure drop over a flat

surface in a channel flow with perforated rectangular blocks attached on its surface. Performance analysis indicated that the solid blocks could lead to energy losses up to 20% despite significantly enhanced heat transfer due to the increased surface area. However, the energy lost was recovered by perforations opened in the blocks. Buchlin [54] performed an experimental study of convective heat transfer in a channel using perforated ribs immersed in a turbulent boundary layer. Infrared thermography associated with the steady heated thin foil technique was applied to measure the heat transfer coefficient. Compared to solid rib, a local thermal enhancement factor of 3 could be obtained just behind the perforated turbulator. Chamoli [55] investigated the heat transfer and friction factor in a V down perforated baffle roughened rectangular channel. The results predicted by a response surface methodology showed good agreement with the experimental values in an uncertainty range of ±5%. Sahel et al. [56] performed a study of heat transfer enhancement in a rectangular channel with perforated baffles. The obtained results showed that the Pores Axis Ratio (PAR) of 0.190 was the best design that eliminated significantly the low heat transfer region, thus giving an increase in the heat transfer rate from 2% to 65% compared with the simple baffle. Hasanpour et al. [57] measured the heat transfer and pressure drop on typical, perforated, V-cut and U-cut twisted tapes in a helically corrugated heat exchanger. They found that the Nusselt number and friction factor for a corrugated tube equipped with modified twisted tapes were higher than for typical tapes.

In addition, many numerical works about ribbed channels have been performed using various turbulence models [60-66]. These turbulence models include Eddy Viscosity Model (EVM) and Explicit Algebraic Stress Model (EASM) by Saidi and Sunden [60] and Shear Stress Transport (SST) by Lin et al. [61]. Wongcharee et al. [62] studied ribs with different shapes with the $k$-$\omega$ SST model and the Renormalization Group (RNG) turbulence model. In their work, the results predicted by the SST $k$-$\omega$ turbulence model showed better agreement with the experimental data, than those predicted by the RNG $k$-$\varepsilon$ turbulence model. Kim et al. [63] studied the effects of inlet velocity profile on flow and heat transfer in the entrance region of a ribbed channel by the $k$-$\omega$ SST model. The numerical results showed that in the entrance region, the location and shape of the reattachment and the recirculation region were altered by different inlet velocity profiles. Gao et al. [64] performed a numerical study of conjugate heat transfer of mixed steam and air in a high aspect ratio rectangular ribbed cooling channel using the $k$-$\omega$ SST model. The generation and separation of secondary flows as well as the mixing of secondary flows could enhance the local heat transfer. Marocco and Franco [65] investigated convective heat transfer in a staggered ribbed channel with high blockage using Direct Numerical Simulation (DNS) and Reynolds Averaged Navier Stokes (RANS) methods. They found the $v^2f$ model performed much better than the $k$-$\varepsilon$ realizable model. Thermal performances of typical ribbed channels investigated in recent years are listed in Table 2.1.

Table 2.1 Thermal performances of typical heat transfer elements in recent years.

| Configurations | Reference | Re/1000 | $Nu/Nu_0$ | $Nu/Nu_0/(f/f_0)^{1/3}$ | Paramters |
|---|---|---|---|---|---|
| 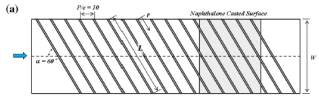 | [42] | 10, 20 | 2.6-3.25 | 1.35-1.95 | 60º inclined ribs, W/H = 1.0-4.0, P/e =10, 0.125 < e/H < 0.2 |
| 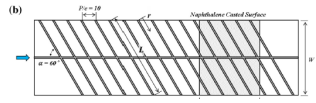 | [42] | 10, 20 | 2.8-3.6 | 1.47-2.07 | 60º inclined ribs, W/H = 1.0-4.0, P/e =10, 0.125 < e/H < 0.2 |
| 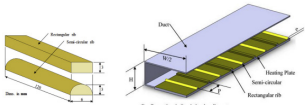 | [43] | 12.5-86.5 | 1.3-2.4 | 1.8-4.2 | Straight and cylindrical ribs, P/e = 6.6-53, e/H = 0.075 |
| 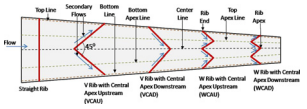 | [44] | 5-35 | 1.9-3.0 | 0.9-1.45 | V combined with W shaped ribs with 45º angle, P/e =6, 10, 17.5, e/H = 0.08 |
| 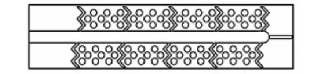 | [47] | 19.5-69 | 3.5-4.2 | 1.2-1.65 | 45º W shaped ribs, P/e = 16, e/H = 0.1 |
| 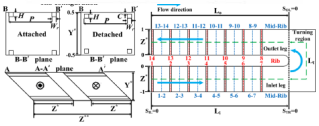 | [49] | 5-20 | | 1.5-2.1 | Detached ribs, P/e =10, e/H = 0.1 |
| 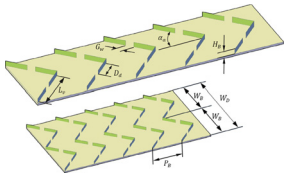 | [50] | 3-8 | | 1.78-3.24 | Flow attack angle: 30º–70º, P/H = 8-12 |
| 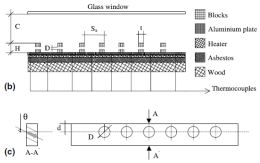 | [53] | 6.6-40 | 1.75-2.8 | | Perforated ribs, inclined angle = 0° to 45º, e/H = 0.454 |
| 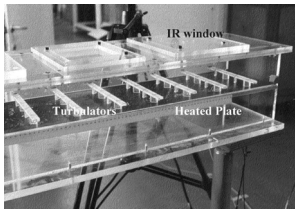 | [54] | 30-60 | 1.4-2.0 | | Perforated ribs with different shaped holes, |

| | | | | | |
|---|---|---|---|---|---|
| 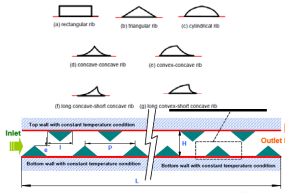 | [62] | 3-7 | 2.0-2.8 | 0.88-1.35 | Different shaped ribs, P/e =6.67, e/H = 0.22 |
| 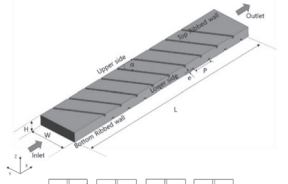 | [63] | 10, 20, 30 | 1.62-1.67 | 1.02-1.17 | 60º inclined ribs, P/e =10, e/Dh = 0.125 |
| 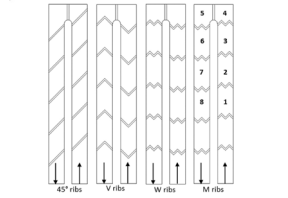 | [66] | 20-70 | M : 1.7-1.85<br>W : 1.75-7.95<br>45º : 2.18-2.28<br>V : 2.32-2.42 | M : 0.8-0.95<br>W : 0.84-1.02<br>45º : 1.02-1.15<br>V : 1.04-1.17 | 45º inclined V, W, M shaped ribs, P/e =16, e/$D_h$ = 0.125 |
| 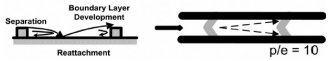 | [67] | 30-400 | 2.1-3.9 | 0.7-1.6 | 45º V shaped rib, 5 < P/e < 10, 0.1 < e/$D_h$ < 0.18 |

## 2.4 External cooling of a turbine blade

Film cooling is a cooling method to protect a solid surface from a high temperature mainstream by injecting coolant flows from discrete holes placed on its surface [6, 7]. Because coolant flows are easily available from the compressed air within a gas turbine, this cooling method is widely used in the cooling of a turbine blade, including endwalls, blade surfaces, blade body and tip regions [8]. Due to the complex surfaces of a turbine blade, inherent complex flow field, extreme working circumstance, film cooling is difficult to predict well when it is applied in a gas turbine [7]. The research works on film cooling have involved several main aspects, such as the pressure and temperature ratio of mainstream to coolant, the location, configuration and arrangements of film cooling holes on a specified blade surface [68, 69]. The effect of the mainstream turbulence intensity and the unsteady wake effect are also considered some research works [70]. Endwall film cooling of a turbine blade is relatively complex because of the complex flow fields caused by the horseshoe vortices [71, 72]. A horseshoe vortex has strong transporting and rotating effects which affect the coolant coverage on the target surface. Not only the mainstream horseshoe vortex, the generated secondary vortices, such as passage vortex and corner vortices, also strongly affect the flow field on the endwall. Ghosh and Goldstein [7] used a mass transfer method to measure the flow pattern on the endwall of a gas turbine blade in a linear cascade. They found the inlet skew has little effect on the Sherwood number distribution on the pressure side.

### 2.4.1 Film cooling on a flat plate

Single row or two rows of film cooling holes on a flat plate have been investigated to give fundamental heat transfer and fluid flow characteristic for film cooling. These can also serve as basic knowledge of film cooling on a turbine blade.

Sinha et al. [73] measured a single row of holes with various density ratio using thermocouples. They found a change in density ratio would change the momentum flux ratio which affected the spreading of the film cooling. Haas et al. [74] investigated the influence of density ratio on film cooling by both predictions and experiments. In their research work, the film cooling effectiveness increased with increased density ratio. Ligrani et al. [75] used a single row of compound angle film cooling holes on a flat template. They found compound angle injection of the coolant air will greatly improve the film cooling protection with increased coolant coverage. Goldstein and Jin [76] measured the cooling effectiveness downstream of one row of compound angle holes using the naphthalene sublimation method. Similarly, when the compound angle holes are used, the laterally-averaged effectiveness is enlarged compared with normal inclined holes at the same blowing ratio. The effect of the hole length-to-diameter ratio ($l/d$) [77] and pitch-to-diameter ratio [78] ($P/d$) are considered in some previous research works. In recent years, more research works [79, 80] are focused on shaped holes to increase the cooling effectiveness, such as fan-shaped holes, which have exhibited higher effectiveness compared with cylindrical holes at higher blowing ratios.

Jabbarl and Goldstein [81] measured the adiabatic wall temperature downstream of injection of two rows of cooling holes. Two rows of holes are considered more effective in protecting the solid wall than one row. Jubran and Brown [82] investigated the film cooing with two rows of holes inclined in both the streamwise direction and spanwise direction. Similarly, two rows also showed improved film cooling compared to one row. Sinha et al. [83] tested the flow field of two rows of holes related to gas turbine film cooling. The thickness of the boundary layer effect was considered in their work. They found the injection would penetrate strongly when the boundary layer upstream of the cooling holes is thick. Ligrani et al [84] studied two rows of compound film cooling holes with staggered arrangement to improve the cooling effectiveness. The results showed that compound angle cooling holes have better cooling protection than simple inclined holes. Similarly, two rows of compound angle holes arrangement are found in some other research works [85, 86]. They all agreed that the combination of two rows of compound angle holes with staggered arrangement can significantly improve the cooling effectiveness. More recently, Dittmar et al. [87] investigated the film cooling of compound angle holes based on shaped holes. When the blowing ratios are moderate or high, the fanshaped holes show good performance with increased coolant coverage in the spanwise direction. Natsui et al. [88] measured the film cooling effectiveness of multi film cooling arrays on a flat surface using Pressure Sensitive Paint (PSP), which is mass transfer measurement. They used film cooling holes with 20º injection angles made by stereolithography (SLA).

### 2.4.2 Turbine endwall film cooling

Full scale endwall film cooling related to gas turbines has been investigated by some researchers [89-95]. Granser and Schulenberg [89] firstly measured the film cooling effectiveness for a first-stage turbine vane shroud using thermocouples in a linear vane cascade. From their research work, the film cooling effectiveness near the suction side was higher than that near the pressure side. Burd and Simon [90] investigated the effects of upstream slot cooling over a contoured endwall with a nozzle guide vane (NGV). They found the upstream bleed cooling has no effects on the aerodynamic penalty and had benefits in reducing secondary flow effects. Oke et al. [91, 92] measured the film cooling effectiveness on a contoured endwall using bleed holes upstream of a NGV. The coolant injection rates were controlled in the experiments. They found that the momentum flux is an important parameter which affects the coolant coverage between the passages. Zhang and Jaiswal [93] investigated the endwall film cooling of a NGV using PSP. They found the averaged film cooling effectiveness had a nonlinear relation with the increased mass flow rate which indicated the interference between coolant injections with endwall secondary flows. Knost and Thole [94] measured full scale endwall film cooling effectiveness for a first stage vane using IR camera. Two film cooling hole patterns with an upstream slot are tested. They found two regions, i.e., the leading edge region and pressure side with endwall junction region, were difficult to cool. Shiau et al. [95] presented full scale endwall film cooling effectiveness distributions using the PSP methodology in a annular cascade. The results serve as good references for the design of endwall film cooling holes.

Endwall film cooling plays an important role in protecting the endwall and vane-endwall junction region. However, many research works have confirmed that two regions on the endwall are difficult for the coolant coverage due to the complex flow field, i.e., leading edge region and endwall-pressure side junction region. The leading edge part has strong flow impingement and high pressure where the coolant flow is difficult to eject out. Sundaram and Thole [96, 97] investigated the film cooling at the leading edge of a NGV using trenched holes or bump modifications aiming to improve leading edge film cooling. However, the research works improve film cooling effectiveness in the two tough regions are not sufficient. More research works are still needed to improve overall averaged film cooling effectiveness and local film cooling effectiveness in such regions.

# 3 Measurement Techniques and Experimental Setup

## 3.1 Liquid Crystal Thermography

### 3.1.1 Introduction to LCT

Liquid Crystal Thermography (LCT) is a non-intrusive measurement technique to determine convective heat transfer coefficients on solid surfaces. The great advantage of the LCT is that it is capable of providing a global temperature field with high resolution, even for complex structured surfaces.

The featured ability of LCT is based on materials called Thermochromic Liquid Crystals (TLC). TLC is a kind of material that changes the reflected color as a function of temperature when illuminated by white light. The light is reflected over a specific range of wavelengths. Because the reflected color is a function of temperature, TLC can be used as a temperature indicator on the target region. Liquid crystal is a unique organic material which exists between the solid and the isotropic liquid phase [98]. Between these temperature limits, it shows a certain molecular structure that resembles the crystalline state. Therefore, thermotropic phases are those that occur in a certain temperature range. If the temperature is too high, thermal motion will destroy the delicate cooperative ordering of the LC phase, pushing the material into a conventional isotropic liquid phase. At too low temperature, most LC materials form a conventional crystal.

To relate color with the corresponding temperature, several methods have been used in recent years. The hue-temperature method is most popular due to its high resolution for heat transfer measurements. The LC images are firstly captured by a camera in red, green, blue (RGB) components and then they can be converted to hue, saturation and intensity (HSI) components by the software, Matlab 2012. The hue value, with a range of 0 to 255, is corresponding to a specified temperature state of the LC.

### 3.1.2 Calibration of LCT

Before the experiments, the LCT sheet needs to be calibrated to obtain the relationship between the temperature and the hue values at different viewing angles. In the experiments, the LC sheet, R35C5W from Hallcrest, is used and two different viewing angles (45˚, 90˚) are chosen in the calibration experiments. The calibration rig is shown in Figure 3.1. The calibration experiments are performed in a black enclosure to prevent interference from ambient environment. The system is heated by forced hot air with a temperature controller. The LC sheet is attached on an aluminum plate to

obtain a relatively uniform temperature field. The LC temperature is recorded by several thermal couples.

The calibrated hue-temperature curve is shown in Figure 3.2. Only the green color range is used for determining the temperature due to its high resolution, i.e., ranging from 60 to 100. For different viewing angles, different correlations between hue and temperature are obtained. A slight difference can be found in the hue values when the view angle is changed. Therefore, the correlations are generally divided into two groups, 45˚ viewing angle and 90˚ viewing angle respectively implemented in the processing code. In the experiments, to measure the heat transfer over the pocket cavity, the correlation of the 45˚ viewing angle is used. For other cases, the viewing angle 90˚ is used.

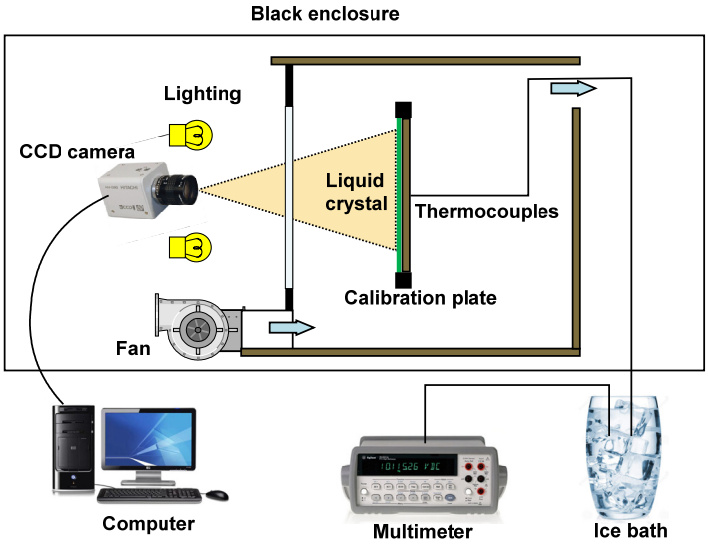


Figure 3.1 Experiment setup for LC calibration.

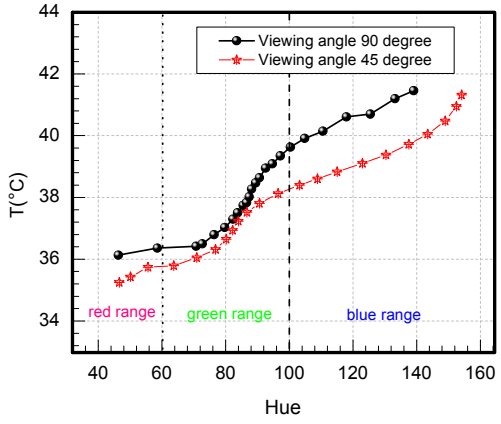


Figure 3.2 Hue-temperature curves in the calibration experiments.

## 3.2 Experimental setup

### 3.2.1 Overview

Heat transfer coefficients on the tested surfaces are measured by steady-state LCT. The schematics of the experimental setup and the LC package are shown in Figure 3.3. The mainstream is generated by a centrifugal fan in a rectangular channel with a total length of 500 cm, a width of 32 cm and a height of 8 cm. The channel inlet part is built as a bell shape to stabilize the incoming flow. The tested channel is made of Plexiglas with a low thermal conductivity ($\lambda$ = 0.2 W/m·K) to reduce the tangential heat conduction along the channel walls and the normal heat loss across the channel walls. The LC package placed in the rectangular channel is about 350 cm away from the inlet, to create a fully-developed flow regime for the tested region. The tested surface is covered by a heating foil to provide a uniform heat flux. The heat flux is adjusted by two transformers in series. An LC sheet R35C5W from Hallcrest is fixed on the top of the heating foil to capture the temperature. The back side of the test section is fixed with an insulation layer, made of Styrofoam ($\lambda$ = 0.03 W/m·K), to reduce the conductive heat loss. A CCD camera is placed above the test surface with two lights to provide sufficient luminance. The LC images are captured by the CCD camera with 1600×1200 pixel resolutions. The test system is surrounded by a dark enclosure to prevent interference from the ambient light.

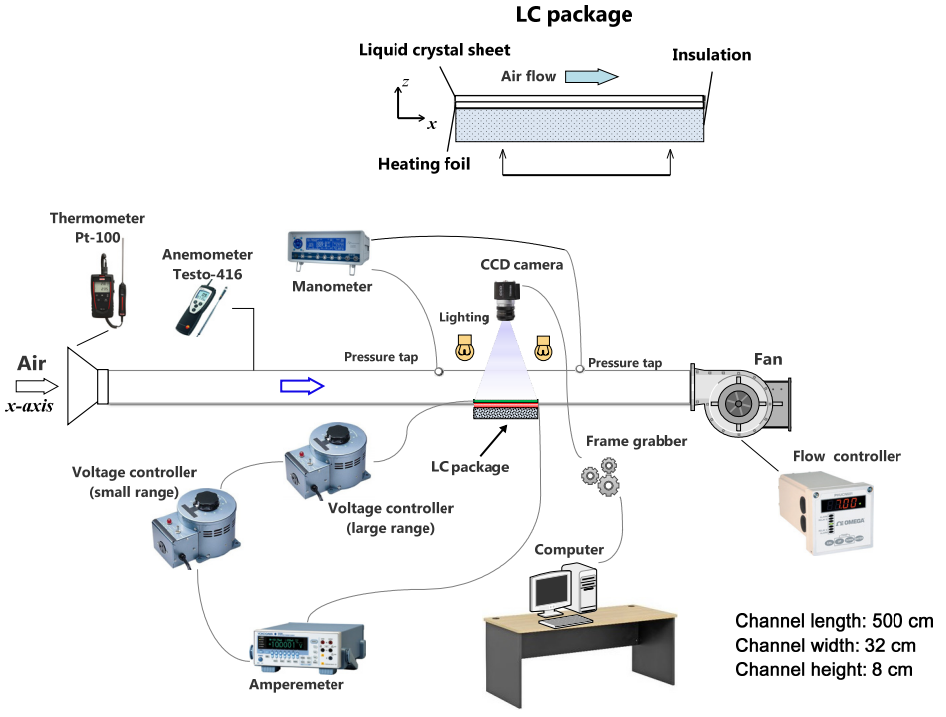


Figure 3.3 Experimental setup and LC package.

Two pressure taps are mounted at the two sides of the tested section with an interval distance of 130 cm. The main flow velocity can be adjusted by the frequency of the driven fan. The inlet air temperature is monitored by a thermometer, Pt-100. The channel center maximum velocity is measured by an Anemometer, Testo-416. According to the relation between the maximum velocity and bulk-mean velocity presented in Schlichting [99], the mean velocity of the section can be obtained and the corresponding Reynolds number is determined.

### 3.2.2 Validation of the test rig

Before performing specific LCT heat transfer measurement, the test rig should be validated. The test channel is validated by heat transfer measurement on a smooth channel by LCT. The heat transfer distribution originating from the heating region is shown below, in Figure 3.4. The Nusselt numbers are normalized by the Dittus-Boelter correlation [100], which is shown later in Eq. 3.5. With the heat transfer boundary developing along the streamwise direction, the normalized Nusselt number is approaching unity, which proves the reliability of the test rig.

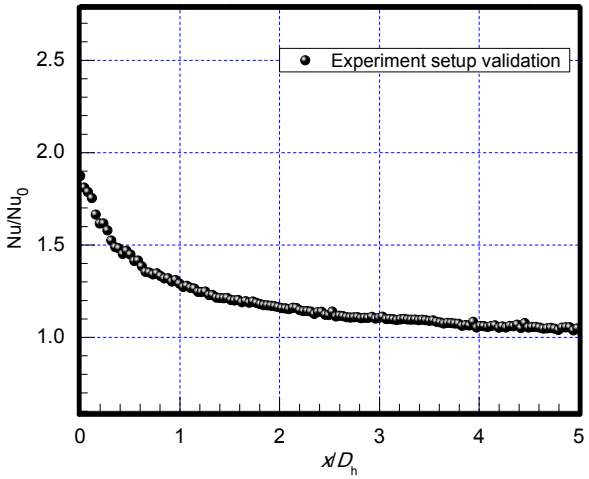


Figure 3.4 Experimental setup and LC package.

### 3.2.3 Basic channel flow parameters

- **Turbulence intensity**

Turbulence intensity of the tested channel is measured by 1-D Hot Wire Anemometer from Dantech Streamline. The flow measurements focus on the streamwise velocity component. The velocity fluctuations are measured at different mean mainstream velocity. The distribution of the velocity fluctuations versus time when the mean mainstream velocity is set to 10m/s is shown in Figure 3.5. For the averaged velocity ranging from 5 to 30 m/s, the turbulence intensity is ranging from 4% to 5% in the experiments, which can be used in the setting boundary condition for numerical calculations.

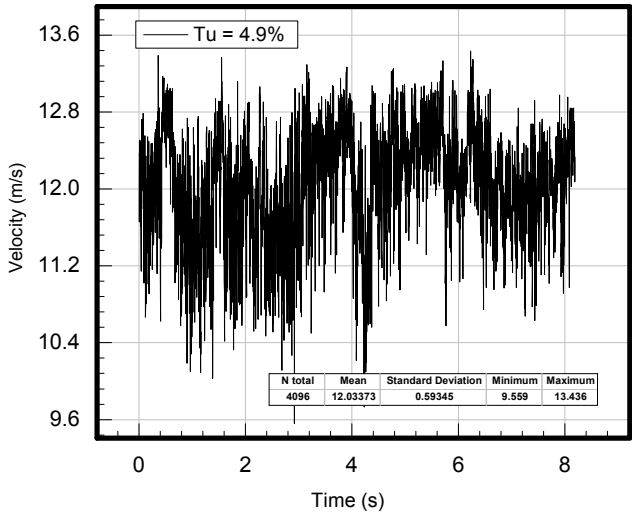


Figure 3.5 Velocity fluctuations measured by Hot Wire Anemometer.

➢ **Velocity profile**

The velocity profile is another important parameter for the tested channel. The velocity field of the channel in the streamwise-spanwise section is measured by a 2-D PIV system form Dantech (532nm). The velocity distribution along the normal direction ($z$) is shown in Figure 3.6. When the relative height is 0.3, the streamwise velocity reaches the highest value. The figure also confirms that the velocity distributions in coincidence with the relation in Schlichting [99].

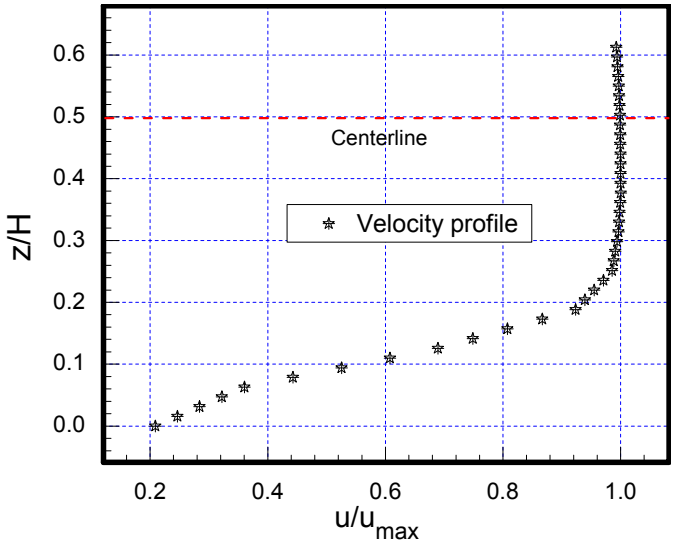


Figure 3.6 Mean velocity distribution measured by the 2-D PIV system.

## 3.3 Tested models

### 3.3.1 Pocket cavity with different fillet radii

In this work, the tested pocket is built as a simplified triangular groove with a fillet at the downstream edge in a high aspect ratio rectangular channel. Pocket models with different fillet radii are built to investigate the influence of the rounded corner and attempting for optimal structures.

The built triangular groove with a fillet at the downstream boundary is displayed in Figure 3.7. Based on the common contracted design in the OGV part, the inclination angle is built as 45˚ with a depth of the groove of 5 cm. The idea of rounded corner is an effective method to connect two components with different contacting angle, especially in the structures with high aerodynamic demands. The adoption of the rounded corner at shaped edges to improve heat transfer distribution has been found successful in Ref. [26, 27], which investigated on spherical dimples and cylindrical grooves, respectively. Two pocket cavity models with fillet radii 1 cm and 2 cm, respectively, are tested in the experiment. The heated area is the inclined surface of the pocket cavity and the adjacent downstream flat surface. In the experiments, the inlet flow velocity is controlled by the power of the fan and the considered Reynold numbers are, respectively, 87,600, 131,400, 175,200 and 219,000. The turbulence intensity in the experimental channel is about 5%, which is reasonable for the existing flow of the turbine blades.

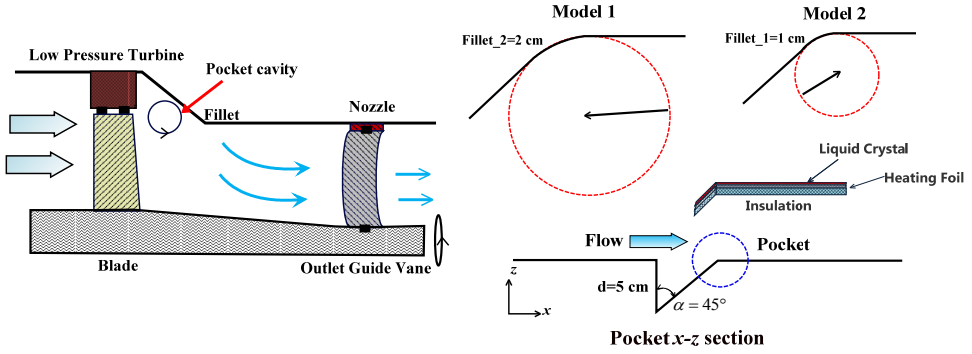


Figure 3.7 Triangular pocket cavity and fillet configurations.

### 3.3.2 Pocket cavity with a symmetric vane

In Figure 3.8, a symmetrical vane is placed on the endwall along the centerline in the tested duct with a pocket cavity placed upstream. The symmetrical vane is designed as a half circle connected with a triangle tail part. The width of the symmetrical vane is 4 cm and the height is the same as the channel height. The blockage ratio of the channel is 12.5%. The depth of the pocket cavity ($d$) is 5 cm. A fillet is used to connect the pocket cavity with the adjacent flat surface with a radius (R) of 2 cm. The distance between the symmetrical vane and the downstream edge of the pocket cavity ($d_L$) is

changed for different tested cases. It is defined as the distance ratio ($d_L$/d), ranging from 1 to 3 for different cases. In the processing of the images, the origin is set at the center of the symmetrical vane. Four cases are tested with the considered the Reynolds number ranging from 87,600 to 219,000.

**Case 0**: a symmetrical vane on the smooth channel;

**Case 1**: a symmetrical vane with a pocket cavity placed upstream ($d_L$/d = 1);

**Case 2**: a symmetrical vane with a pocket cavity placed upstream ($d_L$/d = 2);

**Case 3**: a symmetrical vane with a pocket cavity placed upstream ($d_L$/d = 3).

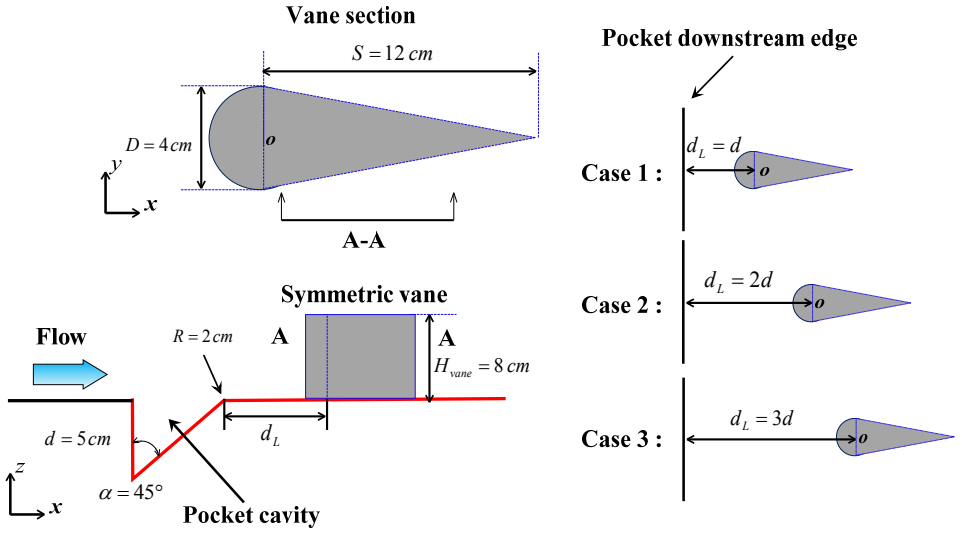


Figure 3.8 Schematic of the pocket cavity with a symmetrical vane and the tested cases.

### 3.3.3 Truncated ribs

This part focuses on heat transfer enhancement of internal cooling passages using differently-truncated ribs and arrangements. The tested channel is a high aspect ratio rectangular channel (4:1) with truncated ribs placed on the bottom walls. Eight kinds of ribbed channels are designed with different truncation types and arrangements, as shown in Figure 3.9. Five rows of ribs are placed on the bottom wall with a length of 50 cm and a width of 32 cm. Each rib row is truncated by 25% of the total length. The pitch ratio of the ribbed channel ($P/e$) is 10, the blockage ratio ($e/D_h$) is 0.078. Only the region between rib rows 3 and 5 is captured by the CCD camera to provide high resolution images. In the experiments, the Reynolds number ranges from 20,000 to 80,000.

**Case 1**: Traditional Continuous Ribs (TCR);

**Case 2**: Middle Truncated Ribs (MTR);

**Case 3**: Three Sides Equally Truncated Ribs (TSETR);

**Case 4**: One Side Truncated Ribs (OSTR);

**Case 5**: Two Sides Truncated Ribs (TSTR);

**Case 6**: Staggered Middle Truncated Ribs (SMTR);

**Case 7**: Staggered One Side Truncated Ribs (SOSTR);

**Case 8**: Two Sides with Middle Truncated ribs (TSMTR);

Cases 1 to 5 are regarded as parallel cases and cases 6 to 8 are regarded as staggered cases in the following analysis.

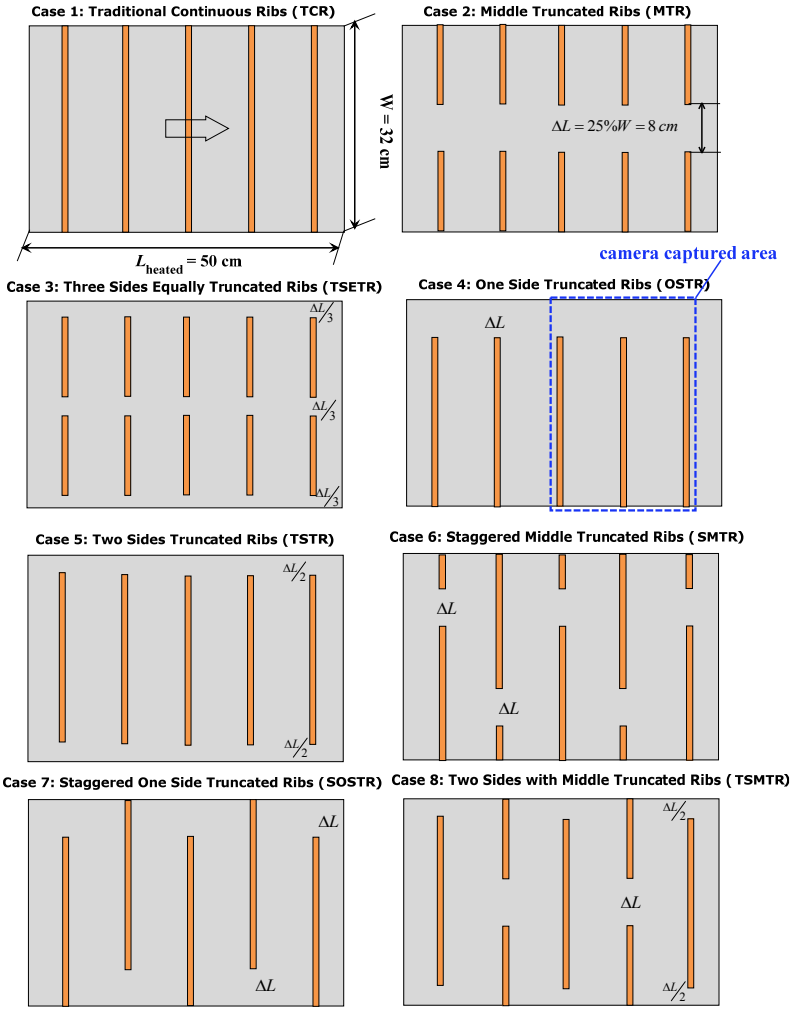


Figure 3.9 Eight ribbed walls with different truncation types and arrangements.

### 3.3.4 Perforated ribs

The test section and three kinds of designed perforated ribs are presented in Figure 3.10. Five rows of the ribs are arranged on the test section and the perforated ribs are placed in the central part of Row 3 and Row 4. The total length of the perforated rib is 8 cm with a square cross-section of 1 cm × 1 cm. The camera is focused on the perforated rib region between Row 3 and Row 4 aiming to give more clear details of the heat transfer fields. Three kinds of perforated ribs are designed. The perforated ratio $\theta$ is defined as the area of the hollow region/the area of the solid region.

**Case 1:** Continuous Ribs;

**Case 2:** Perforated Ribs (round hole with larger interval, $\theta = 0.176$);

**Case 3:** Perforated Ribs (square holes, $\theta = 0.225$);

**Case 4:** Perforated Ribs (round hole with smaller interval, $\theta = 0.282$);

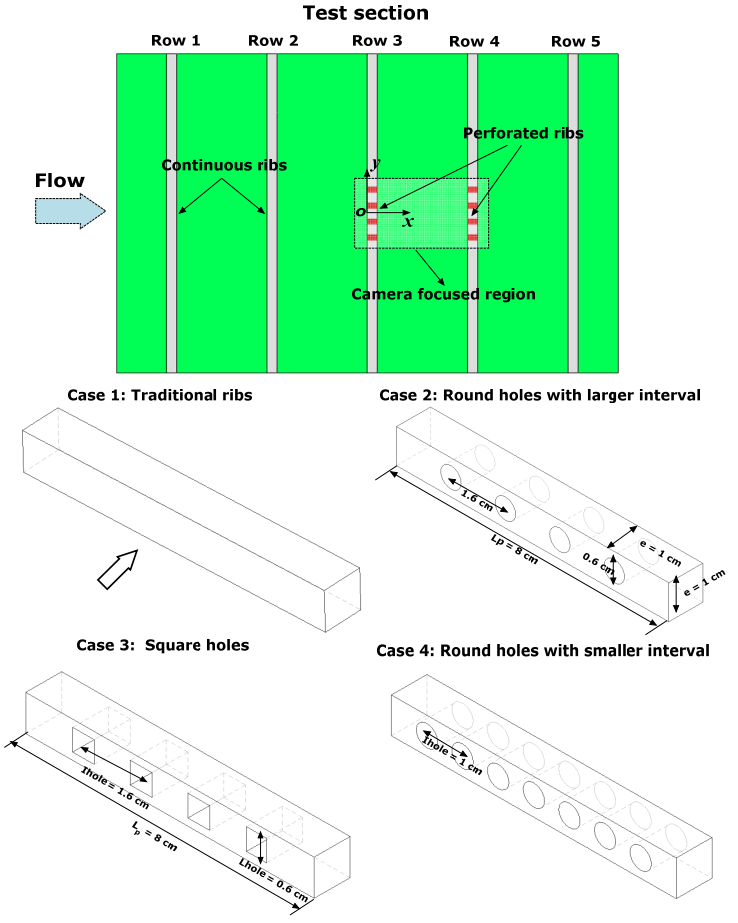


Figure 3.10 Test section and tested perforated rib configurations.

## 3.4 Data reduction and uncertainty analysis

The Reynolds number is defined as

$$Re = \frac{\rho u_m D_h}{\mu} \tag{3.1}$$

where $\rho$ is the density of the fluid, $u_m$ is the average velocity of the fluid in the channel, $D_h$ is the hydraulic diameter of the channel and $\mu$ is the dynamic viscosity.

By processing the captured images by the CCD camera, the heat transfer coefficient is obtained by

$$h = (q_w - q_{loss})/(T_w - T_f) \tag{3.2}$$

where $q_w$ is the supplied wall heat flux, $q_{loss}$ is the heat loss, $T_w$ and $T_f$ are, respectively, the wall temperature and the air temperature. As the air temperature difference, from inlet to outlet, is very small, $T_f$ is regarded as the inlet air temperature. Also, the thermal properties of air are based on the inlet air temperature.

The Nusselt number is obtained based on the hydraulic diameter of the channel,

$$Nu = hD_h/\lambda \tag{3.3}$$

where $\lambda$ is the thermal conductivity of air.

The Fanning friction factor $f$ is defined as

$$f = \frac{\Delta p}{2\rho u_m^{\ 2}} \cdot \frac{D_h}{L} \tag{3.4}$$

where $\Delta p$ is the pressure drop between the two pressure taps in the upstream and downstream of the ribbed channel, respectively and $L$ is the distance between the two pressure taps.

The Nusselt number and friction factors are normalized by the Dittus-Boelter correlation [54] and the Blasius equation, respectively, given by

$$\begin{cases} Nu_0 = 0.023\,Re^{0.8}\,Pr^{0.4} \\ f_0 = 0.079\,Re^{-0.25} \end{cases} \tag{3.5}$$

The thermal hydraulic performance of the channel is given as $(Nu/Nu_0)/(f/f_0)$ and $(Nu/Nu_0)/(f/f_0)^{(1/3)}$.

The uncertainty of the heat transfer coefficients is estimated using the method by Moffat [55]. The uncertainty of the heat transfer coefficient is found from

$$\frac{\Delta h}{h}=\frac{1}{h}\left[\left\{\frac{\partial h}{\partial q}\Delta q\right\}^2+\left\{\frac{\partial h}{\partial T_w}\Delta T_w\right\}^2+\left\{\frac{\partial h}{\partial T_f}\Delta T_f\right\}^2\right]^{0.5}$$
$$=\left[\left\{\frac{\Delta q}{q}\right\}^2+\left\{\frac{\Delta T_w}{T_w-T_f}\right\}^2+\left\{\frac{\Delta T_f}{T_w-T_f}\right\}^2\right]^{0.5} \tag{3.6}$$

The uncertainty of the Nusselt number is obtained from

$$\frac{\Delta Nu}{Nu}=\frac{1}{Nu}\left[\left\{\frac{\partial}{\partial h}(Nu)\Delta h\right\}^2+\left\{\frac{\partial}{\partial D_h}(Nu)\Delta D_h\right\}^2+\left\{\frac{\partial}{\partial k}(Nu)\Delta k\right\}^2\right]^{0.5}=\left\{\left(\frac{\Delta h}{h}\right)^2+\left(\frac{\Delta D_h}{D_h}\right)^2\right\}^{0.5} \tag{3.7}$$

The uncertainty of the friction factor is evaluated from

$$\frac{\Delta f}{f}=\frac{1}{f}\left[\left\{\frac{\partial f}{\partial(\Delta P)}\Delta(\Delta P)\right\}^2+\left\{\frac{\partial f}{\partial L}\Delta L\right\}^2+\left\{\frac{\partial f}{\partial D_h}\Delta D_h\right\}^2+\left\{\frac{\partial f}{\partial u_m}\Delta u_m\right\}^2\right]^{0.5}$$
$$=\frac{1}{f}\left[\left\{\frac{\Delta(\Delta P)}{\Delta P}\right\}^2+\left\{\frac{\Delta L}{L}\right\}^2+\left\{\frac{3\Delta D_h}{D_h}\right\}^2+\left\{\frac{2\Delta u_m}{u_m}\right\}^2\right]^{0.5} \tag{3.8}$$

The uncertainties in the velocity measurements are within 2%. The uncertainties in the pressure drop measurements are within 3%. The uncertainly of the friction factor is within 6%. The measurement errors of the wall temperature and the bulk temperature are estimated to be within ± 0.2 K and ± 0.1 K, respectively. The temperature difference between $T_w$ and $T_f$ is about 17 K. The non-uniformity of the heating foiling and the reading errors of the electric voltage and current are both less than 4%. The errors in calculation of the radiation and heat conduction losses are estimated to be less than 6% in total. Based on these estimations, the uncertainty of the heat transfer coefficient is within ± 6%. The uncertainties of the main measurement equipment are shown in Table 3.1.

Table 3.1 Uncertainty of various measurements.

| Measurements | Instruments | Uncertainty |
|---|---|---|
| Pressure loss | Manometer | ± 3% |
| Velocity | Anemometer | ± 2% |
| Wall temperature | Liquid crystal | ± 0.2 K |
| Air temperature | Thermometer | ± 0.1 K |

# 4 Numerical Investigations

Computational fluid dynamics (CFD) is a branch of fluid mechanics that uses numerical methods to solve and analyze problems of fluid flows. A normal CFD analysis usually contains four main steps, i.e., build of the geometric model, discretization of the volume (mesh), definition of governing equations and definition of boundary conditions.

## 4.1 Pocket cavity with different fillet radii

### 4.1.1 Geometric models and meshes

The computational domain is built exactly according to the tested channel with a shortened upstream and downstream extended channel. The computational domain is a rectangular channel with a length of 105 cm, a width of 32 cm and a height of 8 cm. The middle part of the bottom wall is the heated surface. In the numerical calculations, more cases with different fillet radii are considered of the effect of fillet radii. The fillet radii in the numerical calculations are, respectively, 0, 1, 2 and 5 cm. Fillet radius = 0 cm means the case with no fillets at the downstream edge of the pocket cavity.

The grids of the computational domain are generated by the software package ICEM 17.1. To generate the structured mesh in the pocket region, Y-blocks are used. The grid independence study can be found in the attached **Paper I**. The domain contains about 3.2 million meshes. The grids near the wall boundary are very dense to make $y^+$ values on the wall boundary around unity. Enhanced wall treatment is chosen as the wall functions. The computational channel and typical structured grids on the pocket surface and boundary layer characteristics are presented in Figure 4.1.

### 4.1.2 Selection of turbulence model

For the calculations, the $k$-$\varepsilon$ Re-Normalization Group (RNG model) is selected after comparing the calculated results of four different kinds of RANS turbulence models. The details of the turbulence model validations and governing equations of $k$-$\varepsilon$ RNG model can be found in **Paper I.**

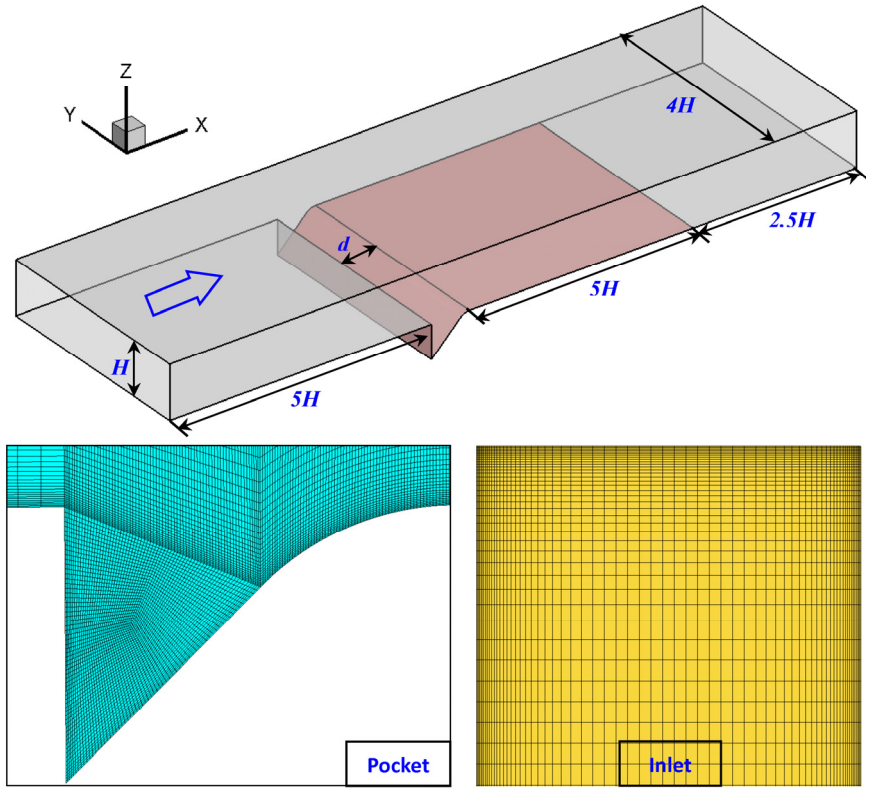


Figure 4.1 Schematics of the computational channel and typical structured grids used in the calculations.

### 4.1.3 Computational settings

The upstream and downstream extended channels are set as adiabatic. A constant surface heat flux of 1000 W/m$^2$ is applied on the heated section. No-slip velocity conditions are imposed at all the walls. Uniform velocity and temperature are utilized at the channel inlet. The inlet turbulence intensity level is set as 5%. The fluid is assumed as incompressible with constant physical properties.

The minimum convergence criterion for the continuity, momentum equations, $k$ and $\varepsilon$ equations is $10^{-5}$, while $10^{-7}$ is utilized for the energy equation. The commercial software ANSYS Fluent 17.1 is utilized to solve the governing equations with appropriate boundary conditions. The coupling of the pressure-velocity fields is handled by the SIMPLEC algorithm. A second order scheme is used for pressure discretization and a second order upwind scheme is used for the momentum and energy equations. In addition, the averaged wall temperature of the heated surfaces is monitored with an absolute criterion of $10^{-5}$ K.

## 4.2 Pocket cavity with a symmetrical vane

### 4.2.1 Geometric models and meshes

The computational channel is also built on the size of the test channel. The domain and meshes of typical regions are shown in Figure 4.2. However, the length of the experimental channel is very long, longer than 500 cm. In order to reduce the computational demands, the extended channels of the tested section are shortened. The upstream extended part is about $5D_h$, which is enough for providing fully-developed turbulent flow regime.

In order to obtain acceptable accuracy and computational efficiency, structured grids are employed. The grid independence study can be found in **Paper 2**. The computational domain contains about 4.5 million cells.

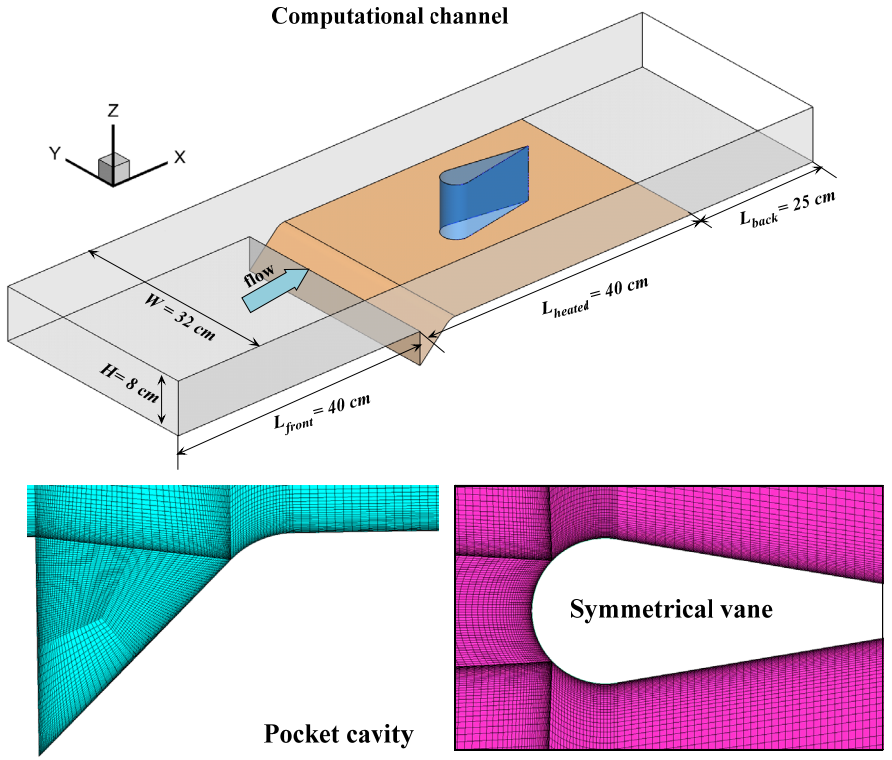


Figure 4.2 Computational channel and typical structured grids used in the calculations.

### 4.2.2 Selection of turbulence model

Recently, Large Eddy Simulation (LES) is considered as a relatively accurate method to solve turbulent flows, but requires a huge amount of computational efforts when

dealing flows with bounded walls. To ensure enough accuracy and reduce the computational demand, a method combining the LES model RANS model has been proposed, namely the Detached Eddy Simulation (DES) model [101]. DES models are specifically designed to address wall bounded flows at high Reynolds number to reduce the computational efforts of near-wall resolution of Large Eddy Simulation [102]. The Improved Delayed Detached Eddy Simulation (IDDES) model [103, 104] was furtherly a development of the original model to provide shielding against Grid Induced Separation (GIS), similar to the Delayed Detached Eddy Simulation (DDES) model [105]. The IDDES model modifies the treatment in the GIS for the LES, which may effectively resolve the turbulence activity approaching to the wall.

Unlike the flow conditions in the previous section, the flow circumstance around the symmetrical vane brings strong unsteadiness due to the vortex street. In order to describe the flow field, two kinds of turbulence models are applied, i.e., the steady $k$-$\omega$ SST model and the unsteady IDDES model. The validation of the models is provided in **Paper 2**.

### 4.2.3 Computational settings

The upstream and downstream extended channels are set as adiabatic. A constant heat flux of 1000 W/m$^2$ is applied on the considered endwall. No-slip velocity conditions are applied on the walls. Uniform velocity and temperature are set for the channel inlet condition. The inlet turbulence intensity level is set as 5%. The fluid is incompressible air with constant thermal physical properties due to the small temperature variations throughout the channel are very small. Therefore, the changes of thermal physical properties, such as absolute viscosity, thermal conductivity, specific heat, and density, are negligible.

The SIMPLEC scheme is used in dealing with pressure-velocity coupling adopted in the $k$-$\omega$ SST model. Second order upwind differences are employed in the spatial discretization of pressure, momentum, turbulent kinetic energy, specific dissipation rate and energy equations. Absolute convergence criteria are set as $10^{-5}$ for the continuity equations, velocity components, $k$ and $\omega$ and $10^{-9}$ is set for energy equations. The averaged temperature on the heated surfaces and mass flow rate on the outlet is also monitored to judge the convergence.

Different from the $k$-$\omega$ SST model, a coupled scheme is chosen for pressure-velocity coupling for the DES simulations. The benefit of the coupled scheme in calculation of unsteady flows is the low requirement on the time step. Second order upwind differences are chosen for spatial discretization. Bounded central differencing is used for the discretization of momentum equations. Second order implicit scheme is chosen for transient simulations. The time step size is set as $3\times10^{-4}$s and the absolute criterion is set as $10^{-4}$ during each time step. Two periods of channel-flowing-through-time are used to obtain a stable calculation and then three more periods are used for the statistics of the averaged calculation results.

## 4.3 Pocket cavity at different flow attack angles

### 4.3.1 Geometric models and meshes

This work is a numerical study and the geometry description is shown below. The computational channel is built based on the OGV profile with upstream extended and downstream extended channels as shown in Figure 4.3. The vane profile is taken from Wang et al. [2] with a chord length of 24.3 cm. The length of the upstream extended channel is 24 cm and the length of the downstream extended channel is 12 cm. The endwall and pocket region are the heated surfaces. The span of the OGV and the pitch are 24 cm. The pocket is placed upstream of the OGV with a distance of $L$ = 5 cm or 10 cm. The depth of the pocket $D$ is 5 cm with an attack angle of 45º connected to the adjacent flat surface. The fillet radius of the pocket cavity is 2 cm. The flow attack angles $\alpha$ change as -30º, 0º and +30º. The origin of the axis is set at the stagnation point of the OGV. Totally, nine cases are tested with different locations of the pocket cavity and flow attack angles (-30º, 0º and +30º), respectively, Case 0a, Case 0b, Case 0c, Case 1a, Case 1b, Case 1c, Case 2a, Case 2b and Case 2b.

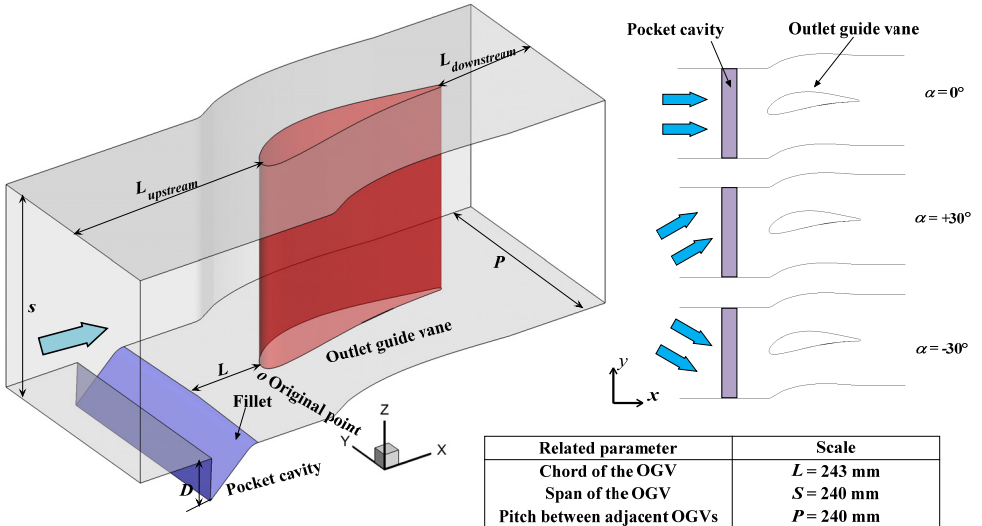


| Related parameter | Scale |
|---|---|
| Chord of the OGV | $L$ = 243 mm |
| Span of the OGV | $S$ = 240 mm |
| Pitch between adjacent OGVs | $P$ = 240 mm |
| Distance between the pocket cavity and the OGV | $L$ = 50 mm & 100 mm |
| Depth between the pocket cavity and the OGV | $D$ = 50 mm |
| $L/D$ | $L/D$ = 1 & 2 |
| Fillet radius | $R$ = 20 mm |
| Attack angle | $\alpha$ = 0°, +30° and -30° |

| | | |
|---|---|---|
| Case 0a ($\alpha$ = 0°) | Case 1a ($L/D$ = 1, $\alpha$ = 0°) | Case 2a ($L/D$ = 2, $\alpha$ = 0°) |
| Case 0b ($\alpha$ = +30°) | Case 1b ($L/D$ = 1, $\alpha$ = +30°) | Case 2b ($L/D$ = 2, $\alpha$ = +30°) |
| Case 0c ($\alpha$ = –30°) | Case 1c ($L/D$ = 1, $\alpha$ = –30°) | Case 2c ($L/D$ = 2, $\alpha$ = –30°) |

Figure 4.3 Computational domain and related parameters.

The grids of the computational channel are generated using the software package ICEM 17.1. Typical grids in the pocket region and the symmetric vane region are shown in Figure 4.4. In order to obtain acceptable levels of accuracy and computational efficiency, structured grids are employed. The figure shows that the grids near the boundary are very dense, whereas the grid density is relatively sparse far from the wall boundary. The mesh independence study can be found in **Paper III**.

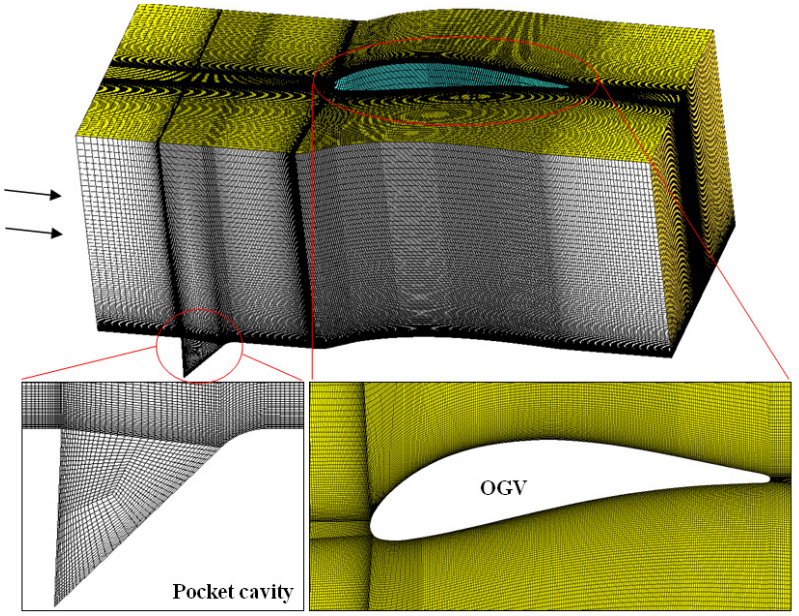


Figure 4.4 Computational channel and typical structured grids used in the calculations.

### 4.3.2 Selection of turbulence model

In the calculation part, two kinds of turbulence models are tested and compared, respectively *k-ω* SST model and DES model. The adoption of these two models is based on the experience from the study in **Section 4.2.** In addition, a comprehensive turbulence model validation study can be found in **Paper III**. The experimental results of the OGV endwall heat transfer for comparisons were performed by Wang et al. [2] in a linear cascade test facility.

### 4.3.3 Computational settings

In this study, the sidewalls and top wall are adiabatic. A constant surface heat flux of 1000 $W/m^2$ is applied on the endwall and the pocket region. No-slip velocity conditions are applied for all the walls, except the sidewalls. For the two sidewalls, transverse periodic wall condition is applied. Uniform velocity and temperature are applied at the channel inlet. The flow attack angle changes from -30º to +30º at a constant Reynolds number = 160,000. The turbulence intensity level at the inlet is set as 3.5 % consistent with the measurements by Wang et al. [2].

The setting of the solver in this study is similar to that in **Section 4.2.3**. The only difference is the setting of the DES model. A smaller time step, $1\times10^{-4}$s, is chosen in this study.

# 4.4 Truncated ribs

## 4.4.1 Geometric models and meshes

The computational domain is built up based on the tested channel but with relatively shorter inlet and outlet extended parts. The computational channel is a rectangular channel with a length of 150 cm, a width of 32 cm and a height of 8 cm. The upstream extended channel is 60 cm long and the downstream extended channel is 40 cm long. Only the middle bottom wall is heated. In order to obtain acceptable accuracy and computational efficiency, structured grids are employed. The grids near the wall boundary are very dense to make $y^+$ values on the wall boundary around 1.0 to meet the wall requirements of the *k-ω* SST model. The total number of control volumes for the whole channel is about 4.0M-4.6M, depending on the different truncated rib channels. The structured meshes near the ribbed surfaces are shown in Figure 4.5. The grid independence study is provided in **Paper IV**.

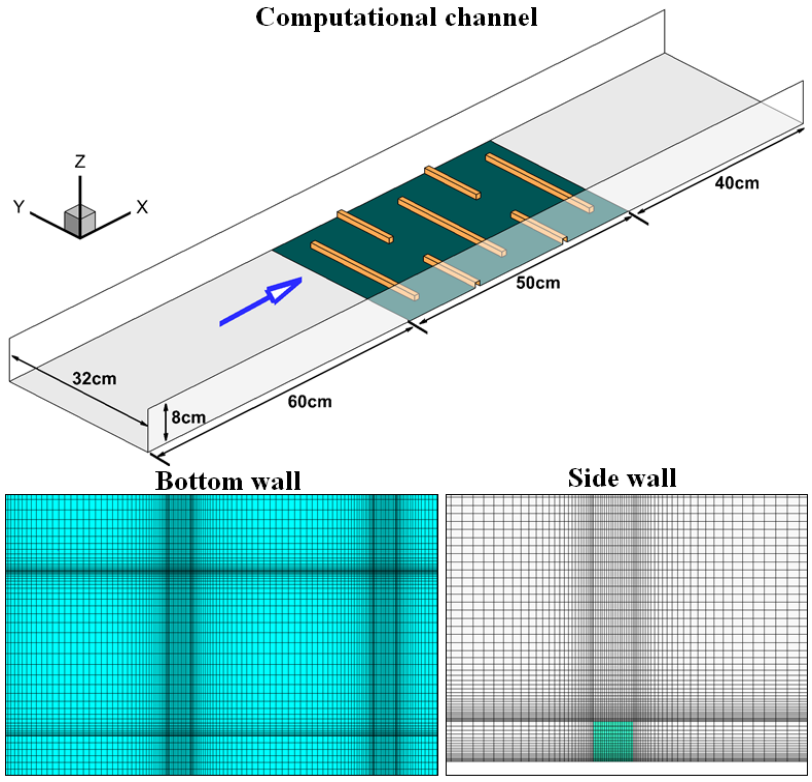


Figure 4.5 Computational channel and typical structured meshes in the domain.

### 4.4.2 Selection of turbulence model

The $k$-$\omega$ SST model is used in the calculations of the cooling structures in a turbine blade. The $k$-$\omega$ model has shown high accuracy and robustness in the boundary layer region and the $k$-$\varepsilon$ model is widely used for the shear and outer regions, irrespective of the freestream condition. Therefore, the combination of both models, the $k$-$\omega$ SST model, can give a high accuracy and robustness in solving turbulent flows. The selection of $k$-$\omega$ SST model is decided by a detailed turbulence model validation study which can be found in **Paper IV**.

### 4.4.3 Computational settings

Similar to other studies performed in the tested rectangular channel, the inlet-extended part and outlet-extended channel are adiabatic. A constant surface heat flux of 1000 $W/m^2$ is applied on the middle endwall. No-slip velocity boundary is applied for all the walls. Uniform velocity and temperature are set at the channel inlet. The inlet turbulence intensity level is set as 5%. The fluid is incompressible with constant thermal-physical properties because the temperature variations are very small.

ANSYS FLUENT 17.1 is employed to solve the governing equations. The SIMPLEC algorithm is chosen for the pressure-velocity coupling. Second order difference formulae are chosen for spatial discretization of turbulent kinetic energy, turbulent dissipation rate and energy equations.

## 4.5 Perforated ribs

### 4.5.1 Geometric models and meshes

The computational domain is built up based on the tested channel with the shortened inlet and outlet extended parts. The upstream extended channel is 60 cm (about $5D_h$) long and the downstream extended channel is 40 cm long. The length, width and height of the computational domain are, respectively, 150 cm, 32 cm and 8 cm. The bottom wall of the middle channel is the heated surface. The structured grids are generated by the software package ANSYS ICEM 17.1. The grids near the wall boundary are very dense to make $y^+$ values on the wall boundary around 1.0 to meet the wall requirements of the $k$-$\omega$ SST model and the DES model.

The total number of control volumes for the whole channel is around 7.0M and it changes a little for different kinds of perforated ribs. Typical structured meshes near the ribbed surfaces are shown in Figure 4.6. A detailed mesh independence study is provided in **Paper V**.

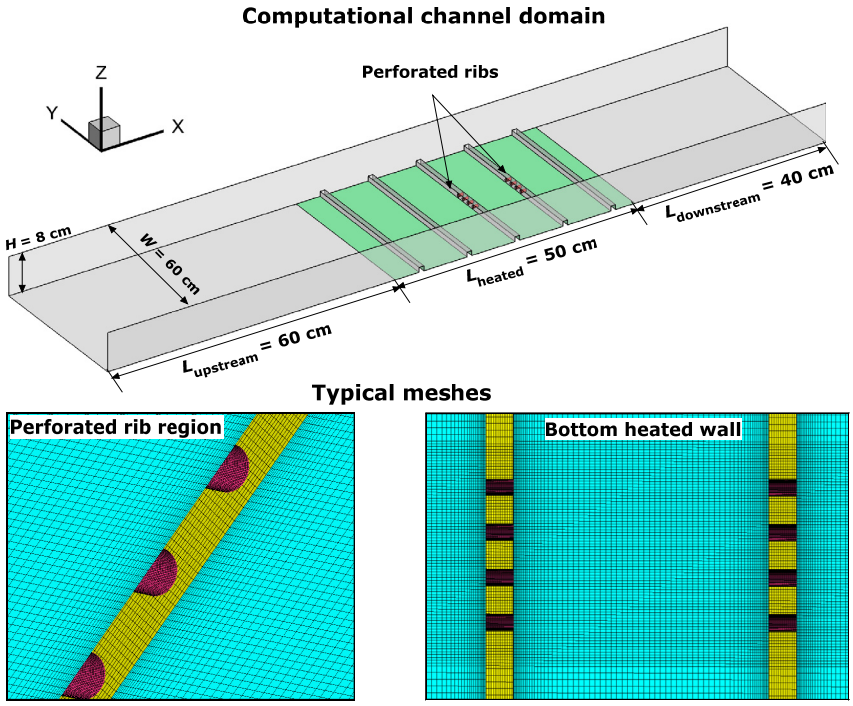


Figure 4.6 Computational channel and typical structured meshes in the domain.

## 4.5.2 Selection of turbulence model

Unlike **Section 4.4,** a more advanced turbulence model, DES model, is added in solving the complex flow field existing the perforated ribbed channel. Two kinds of turbulence models, i.e., *k*-*ω* SST and DES model, are tested and compared. The *k*-*ω* SST model, as an steady RANS model, is a hybrid turbulence model which takes advantages of both the *k*-*ε* model and the *k*-*ω* model [106, 107]. The solution of the *k*-*ω* SST model shows high accuracy and robustness in the boundary layer region. A DES model is considered suitable for dealing with the wall bounded flows, such as channel flows. The comparison of the experimental results and numerical calculated results is provided before the numerical calculation part, which can be considered as the validation of the turbulence model. Details can be found in **Paper V**.

## 4.5.3 Computational settings

The boundary setting and the solver setting for the *k*-*ω* SST model are the same as those in **Section 4.4.3**. For the DES model, the coupled method is chosen for the pressure-velocity field coupling. Second order difference formulae are chosen for spatial discretization of turbulent kinetic energy, turbulent dissipation rate and energy equations. Second order implicit method is chosen for the transient formulation. A bounded central differencing scheme is chosen for momentum discretization. The convergence criterion is set as $10^{-4}$ in every time step. The time step is set as 0.0003 s.

The period of six channel flowing-through time is chosen to obtain the time-averaged heat transfer and flow field.

## 4.6 Film cooling upstream of the leading edge

### 4.6.1 Geometric models and meshes

This part is about arranging film cooling holes upstream of the leading edge of a turbine vane and only numerical calculations are performed. The computational domain is displayed in Figure 4.7. The profile of the turbine vane is taken from the previous research works by Thole et al. [31, 108], scaled up by 9 times of the real vane. In the table of the figure, the basic parameter of the domain is provided. The domain is built based on the mid-line of the vane with upstream and downstream extended channels. The supply of the coolant at the leading edge for film cooling holes is from a rectangular plenum. The plenum is large enough to provide relatively uniform flows ejecting from each cooling hole.

Six different arrangements of the film cooling holes are designed. Case 1 is one row of nine cylindrical holes with a distance of 4*d* from the stagnation point. The interval between two holes (*P*/*d*) is 3. Case 2 has the same arrangement as Case 1 but is placed a little far away from the stagnation point (*D* = 8*d*). Case 3 has two rows of normal film cooling holes with staggered arrangement with an interval of 6*d*. For Cases 4-6, compound angle holes are applied aiming to combine the benefit of staggered arrangement and compound angle holes. Because of the specified region, upstream of the leading edge region, orientations of the placed compound angle holes may have some effects. Case 4 has two staggered rows of film cooling holes with compound angle holes. The spanwise inclination angle of the row close to the vane ($\beta$) is 45º and that for the other row is -45º. Case 5 also uses two rows of staggered arrangement but have opposite spanwise inclination angle relative to Case 4. Case 6 has the same arrangement as Case 4 with a relatively smaller interval between two rows. The total number of film cooling holes is unchanged for all the cases. The ejecting angle in the streamwise direction is 30º for all the cases. The designed cases are shown below.

**Case 1**: one row, cylindrical holes, D = 4d;

**Case 2**: one row, cylindrical holes, D = 8d;

**Case 3**: two rows, cylindrical holes, $D_1$= 6d, $D_2$ = 8d;

**Case 4**: two rows, compound angle holes, $D_1$= 4d, $D_2$ = 8d, $\beta_1$ = +45º, $\beta_2$ = -45º;

**Case 5**: two rows, compound angle holes, $D_1$= 4d, $D_2$ = 8d, $\beta_1$ = -45º, $\beta_2$ = +45º;

**Case 6**: two rows, compound angle holes, $D_1$= 6d, $D_2$ = 8d, $\beta_1$ = +45º, $\beta_2$ = -45º;

To improve the calculation accuracy, structured meshes are generated by ANSYS ICEM 17.1. The typical meshes used in the study are shown Figure 4.8. A detailed mesh independence study can be found in **Paper VI.** The total mesh for the computation domain is about 9 million.

| Related parameter | Scale |
|---|---|
| Chord of the vane | $C$ = 594 mm |
| Span of the vane | $S$ = 552.42 mm |
| Pitch between adjacent vanes | $Pvane$ = 457.38 mm |
| Inlet Reynolds number | 2.2×10^5 |
| Inlet mainstream velocity | 6.3 m/s |
| Angle between injection and mainstream direction | $\alpha$ = 30° |
| Spanwise inclined angle | $\beta$ = ±45° |

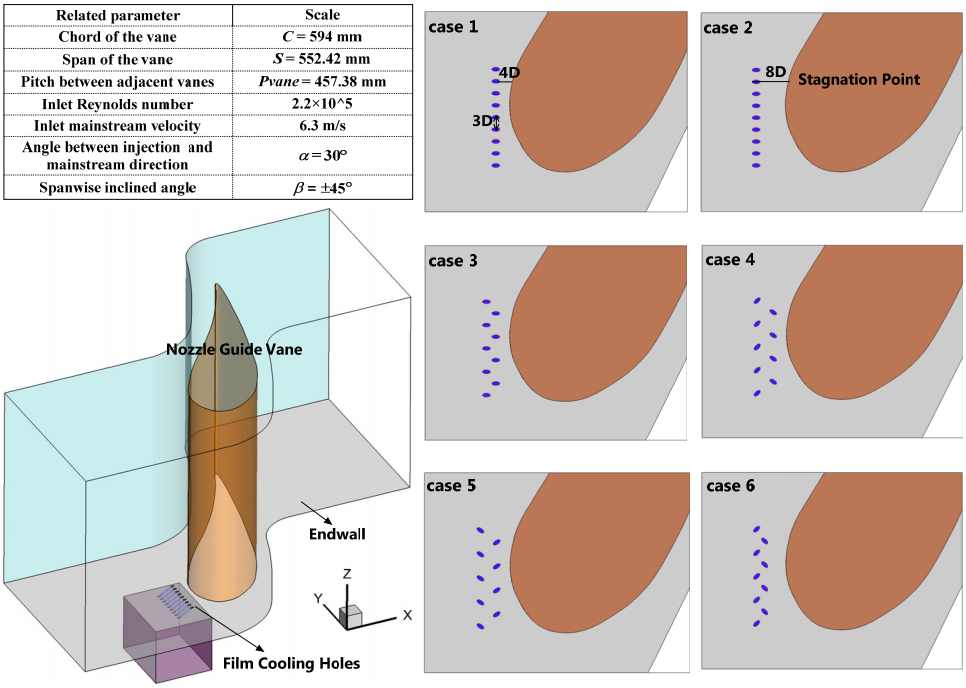


Figure 4.7 Computational domain and various arrangements of film cooling holes.

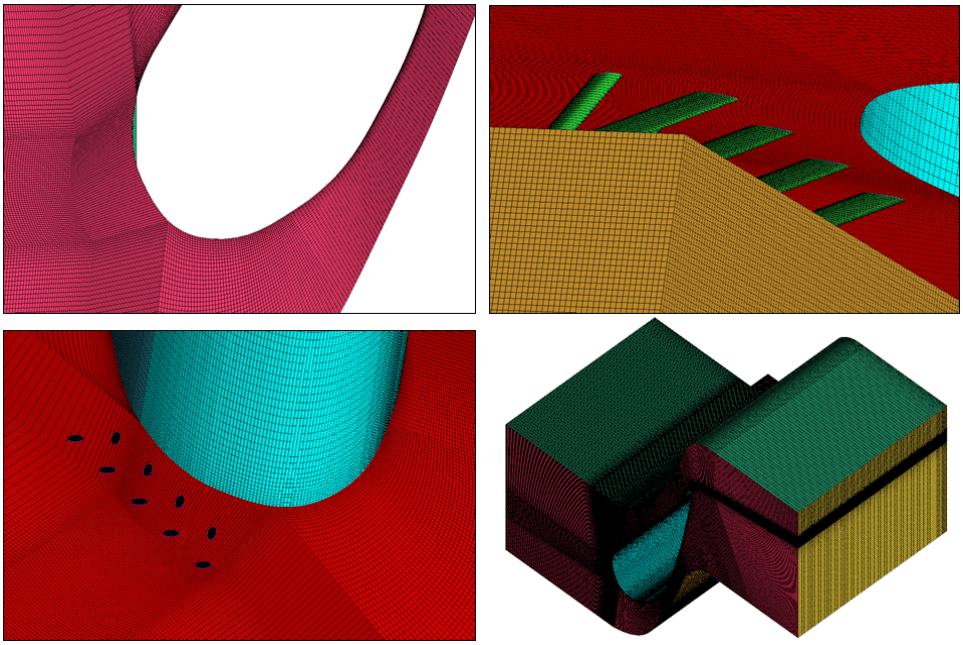

Figure 4.8 Typical structured meshes in the leading edge region.

### 4.6.2 Selection of turbulence model

In this study, the *k-ω* SST model is applied in the calculations to. This turbulence model has advantages in dealing with boundary layer region with high accuracy compared with other RANS models. A comprehensive turbulence model validation is provided in Figure 4.9 and Figure 4.10. Four different turbulent models, respectively *k-ω* SST model, *k-ε* model, transition SST model and *k-ε* realizable model, are used and compared. The experimental data is obtained from [32] by Kang at al. From the Figure 4.9(a), all the turbulence models have pretty good predictions of pressure coefficients compared with the experimental data. It has relatively large prediction errors in the transition part of the suction side. The predicted results are acceptable for all the considered turbulence models. The comparison of averaged Stanton number is shown in Figure 4.9(b). The averaged Stanton number is increased in the streamwise direction. The relatively large error is found at the transition region. Even the largest error between different turbulence models is still within 20% compared with the experimental data. For other regions, the predicted heat transfer data is quite close to the experimental data. The *k-ω* SST model provides good predictions for the pressure coefficients and Stanton number.

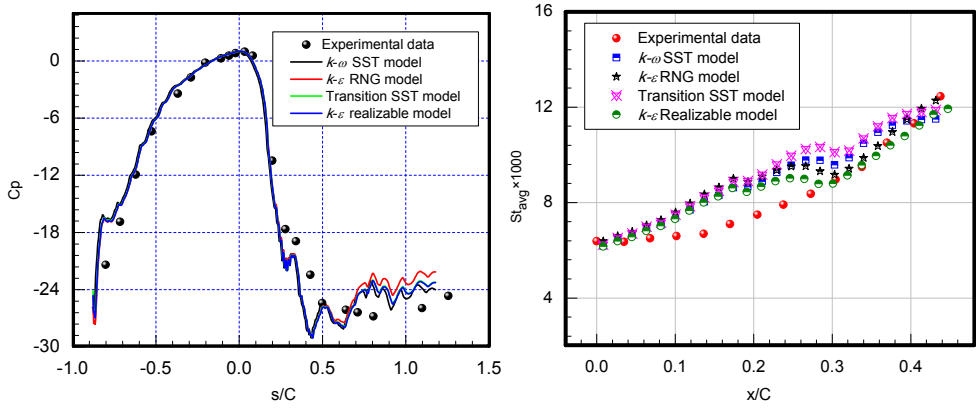


(a) Pressure coefficient comparison (b) Stanton number comparison

Figure 4.9 Turbulence model validations: comparisons of pressure coefficients and averaged Stanton number along the streamwise direction.

Figure 4.10 presents comparison of the endwall film cooling effectiveness predicted by the different turbulence models with the experimental data. The film cooling effectiveness is defined as

$$\eta = \frac{T_w - T_g}{T_c - T_g} \tag{4.1}$$

The pressure side has worse coolant coverage by the film cooling holes at the leading edge. For different turbulence models, the predicted film cooling effectiveness distributions have similar distributions. For the *k-ε* Realizable model, the errors of the film cooling effectiveness upstream of the vane are large. The film cooling holes at the stagnation region have difficulties to release the coolant flow. The cooling holes close to the suction side are easy to eject coolant flows. Considering all the comparisons,

including the pressure coefficients and heat transfer comparisons above and cooling effectiveness contours, the *k*-*ω* SST model is selected.

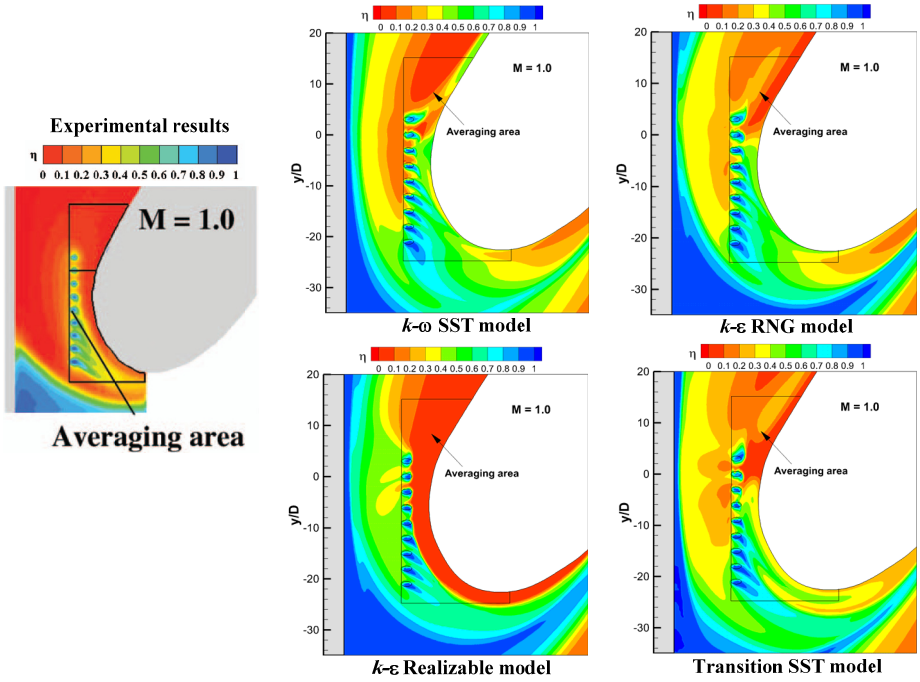


Figure 4.10 Turbulence model validations: comparisons of endwall film cooling effectiveness.

### 4.6.3 Computational settings

The boundary condition is set based on the experiments from [31, 108], which is also convenient for later comparisons. The temperature difference of the mainstream and the coolant is set as 20K and then physical properties of the air are assumed to be constant. The mainstream inlet is specified with a velocity of 6.3 m/s and the corresponding Reynolds number is $2.2 \times 10^5$. The inlet flow is assumed to be incompressible. The mainstream inlet temperature is 320 K. The two side-walls are periodic walls and built based on the middle line of the vane profile. The inlet of the rectangular plenum is set as a mass-flow-inlet with the cooling temperature at 300 K. The effects of the blowing ratio and mainstream turbulence intensity are considered. The two sidewalls are set as periodic walls. Other walls are set as adiabatic walls with no-slipped velocity. The outlet is set as pressure-outlet.

The SIMPLEC method is applied for the coupling of pressure and velocity field. Second order scheme is used for the discretization of pressure, momentum, TKE, and specific dissipation rate and energy equations. The absolute convergence criterion of $10^{-5}$ is set for the continuity equation and other velocity equations and $10^{-9}$ is chosen for the energy equation. In addition, the averaged temperature of the endwall is monitored to judge the convergence of the calculations.

## 4.7 Full scale endwall film cooling design

### 4.7.1 Geometric models and meshes

This part is a numerical work about full scale endwall film cooling design. The turbine vane [32] is the same as in **Section 4.6**. In contrast to **Section 4.6**, the domain in this part is focused on the flow passages between two vanes. The computational domain is shown in Figure 4.11. The coolant for endwall cooling holes is supplied by a plenum fitting the locations of the film cooling holes. Upstream of the endwall film cooling holes, a rectangular slot is fixed with an injection angle of 30º. The mainstream condition is the same as in **Section 4.6.** For controlling the endwall film cooling, two parameters, $S$ and $F$ are defined. $S$ means the ratio of slot mass flow rate to mainstream mass flow rate and $F$ means the ratio of film holes mass flow rate to mainstream mass flow rate. In this study, $S$ is fixed at 0.5% while $F$ is changing between 0.5% and 0.75% to investigate effects of the blowing ratio.

**Basic parameters**

| Related parameter | Scale |
|---|---|
| Chord of the vane | $C$ = 594 mm |
| Span of the vane | $S$ = 552.42 mm |
| Pitch between adjacent vanes | $P$ = 457.38 mm |
| Inlet Reynolds number | 2.2×10^5 |
| Inlet mainstream velocity | 6.3 m/s |
| Angle between injection and mainstream direction | $\alpha = 30°$ |
| Spanwise inclined angle | $\beta = (0° - 90°)$ |
| $S$ | 0.5% |
| $F$ | 0.5%, 0.75% |

$$S = \frac{Slot\ mass\ flow\ rate}{Mainstream\ mass\ flow\ rate} \times 100\%$$

$$F = \frac{Film\ hole\ mass\ flow\ rate}{Mainstream\ mass\ flow\ rate} \times 100\%$$

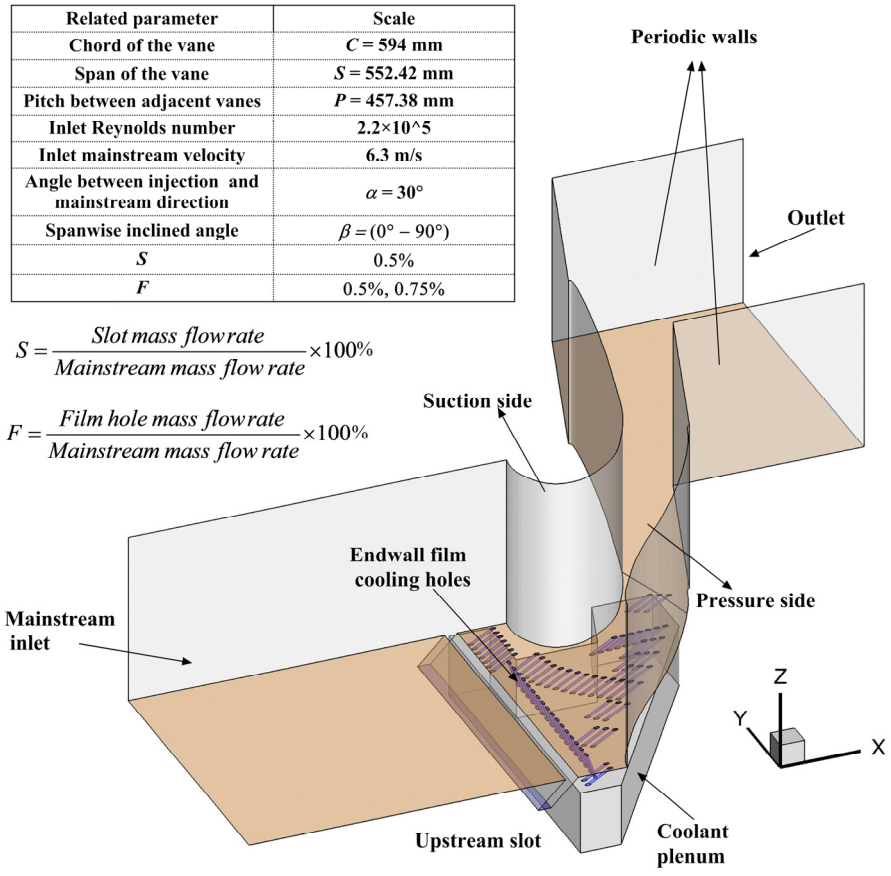


Figure 4.11 Computational domain and related parameters.

Figure 4.12 shows the endwall film hole designs and corresponding reference lines based on pressure coefficient distributions. The pressure distributions are obtained by calculations without endwall film holes. The film cooling holes are placed along the design baseline with $P/d$ fixed at 3. In Design 1, normal cylindrical holes ($\beta$ = 0º) are adopted. In design 2, the film holes locations are the same as in Design 1, but compound angle holes are adopted. The spanwise inclination angle ($\beta$) is changing between 45º, 60º, 70º, 80º and 90º as mainstream is developing along vane passages. The ejection angles of film cooling holes are more consistent with the mainstream flow direction in Design 2.

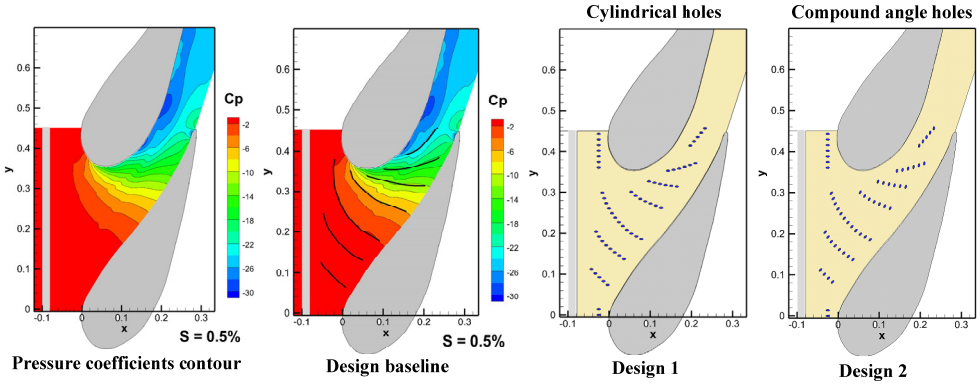


Figure 4.12 Endwall film cooling designs based on pressure coefficients distribution. Design 1: normal cylindrical holes and Design 2: compound angle holes.

Figure 4.13 presents the endwall film hole design based on streamline distributions (Design 3) and heat transfer coefficient distributions (Design 4). Similar to those shown in Figure 4.12, the streamline distributions and the heat transfer coefficients are obtained by calculations for the case of only upstream slot injection considered. Corresponding design baselines are also provided in the figure. The film cooling holes are arranged with $P/d$ fixed at 3. The total number of film holing holes is ranging from 40 to 60 for all the designs.

Structured meshes are applied to improve calculation accuracy and efficiency. In the near wall regions, the meshes should be dense to meet the requirement of the turbulence model. For the cylindrical holes and vane body regions, O-block strategy is applied to improve mesh quality. The structured meshes in some typical regions are shown in Figure 4.14. The total mesh is about 11 million, changing a little for different designs. A mesh independence study can be found in the attached **Paper VII**.

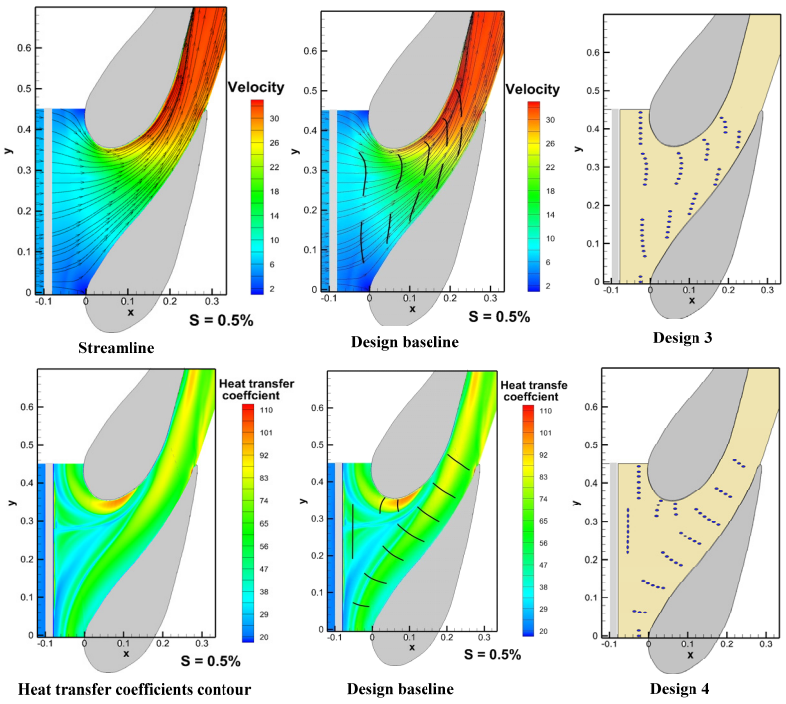


Figure 4.13 Endwall film cooling designs based on streamline distribution (Design 3) and heat transfer coefficients contour (Design 4).

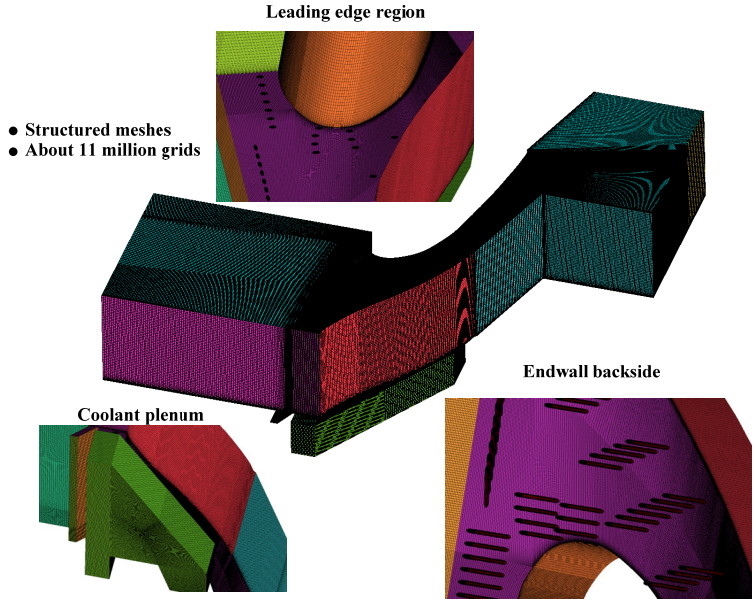


Figure 4.14 Structured meshes in some regions of the computational domain.

### 4.7.2 Selection of turbulence model

In this study, the *k-ω* SST model is applied. In Figure 4.9, the *k-ω* SST has shown its good ability in predictions of pressure coefficient distribution and endwall heat transfer around the turbine vane. In this part, the calculated full scale endwall film cooling results are compared with previous experimental data. The experimental data is from Knost [109] and measured by IR camera. Figure 4.15 shows the comparisons of calculated endwall film cooling contours with previous experimental results. The cases without an upstream slot at different film hole mass flow ratios (*F*) are used for comparisons. Two previous design patterns are compared. All the calculated results by the *k-ω* SST model have good agreements with the experimental data for both the distributions and magnitude.

Furthermore, Figure 4.16 shows the comparisons of calculated endwall film cooling contours including upstream slot with previous experimental results. The upstream slot is helpful for the coolant coverage on the endwall. The calculated results also show pretty good agreement with the experimental data. So the turbulence model, *k-ω* model, is reliable to predict the endwall film cooling effectiveness.

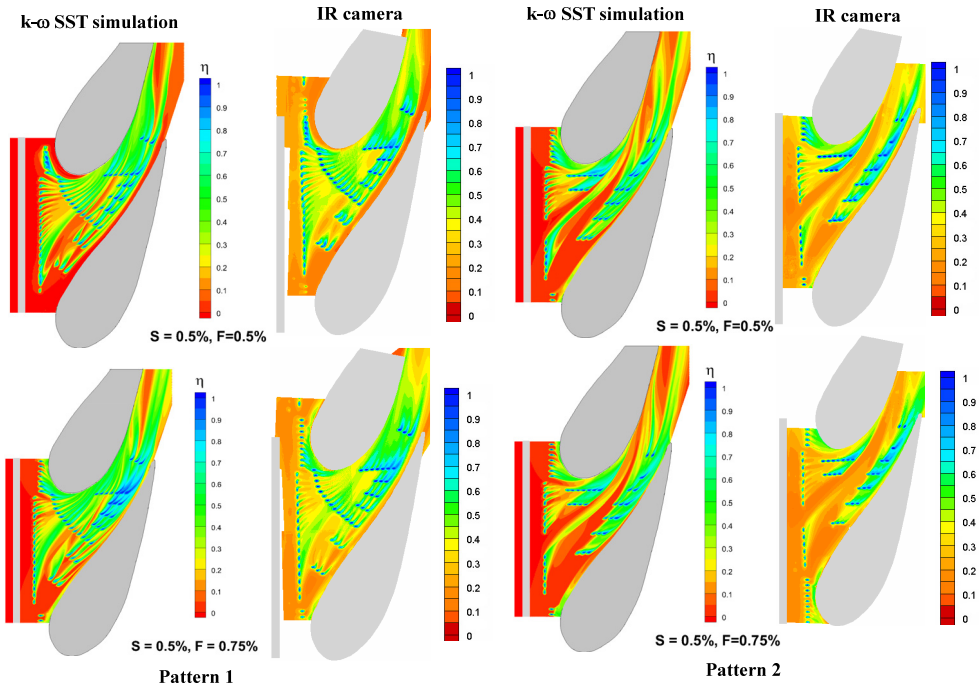


Figure 4.15 Turbulence model validations of endwall film cooling effectiveness contours. The cases without upstream slot are used for comparisons.

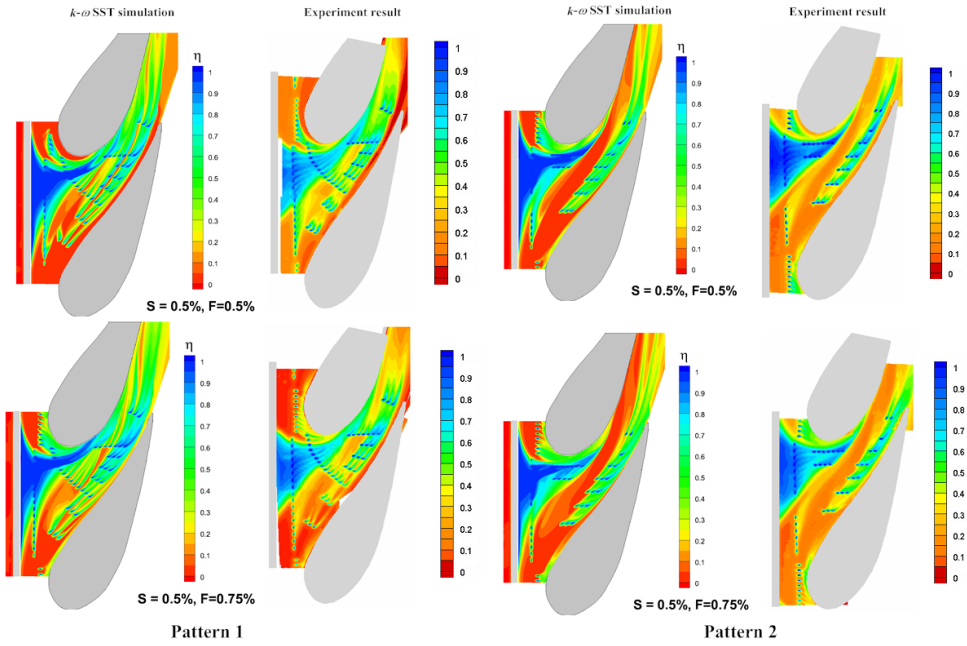


Figure 4.16 Turbulence model validations of endwall film cooling effectiveness contours. The cases with upstream slot are used for comparisons.

### 4.7.3 Computational settings

The setting of boundary condition and solver is similar to **Section 4.6.3**. Only half of the vane in the spanwise direction is considered in the computational domain to reduce calculation efforts. A symmetric wall condition is applied for the top wall. The sidewalls are set as periodic walls.

# 5 Results and Discussions

## 5.1 Pocket cavity with different fillet radii (Paper I)

➢ **Experimental results**

Figure 5.1 shows Nusselt number distributions on the heated wall with the fillet radius = 1 cm at different Reynolds numbers. The results are obtained by post-processing Liquid Crystal images. The origin is at the upstream edge of the pocket cavity. The highest heat transfer regions are located on the boundary edge of the pocket cavity where the flow attachment happens. The lowest heat transfer regions are found inside the pocket cavity where recirculating flows are formed inside. With increased Reynolds number, the heat transfer on the pocket surfaces becomes larger. It should be noted that the low heat transfer area becomes smaller in the regions close to the sides which indicates a smaller flow recirculation near the sidewalls. The reattachment expands on the flat area downstream of the pocket cavity and the highest heat transfer regions expand on the adjacent flat area with increased Reynolds number.

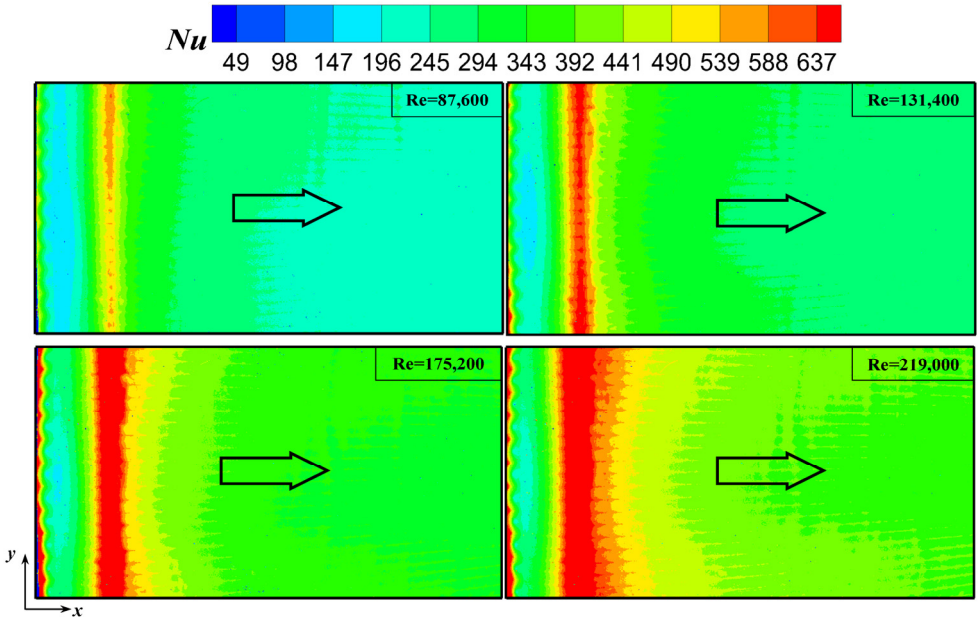


Figure 5.1 Nusselt number distributions on the heated walls with fillet radius = 1 cm at different Reynolds number obtained by LCT.

In order to investigate effect of the fillet radius, a comparison of the Nusselt number along the centerline of the heated bottom wall with different fillet radii at Reynolds number = 87,600 is provided in Figure 5.2. It is found that the peak value obtained by the smaller fillet radius is much larger than that from the larger fillet radius. Compared with the case with fillet radius = 1 cm, the Nusselt number is decreased about 25% when the fillet radius = 2 cm is used to connect the edges. However, the Nusselt number is almost the same for the two cases downstream the pocket cavity region.

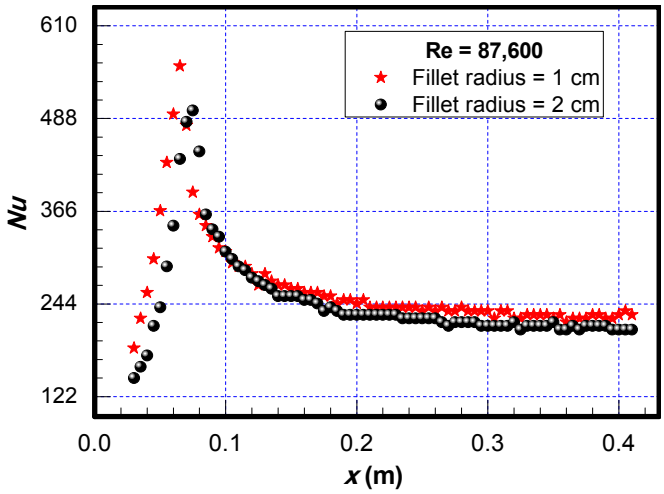


Figure 5.2 Comparisons of Nusselt numbers along the centerlines of the heated bottom walls for different fillet radius at Re = 87,600.

➢ **Calculated results**

Figure 5.3 presents distributions of streamlines and turbulent kinetic energy (TKE) on the *x-z* section of the middle heated parts at Re = 87,600. The *x-z* section is picked through the centerline where *y* is set as 0. The recirculation is located inside the pocket cavities. High TKE regions are found where the flow separation and impingement happen. However, it seems that the recirculating flow scale depends on the variation of the fillet radii. The high TKE regions expand on the flat areas with increased fillet radii, which also indicate relatively high heat transfer in this region. When the flat surfaces are included, the averaged Nusselt number should be relatively high for the case with large fillet radius.

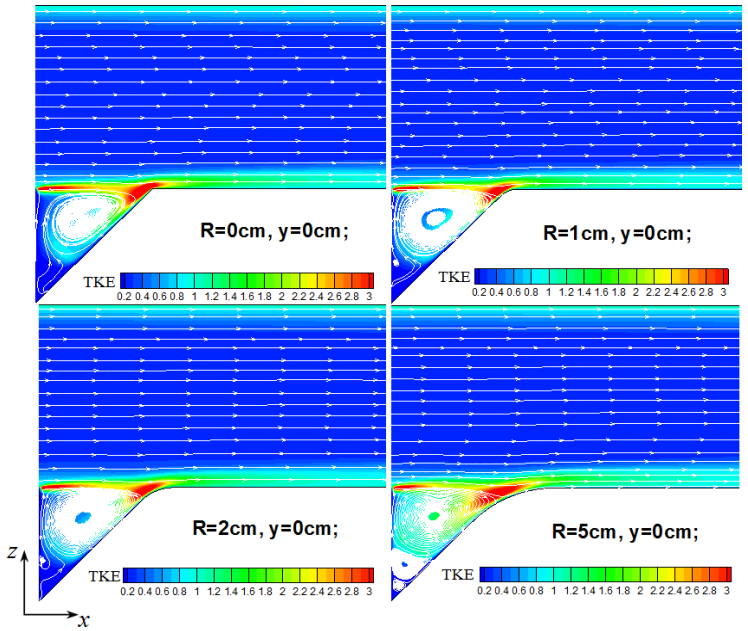


Figure 5.3 Streamlines and Turbulent Kinetic Energy ($m^2/s^2$) distributions on the centerline ($x$-$z$) section of the middle heated part at Re = 87,600.

## 5.2 Pocket cavity with a symmetrical vane (Paper II)

➢ **Experimental results**

Nusselt number distributions on the bottom walls for different cases are presented in Figure 5.4 at Re = 87,600. The origin is set as at the center of the symmetric vane. Case 0 is the smooth channel without the pocket cavity. From Case 1 to Case 3, the distance between the pocket cavity and the symmetrical vane is increased from $d_L/d$ = 1 to $d_L/d$ = 3. For Case 0, the highest Nusselt number is obtained in the region around the vane. The Nusselt number distributions around the symmetrical vane are a little increased when the pocket cavity is gradually placed far away as from Case 1 to Case 3. It can be expected that the Nusselt number distribution of Case 3 is similar to Case 0 as the pocket cavity is placed far away from the symmetrical vane. In Case 1, the high Nusselt number region caused by the cavity can also be found in regions where $x/D$ = -1. On the other hand, in Case 2 and Case 3, this phenomenon is not so clear.

The averaged Nusselt number distributions along the centerline in the streamwise direction at Re = 87,600 is presented in Figure 5.5. As expected, the Nusselt number is increased from $x/D$ = -1.0 to $x/D$ = -0.5 for all cases. The highest Nusselt number is found at the stagnation point for Case 0. From Case 1 to Case 3, the highest Nusselt number at the stagnation point for different cases is slightly increased. Also, the enhanced effect by the pocket cavity is also revealed in Case 1 where it has high Nusselt number in the region where $x/D$ ranges from -1.0 to -0.8.

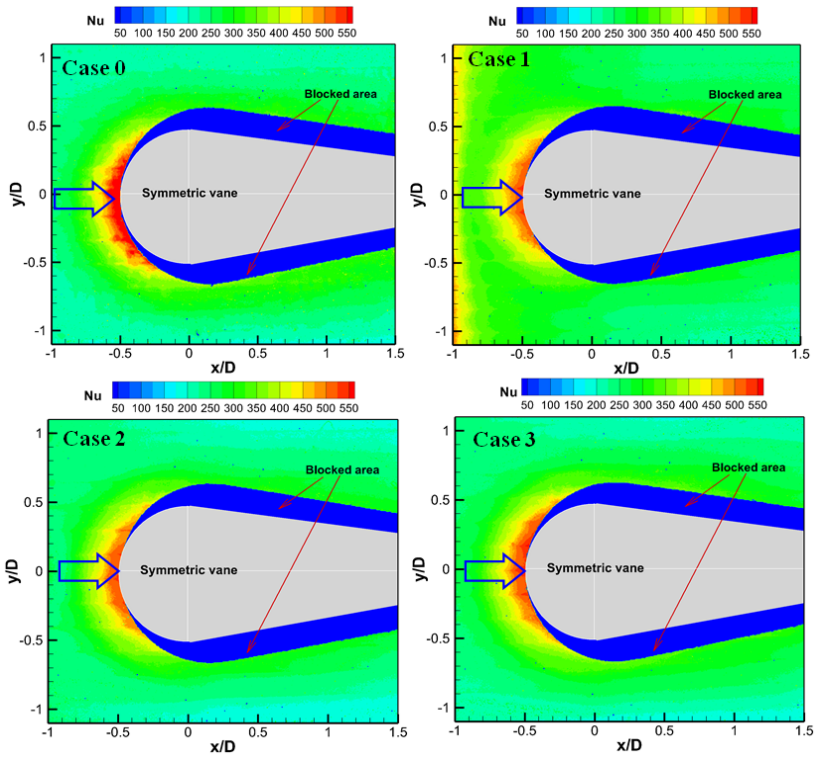


Figure 5.4 Experimental Nusselt number contours on the endwall for different cases at Re = 87,600.

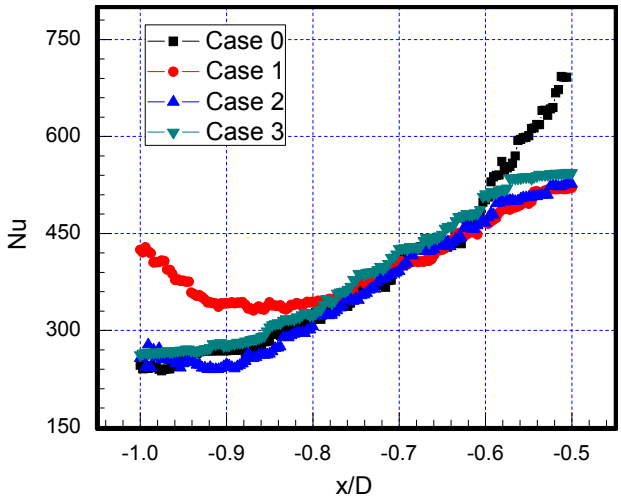


Figure 5.5 Experimental averaged Nusselt number distributions along the centerline upstream of the symmetric vane for different cases at Reynolds number = 87,600.

➢ **Calculated results**

The TKE distributions and streamlines on the *y-z* sections are displayed in Figure 5.6. The results are predicted by the *k-ω* SST model at Re = 87,600. The *y-z* sections are chosen at *x/D* = -0.5 and *x/D* = 3.5 based on the center of the vane. The high TKE regions for all cases are found near the boundary layer and the regions near the edge of the symmetrical vane surfaces. The TKE in the rear part of the symmetrical vane in Case 1 is the largest among all cases. The high TKE in this region is caused by the vortex structures caused by the symmetrical vane. This phenomenon indicates that the vortex structures shed from the pocket cavity are strong in Case 1. When the pocket cavity is placed close to the symmetrical vane, the flow is pushed upward in Case 1. The upward flow is in Case 2 and Case 3 and has almost disappeared in Case 0.

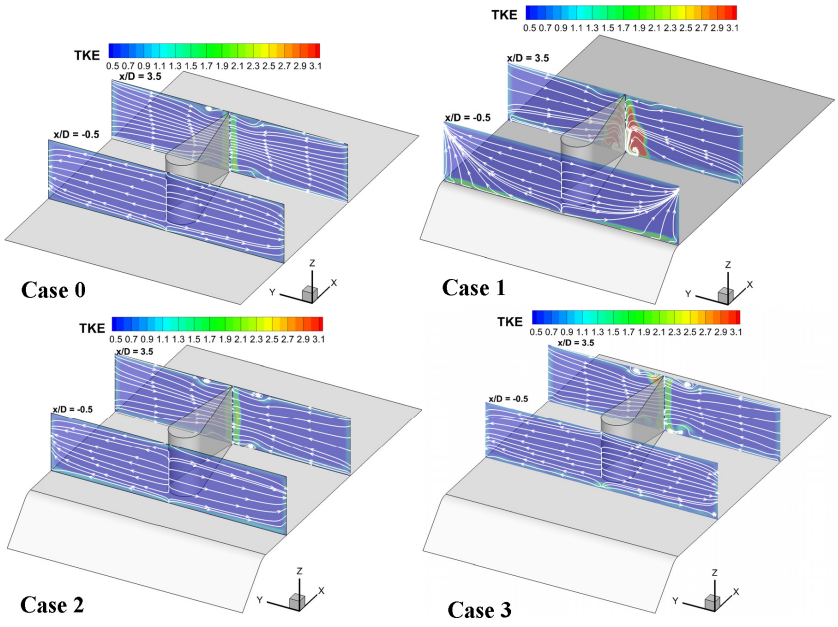


Figure 5.6 Streamlines and turbulent kinetic energy ($m^2/s^2$) on the *y-z* sections at Re = 87,600 by *k-ω* SST model. The two sections are *x/D* = -0.5 and *x/D* = 3.5, respectively.

## 5.3 Pocket cavity at different flow attack angles (Paper III)

Nusselt number distributions on the endwall of the OGV with a pocket cavity (Case 2, *L/D* = 2) at different flow attack angles at Re = 160,000 are provided in Figure 5.7. In addition, the results of the DES model and *k-ω* SST model are compared. Three different flow attack angles are applied, respectively, -30º, 0º and +30º. With different flow attack angles, the high Nusselt number regions around the OGV are changed. From the figure, the high heat transfer region is really drawn back for the flow attack angle = +30º (Case 2b). When the flow attack angle is changed to -30º (Case 2c), the high Nusselt number regions are greatly enlarged not only on the suction side but also

on the pressure side. For Case 2c, the flow impingement on the vane surfaces becomes stronger and enhances the flow mixing. In the case of the flow attack angle = 0º (Case 2a), the Nusselt number distribution is moderate compared to the other two cases. For the results of the *k-ω* SST model, the high Nusselt number regions are relatively larger than those predicted by the DES model. The DES model can avoid the over-production of turbulent kinetic energy *k* compared to the *k-ω* SST model. The effect of the flow attack angle shows the same trend for both turbulence models. Because the *k-ω* SST model is a steady simulation, the unsteady flow characteristics of the pressure side are difficult to capture of the vane which is obvious when the flow attack angle is set as -30º (Case 2c). Under this flow attack angle, the vane has a large blocking ratio relative to the mainstream and cause strong vortex streets. For the DES model, the results are time-averaged to provide more reasonable references for the overall heat transfer characteristics. However, the location of the high Nusselt number region over the pocket surface is changed for different flow attack angles. Overall, the Nusselt number over the pocket surface is much smaller than in the region near the vane.

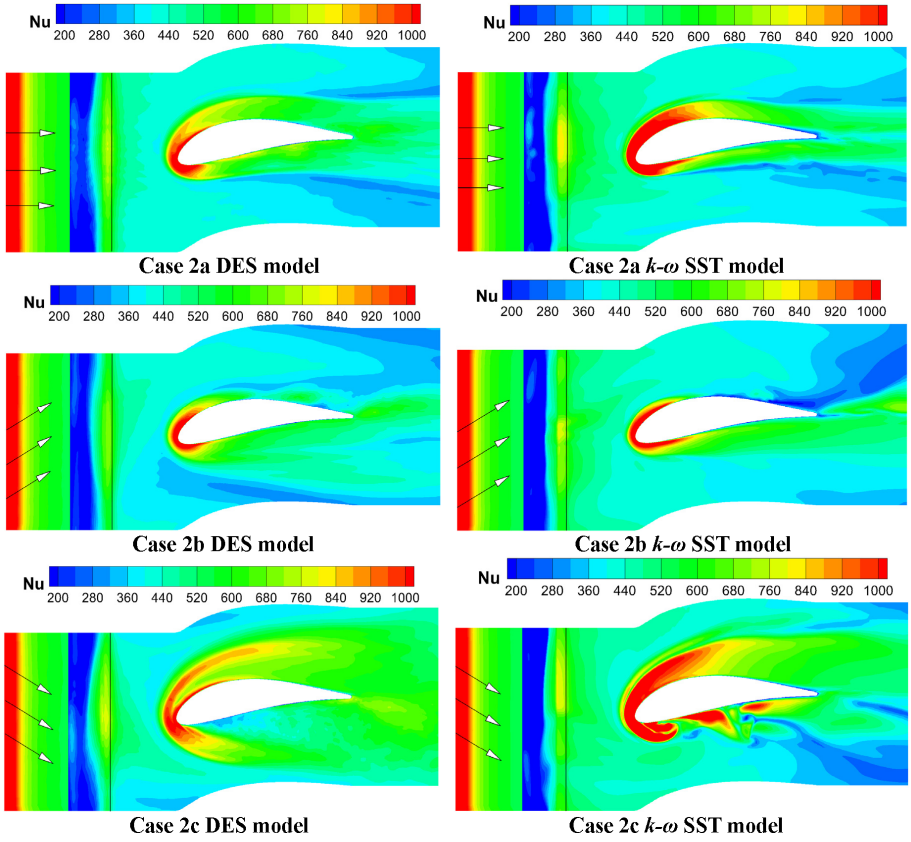


Figure 5.7 Nusselt number distributions on the endwall of an OGV with pocket cavity (Case 2) for different flow attack angles. The results of the DES model and *k-ω* SST model are compared.

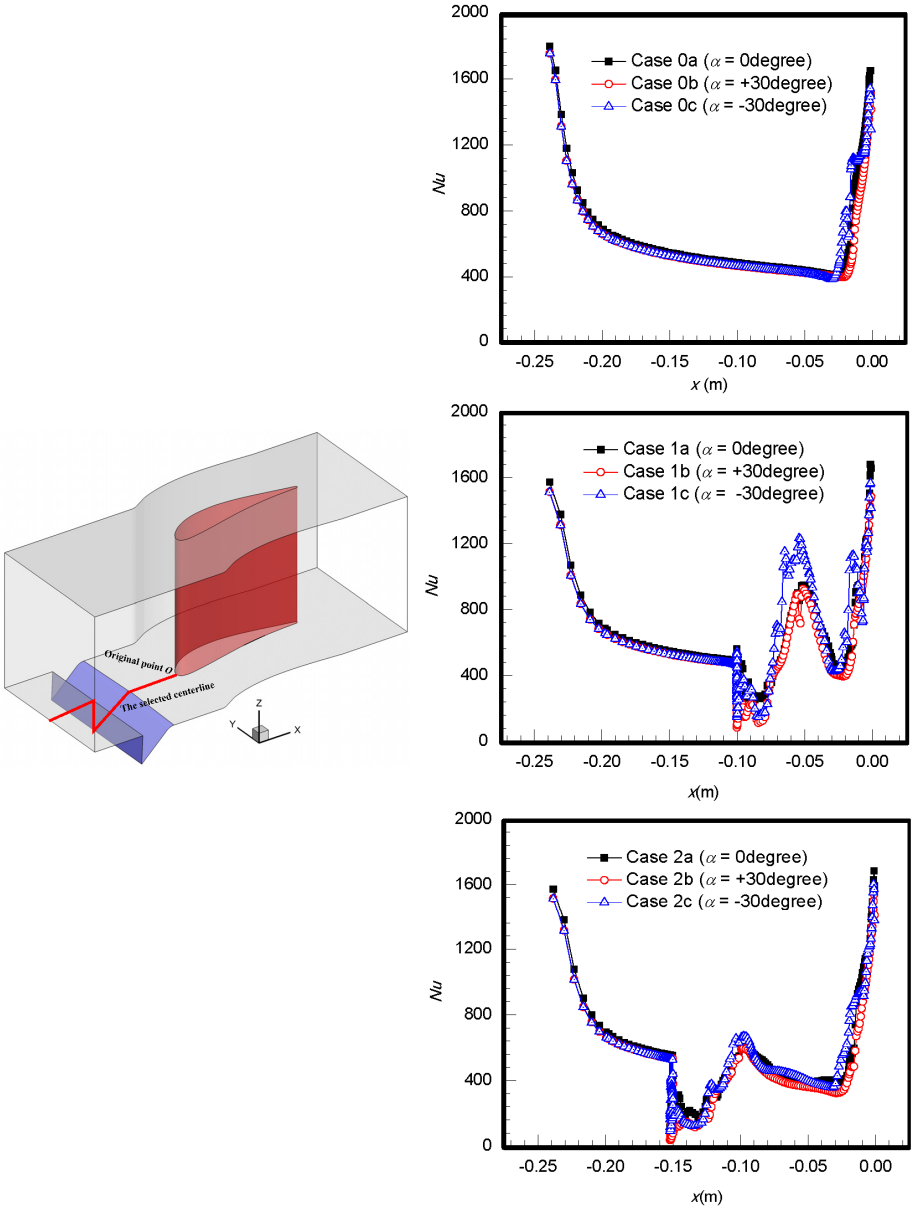


Figure 5.8 Comparisons of Nusselt number distributions along the centerline with different flow attack angles by the DES model.

The Nusselt number distributions along the centerline for different flow attack angles at Re = 160,000 by the DES model are presented in Figure 5.8. The centerline is marked on the left side of the schematic configuration. There are two peaks in the distribution along the centerline in the case without the pocket cavity (Case 0). The

first peak is because of the thermal boundary development at the inlet. The second peak is caused by the strong flow impingement on the vane surfaces. There are three peaks in the figure of Case 1 and Case 2. The third peak is located on the downstream edge of the pocket cavity. Low heat transfer can be found in Case 1 and Case 2 which is caused by the flow recirculation inside the pocket cavity. It seems that the flow attack angle has little effect on the Nusselt number distributions along the centerline. All the distribution curves converge and only small fluctuations can be found near the heat transfer peak region. Obviously, the peak value on the edge of the pocket cavity is much larger when the pocket cavity is placed near the vane especially when the flow attack angle is -30 º.

## 5.4 Truncated ribs (Paper IV)

➢ **Experimental results**

The Nusselt number contours of the ribbed walls for the parallel cases at Re = 80,000 by LCT experiments are shown in Figure 5.9. The ribbed channels with parallel arrangements include Case 1 (Traditional Continuous Ribs), Case 2 (Middle Truncated Ribs), Case 3 (Three Sides Equally Truncated Ribs), Case 4 (One Side Truncated Ribs) and Case 5 (Two Sides Truncated Ribs). The selected region between rib rows 3 and 5 is captured by the CCD camera. Between two rows, the Nusselt number in the streamwise direction first increases and then decreases. The lowest heat transfer areas are mainly found downstream the ribs due to the flow recirculation. In the spanwise direction, the high Nusselt number region is increased somewhat from the centerline to the two sidewalls. When the ribs are truncated by a small gap, the flow structure is changed and the recirculating flows behind the ribs are decreased due to the transverse flows. Transverse vortices are induced by a large pressure difference in the spanwise direction in the gap region of the truncated ribs. The wake area behind the truncated rib is similar to that of a bluff body with strengthened transverse flows. From the figure, it is obvious that local heat transfer coefficients near the truncation gap are enhanced in the ribbed channel with truncated ribs.

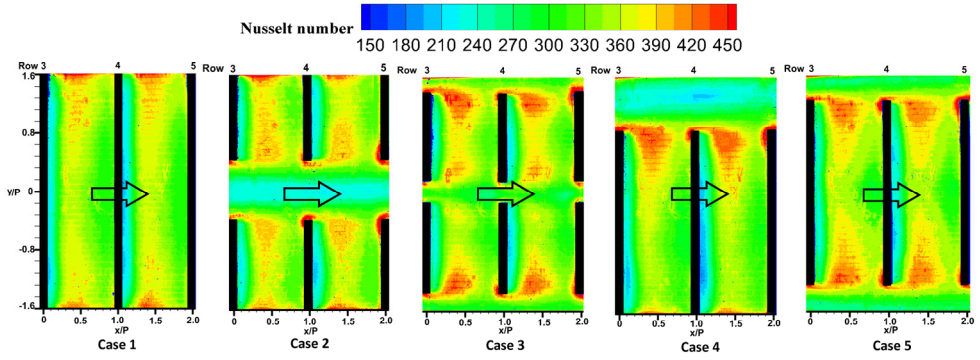


Figure 5.9 Nusselt number contours of the ribbed walls for the parallel cases by LCT experiments at Re = 80,000 (Cases 1-5).

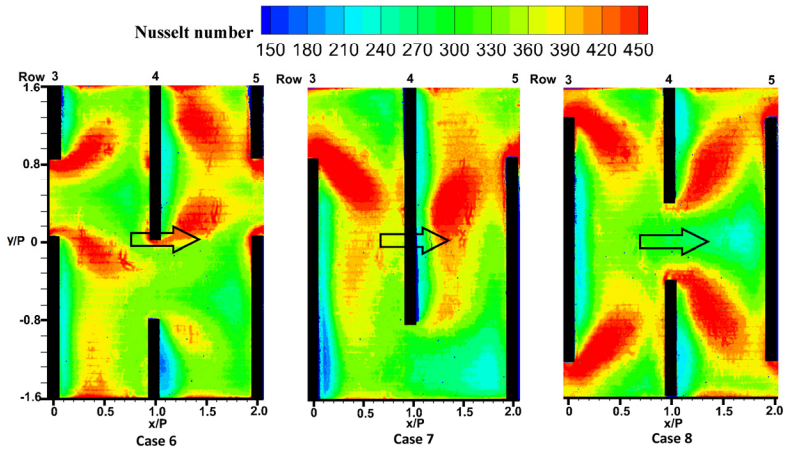


Figure 5.10 Nusselt number contours of the ribbed walls for the staggered cases by LCT experiments at Re = 80,000 (Cases 6-8).

Figure 5.10 presents the Nusselt number contours of the ribbed walls for the staggered cases by LCT experiments at Re = 80,000. The staggered cases include Case 6 (Staggered Middle Truncated Ribs), Case 7 (Staggered One Side Truncated Ribs) and Case 8 (Two Sides with Middle Truncated Ribs). These cases are designed to strengthen the transverse flows and reduce the recirculating flows. By the staggered arrangements, the high Nusselt number areas expand along the spanwise direction. Generally, the staggered cases have larger heat transfer enhancement than the parallel cases. Also, the heat transfer distribution becomes more uniform in the staggered cases. The truncation causes an unbalance of pressure behind the ribs and brings in the transverse flow from the "truncation gap". The forced transverse flow breaks up the boundary layers and mix with the mainstream flow along the spanwise direction. The averaged Nusselt number of Case 8 (Two Sides with Middle Truncated Ribs) is the largest compared to the other two staggered cases. The non-symmetric Nusselt number distributions of Case 6 and Case 7 are due to the limited rib rows in front of the captured areas. The arrangement of the upstream rib rows has effects on the distributions of the two sides in the staggered cases, such as Case 6 and Case 7. In the simulations, the same phenomenon is found for these cases.

A comparison of the thermal performance for all cases is shown in Table 5.1. The Nusselt number and friction factor are normalized by the Dittus-Boelter correlation [100] and the Blasius equation, respectively. The averaged Nusselt number is achieved by averaging the Nusselt number in the selected regions. The region covers the main characteristics of the heat transfer distributions. The averaged Nusselt number is expressed as:

$$\overline{Nu} = \frac{\int_{-1.5(z/P)}^{+1.5(z/P)} \int_{0.15(x/P)}^{0.85(x/P)} Nu(x,z)dxdz + \int_{-1.5(z/P)}^{+1.5(z/P)} \int_{1.15(x/P)}^{1.85(x/P)} Nu(x,z)dxdz}{A} \quad (5\text{-}1)$$

where $A$ is the total area of the selected area.

Table 5.1 Thermal performance comparison

| Arrangements | $\Delta P$(Pa) | $f$ | $Nu_{avg}$ | $Nu/Nu_0/(f/f_0)$ | $Nu/Nu_0/(f/f_0)^{1/3}$ |
|---|---|---|---|---|---|
| Case 1 | 40.4 | 0.01407 | 343.5 | 0.68739 | 1.42843 |
| Case 2 | 35.6 | 0.01239 | 337.6 | 0.76668 | 1.46435 |
| Case 3 | 36.2 | 0.01260 | 345.3 | 0.77117 | 1.48943 |
| Case 4 | 35.2 | 0.01226 | 336.1 | 0.77194 | 1.46335 |
| Case 5 | 36.6 | 0.01274 | 361.7 | 0.79897 | 1.55447 |
| Case 6 | 40.0 | 0.01393 | 361.8 | 0.73125 | 1.50953 |
| Case 7 | 40.4 | 0.01407 | 365.4 | 0.73122 | 1.51950 |
| Case 8 | 42.8 | 0.01490 | 370.2 | 0.69928 | 1.51013 |

For the parallel cases (Cases 2 to 5), the pressure drop is usually smaller than that of the continuous ribs (Case 1). Case 2 and Case 4, which are only partly truncated, have the smallest pressure drop. For the staggered cases, the pressure drop is similar to that of the continuous ribs except that case 8 is a little larger. Even though the pressure drop of the parallel cases is somewhat smaller, the averaged Nusselt number is still similar or higher than for the continuous ribs. Case 3 and Case 5 have the largest heat transfer due to the scattered high-heat-transfer regions. By comparing the contours in Figures 5.9 and 5.10, the high heat transfer regions are affected by the length of the truncated gaps in the experiments. If the truncated length is too large at a specified Reynolds number, the central region of the truncation part gives low heat transfer, such as Case 2 and Case 4. By reducing the forced mixing strength, Case 2 and Case 4 have the lowest pressure drop. The staggered cases generate stronger transverse flows and expand the high heat transfer regions without increasing the pressure drop. Therefore, Case 8 obtains the highest averaged heat transfer enhancement. The thermal hydraulic performance of the channel is given as $(Nu/Nu_0)/(f/f_0)$ and $(Nu/Nu_0)/(f/f_0)^{(1/3)}$. Case 5 presents the highest thermal performance with a relatively small pressure drop and a relatively high averaged Nusselt number. Overall, all the channels with truncated ribs have better thermal performance than the continuous rib one.

- **Calculation results**

The limiting streamline approaching the ribbed walls for the parallel cases at Re = 80,000 is presented in Figure 5.11. The limiting streamline means the streamline on the mesh of the first layer approaching the ribbed bottom wall. Flow recirculation and flow reattachment can be found between two adjacent rib rows. When the rib is truncated, a transverse vortex can be found at the truncation gap, which increases the turbulent flow mixing with the mainstream flow. The vortex strength is affected by the size of the truncated gap and it is enlarged at a larger truncated gap. From the figure, it is evident that the discrete truncated parts induce discrete vortices and improve the flow mixing. Therefore, higher heat transfer is presented in both Case 3 and Case 5.

Figure 5.12 presents the limiting streamline approaching the ribbed walls for the staggered cases at *Re* = 80,000. The staggered arrangement changes the flow patterns between two adjacent rows and creates relatively complex flow paths for the incoming flow. This enhanced flow mixing effectively breaks the boundary layer and increases the flow mixing and heat transfer. However, the more complex flow path also contributes to higher pressure drop for the staggered cases. In general, the transverse flow caused by the truncated ribs decreases the flow recirculation regions behind the ribs and then increases the heat transfer.

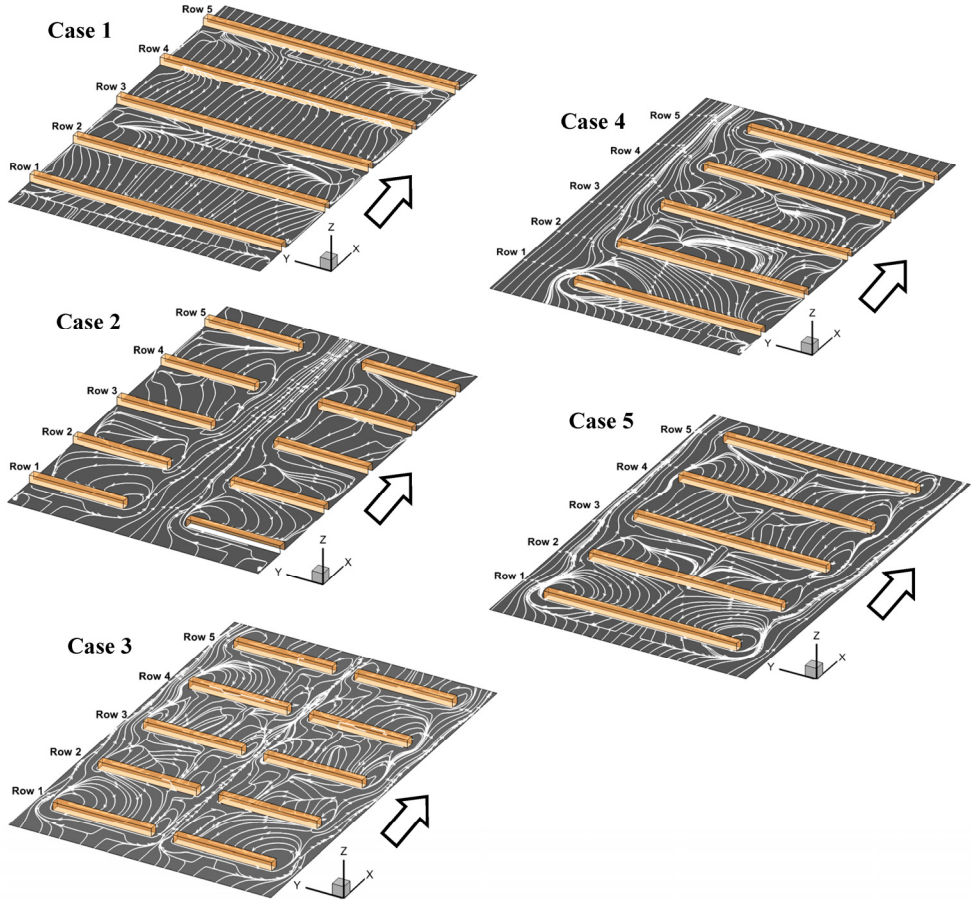


Figure 5.11 Limiting streamline approaching the ribbed walls for the parallel cases at Re = 80,000.

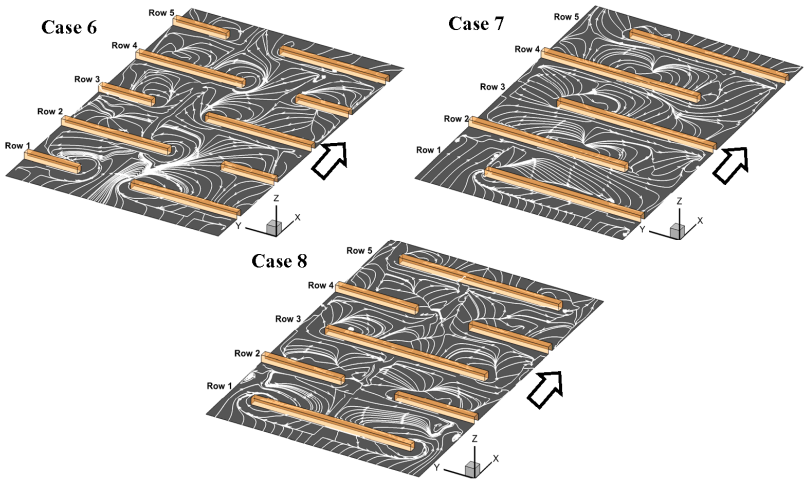


Figure 5.12 Limiting streamline approaching the ribbed walls for the staggered cases at Re = 80,000.

## 5.5 Perforated ribs (Paper V)

➢ **Experimental results**

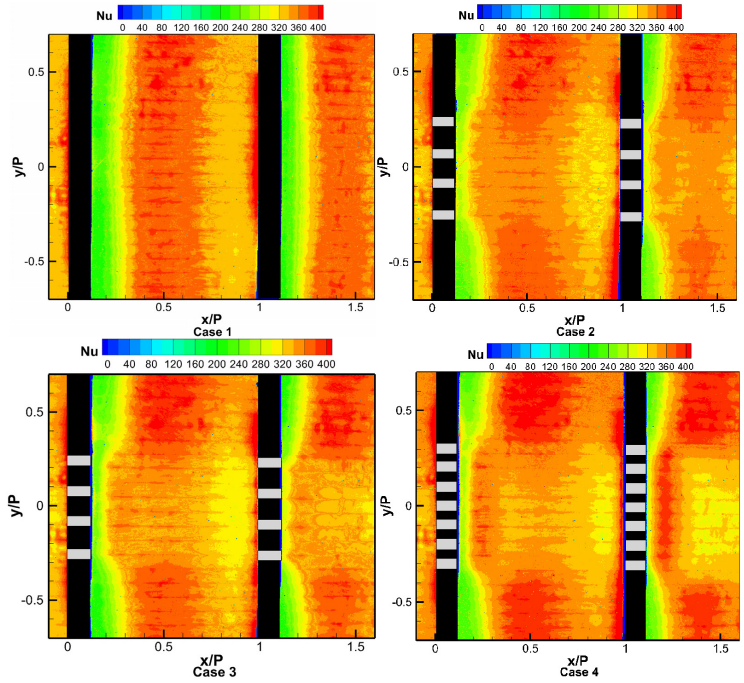


Figure 5.13 Nusselt number contours on the tested surface for the differently perforated ribs at Re = 80,000 by LCT experiments.

The Nusselt number contours of the perforated ribbed surfaces for all the cases at Re = 80,000 provided by LCT experiments are shown in Figure 5.13. The camera focuses on one row of the perforated rib to obtain high resolution results. The high heat transfer regions are usually located in the middle part between two adjacent rib rows caused by the flow reattachment and re-development of the boundary layer. The low heat transfer regions are found behind the ribs due to the recirculating flows. In the region approaching the next rib, the heat transfer is also increased with the increased flow impingement. Compared with the normal rib in Case 1, the low heat transfer behind the ribs for the perforated cases (Cases 2-4) is greatly improved. This phenomenon is more obvious if the perforation ratio is increased, i.e., Case 4. When the perforation ratio is increased (Case 4), the heat transfer field also becomes more uniform, which is a big concern in the cooling design of a turbine blade. However, it seems that the high heat transfer in the flow reattachment region is somewhat weakened in the perforated cases as the flow reattachment is also affect by the penetrated flows.

**Region 1**

$$\overline{Nu} = \frac{\int_{-0.4(y/P)}^{+0.4(y/P)} \int_{0.12(x/P)}^{0.97(x/P)} Nu(x,y)dxdy}{A}$$

| *Nu* | Case 1 | Case 2 | Case 3 | Case 4 |
|---|---|---|---|---|
| Re = 40,000 | 220.1 | **234.2 (+6.40%)** | **233.5 (+6.08%)** | **238.1 (+8.17%)** |
| Re = 80,000 | 320.0 | **339.7 (+6.15%)** | **333.5 (+4.21%)** | **340.7 (+6.46%)** |

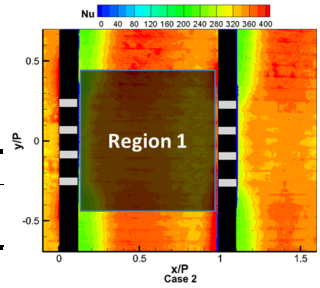


**Region 2**

$$\overline{Nu} = \frac{\int_{-0.4(y/P)}^{+0.4(y/P)} \int_{0.12(x/P)}^{0.32(x/P)} Nu(x,y)dxdy}{A}$$

| *Nu* | Case 1 | Case 2 | Case 3 | Case 4 |
|---|---|---|---|---|
| Re = 40,000 | 162.6 | **200.9 (+23.55%)** | **201.7 (+24.04%)** | **202.3 (+24.41%)** |
| Re = 80,000 | 265.3 | **297.8 (+12.25%)** | **301.8 (+13.75%)** | **309.2 (+16.55%)** |

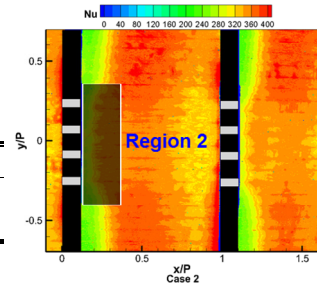


Figure 5.14 Comparisons of the averaged Nusselt number for all the cases.

The averaged Nusselt number on the heated surfaces for all the perforated rib cases are presented in Figure 5.14. Two averaged regions are chosen, Region 1 and Region 2, respectively. Region 1 is the whole heated region around the perforated ribs and Region 2 is the region close to the ribs where the recirculating flows exist. The correlations for the two regions are expressed as

$$\overline{Nu} = \frac{\int_{-0.4(y/P)}^{+0.4(y/P)} \int_{0.12(x/P)}^{0.97(x/P)} Nu(x,y)dxdy}{A} \quad (5\text{-}2)$$

$$\overline{Nu} = \frac{\int_{-0.4(y/P)}^{+0.4(y/P)} \int_{0.12(x/P)}^{0.32(x/P)} Nu(x,y)dxdy}{A} \tag{5-3}$$

The averaged Nusselt numbers at different Reynolds numbers are compared. Case 1 is the normal rib case. For the whole region, i.e., Region 1, the heat transfer enhancement by the perforated ribs is about 5%. The heat transfer enhancement factor does not change so much for differently-perforated ribs. Case 4 obtains a little larger heat transfer enhancement. Also, the heat transfer enhancement is a little larger at the low Reynolds number. However, for Region 2, the local heat transfer is enhanced by 10-20% for all the perforated cases. Region 2 is the main region where the perforated ribs take effects. The relative small heat transfer enhancement in Region 1 is caused by the weakened heat transfer in the flow reattachment region by the perforated ribs. Overall, the heat transfer field for the perforated cases is more uniform.

- **Calculated results**

The turbulent kinetic energy (TKE) distributions and streamlines on the *x*-*y* section (*z*/*e* = 0.5) for all the cases are presented in Figure 5.15. Similar to the heat transfer distributions, the turbulent kinetic energy distribution changes depending on the different flow structures. In the flow recirculation region, the turbulent kinetic energy is relatively small. In the flow reattachment region, the turbulent kinetic energy is relatively high. The turbulent kinetic energy is decreased when approaching the next rib, in agreement with the heat transfer distribution. The low and high TKE regions are disturbed by the perforated ribs. The low turbulent kinetic energy region is increased and the high TKE is decreased for the perforated cases. It is evident that the recirculating flows are reduced in the perforated cases and the flow reattachment is disturbed by the perforated holes. When the perforation ratio is increased (Case 4), the high turbulent kinetic energy region is greatly reduced. This phenomenon is also found in the streamline distribution. Obvious flow recirculation and flow reattachment in the streamline distribution for Case 1 can be observed. The reattachment line, which is the dividing border of the flow recirculation and flow reattachment region, is also displayed in the figure. However, for the perforated cases, no reattachment line can be found and the flow recirculation region is greatly reduced. With the increased perforation ratio, the flow field becomes more uniform.

The TKE distributions and streamlines on the *x*-*z* section for all the cases predicted by the *k*-*ω* SST model are shown in Figure 5.16. The selected *x*-*z* section, *y* = 0, is through the centerline of the channel. In the near wall region, the TKE is usually high. For the ribbed case, the TKE is greatly enlarged by the flow separation and reattachment. For the perforated cases, the TKE energy region is reduced compared with that of the normal ribs. It also proves that the recirculation flows are greatly reduced by the perforated ribs. The shapes of the holes have little influence on the flow structures. However, the recirculating flows are further reduced with increased the perforation ratio in Case 4.

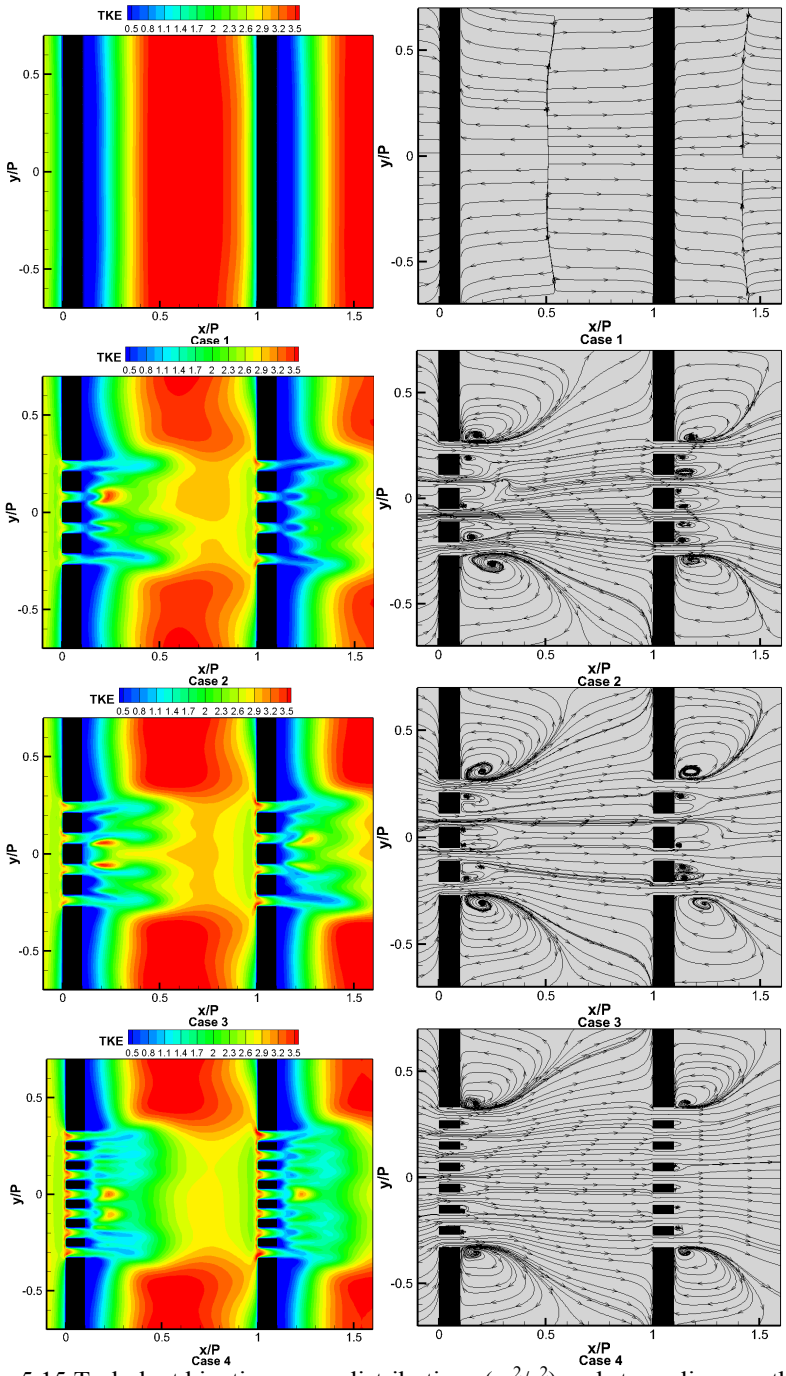


Figure 5.15 Turbulent kinetic energy distributions ($m^2/s^2$) and streamlines on the *x*-*y* sections for all the cases. The section is located at $z/e = 0.5$.

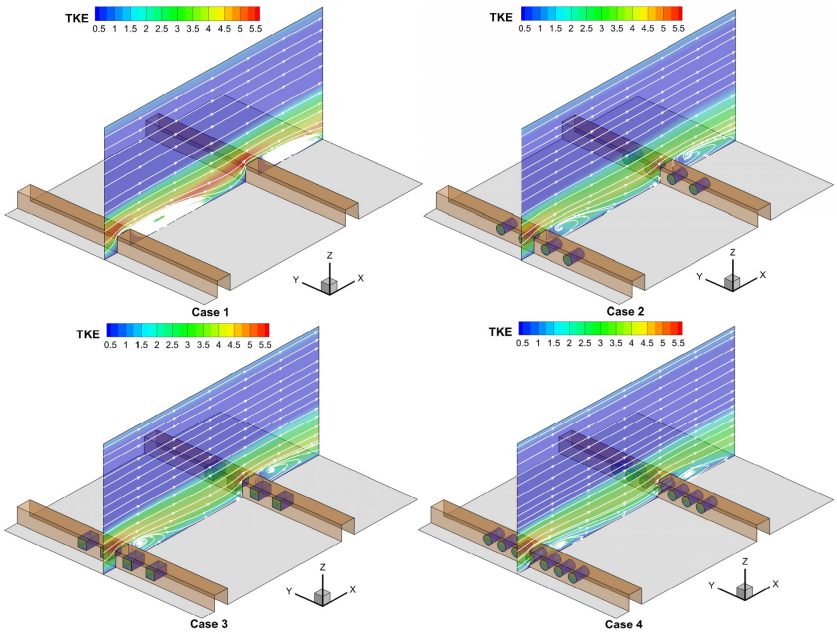

Figure 5.16 Turbulent kinetic energy distributions ($m^2/s^2$) and streamlines on the *x*-*z* section for all the cases. The section is located at the centerline of the channel.

## 5.6 Film cooling upstream of the leading edge (Paper VI)

Figure 5.17 presents the endwall cooling effectiveness for different cases at different blowing ratios. The cooling effectiveness contours at the leading edge are greatly affected by the impingement flows in the stagnation region. For Case 1, the leading edge region is well protected by single row of film cooling holes when these are placed close to the stagnation region. When the film cooling holes are placed a little far away, as in Case 2, the coolant coverage in this region is not so good. The ejected coolant flows are separated by horseshoe vortices and develop with the mainstream flow. This kind of arrangement, as in Case 1 and Case 2, seem to eject the coolant in a large area along the suction side and pressure side. However, for the two important regions, i.e., the stagnation region and junction region of the endwall and pressure side, this arrangement has no obvious improvement. Case 3 has two rows of normal cylindrical holes with staggered arrangement. This arrangement has good cooling protection for both the pressure and suction sides. However, the cooling coverage is not as large as that in Case 1 and Case 2. Case 4 has two rows of compound angle cooling holes with staggered arrangement. The compound angle holes have reversed spanwsie angles for each row of cooling holes. However, this arrangement almost has no good protection for the pressure side though it provides a relatively large cooling coverage on the endwall. In Case 6, the arrangement is similar to Case 4 with a small interval between the two rows. However, no obvious improvement can be found in Case 6. Case 5 also uses two rows of compound angle holes with staggered

arrangement. The spanwise angles of two rows are entirely reversed compared to those in Case 4. With reversed compound angles, the coolant coverage in Case 5 is greatly enlarged. Both the suction side and the pressure side of the vane are protected well. With the increased blowing ratio, the coolant strongly impinges on the leading edge and the generated horseshoe vortices develop strongly along the vane body. The strong impingement flows change the coherent flow path of the ejected coolant flows. Due to the high pressure at the stagnation region, the coolant is difficult to eject in this region. The coolant coverage on the endwall is decreased when the blowing ratio is increased. It seems that coolant coverage at the leading edge of the vane is not so greatly affected in Case 2 and Case 5 even when the blowing ratio is increased.

Three dimensional film cooling effectiveness contours of all the cases at blowing ratio = 3 are displayed in Figure 5.18. It is clear that the film cooling holes at the leading edge of the vane have effects on both the endwall region and the vane surfaces. Comparing Case 1 with Case 2, the coolant coverage on the vane surfaces is more dominant when the cooling holes are placed close to the leading edge. Case 3 also provides a good protection for both the suction side and pressure side when the cylindrical holes have staggered arrangement. For the arrangements in Case 4 and Case 6, staggered arrangement with compound angle holes, has better coolant protection on the suction side than on the pressure side. In Case 5, staggered arrangement with reversed compound angle holes is utilized and this arrangement provides good protection for both the pressure side and suction side. The figure provides more evidence that the junction region of pressure side and endwall is difficult for the coolant to approach.

The comparisons of averaged film cooling effectiveness in different regions at various blowing ratios are shown in Table 5.2. The averaged film cooling effectiveness in different regions are marked as $\eta_1$, $\eta_2$, $\eta_3$ and $\eta_4$, which, respectively, represent the averaged film cooling effectiveness on the whole endwall, the vane surface of the pressure side, the vane surface of the suction side and all the considered surfaces. Case 1 has relatively equal cooling effects for all the regions. When the film cooling holes are placed a little far away from the vane leading edge (Case 2), the averaged film cooling effectiveness on the endwall is greatly enhanced while that on the vane surfaces is greatly reduced. Using staggered arrangement of the film cooling holes (Case 3), the averaged cooling effectiveness is improved on the vane surfaces at blowing ratio = 1. For the staggered arrangement with compound angle holes, there are hardly cooling effects on the vane surfaces of pressure side in Case 4 and Case 6. By reversing the compound angle of the film cooling holes (Case 5), the cooling effects on the vane surfaces are greatly improved. In addition, the overall cooling effectiveness of Case 5 is also the highest at blowing ratio = 1. With the increased blowing ratio, the cooling effectiveness on the vane surfaces and the overall averaged cooling effectiveness are greatly increased. The cooling effects on the endwall are dominant when the blowing ratio is small. However, the cooling effects on the vane surfaces are dominant when the blowing ratio is large. Only in Case 5, the endwall film cooling holes always provides good performances at different blowing ratios.

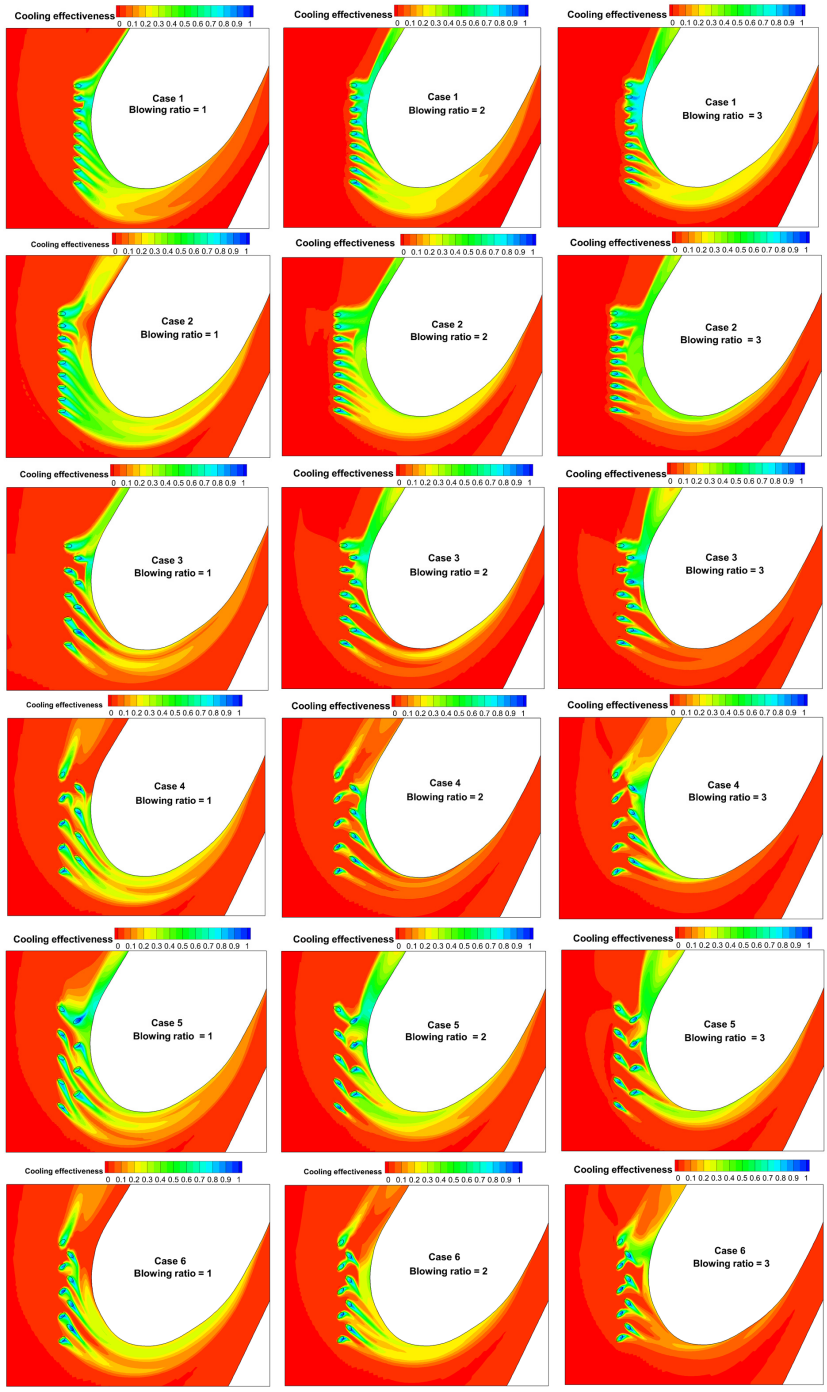


Figure 5.17 Endwall film cooling effectiveness for different cases at different blowing ratios.

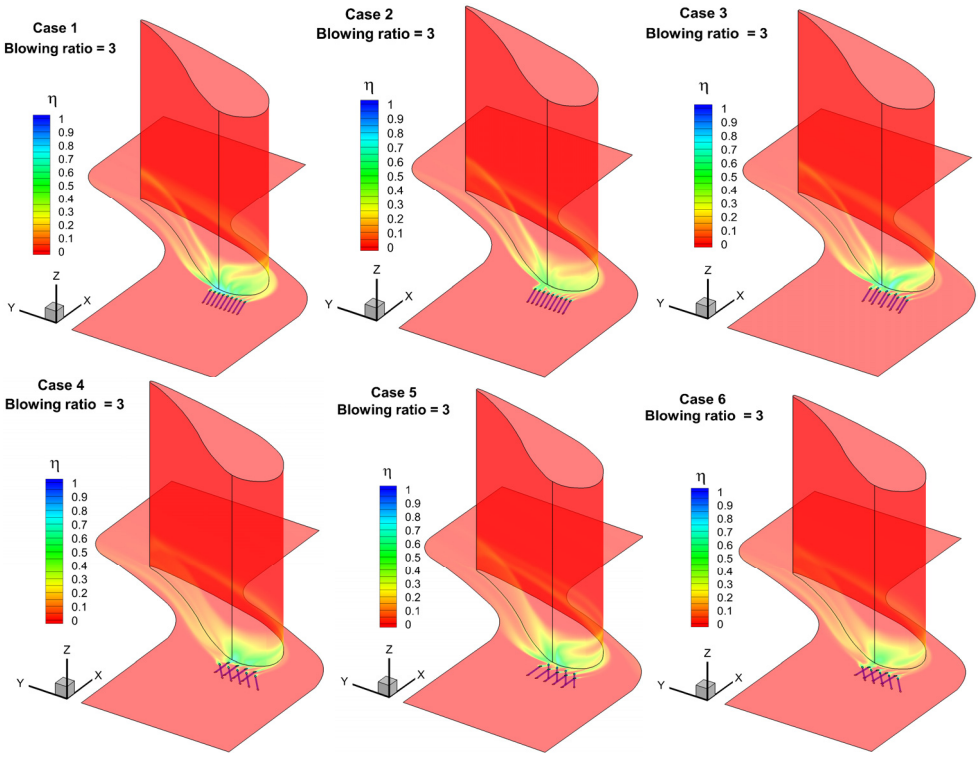


Figure 5.18 3D plot of film cooling effectiveness for different cases at blowing ratio = 1.

Table 5.2 Averaged film cooling effectiveness.

| | **Blowing ratio = 1** | | | | **Blowing ratio = 2** | | | |
|---|---|---|---|---|---|---|---|---|
| | $\eta_1\times10^3$ | $\eta_2\times10^3$ | $\eta_3\times10^3$ | $\eta_4\times10^3$ | $\eta_1\times10^3$ | $\eta_2\times10^3$ | $\eta_3\times10^3$ | $\eta_4\times10^3$ |
| Case 1 | 8.821 | 8.613 | 8.589 | 8.683 | 12.492 | 14.607 | 20.045 | 15.807 |
| Case 2 | 16.078 | 0.817 | 2.447 | 7.195 | 11.335 | 15.847 | 13.736 | 13.362 |
| Case 3 | 11.066 | 6.439 | 5.361 | 7.795 | 12.028 | 14.190 | 12.007 | 12.568 |
| Case 4 | 12.526 | 0.021 | 4.363 | 6.354 | 12.158 | 7.521 | 14.783 | 11.949 |
| Case 5 | 15.608 | 7.093 | 4.014 | 9.185 | 14.959 | 18.670 | 14.303 | 15.658 |
| Case 6 | 13.355 | 0.018 | 2.487 | 5.976 | 11.842 | 5.935 | 11.902 | 10.367 |

$\eta_1$: averaged film cooling effectiveness on the whole endwall;

$\eta_2$: averaged film cooling effectiveness on the pressure side vane surface;

$\eta_3$: averaged film cooling effectiveness on the suction side vane surface;

$\eta_4$: averaged film cooling effectiveness on the whole endwall and vane surfaces;

## 5.7 Full scale endwall film cooling design (Paper VII)

The contours of film cooling effectiveness on the endwall for different designs at various coolant mass flow rate ratios are presented in Figure 5.19. From the figure, the designs based on pressure coefficient distributions (Design 1 and Design 2) force the coolant flows from pressure side to suction side. The coolant coverage on the junction part of the pressure side and the endwall is worse compared with other designs. Also, more coolant will impinge on the suction side surfaces and is helpful for cooling of suction vane surfaces in Design 1 and Design 2. Compared with normal cylindrical holes (Design 1), the use of compound angle holes (Design 2) is easier to force more coolant to the suction surfaces and brings the worse film cooling on the endwall between vane passages. Design 3 is based on the streamline distributions which has good coolant coverage on the endwall, even in the tough region, i.e., the junction part of pressure side and endwall. In addition, when the film hole mass flow rate ratio is increased, the coolant coverage on the endwall is increased in Design 3, which is not so obvious in Design 1 and Design 3. Design 4 is based on the heat transfer coefficient distribution, which also displays good coolant coverage on the endwall at the same film cooling mass flow rate. However, the film cooling at the junction part of the pressure side and endwall is not so well as Design 3. The film cooling design based on heat transfer coefficients is helpful to reduce local high temperature region on the endwall. When the film hole mass flow rate ratio ($F$) is 0.5%, the coolant upstream of the leading edge is difficult to eject in some designs. The pressure at the stagnation region is high and the coolant cannot eject out when the coolant supply is not sufficient.

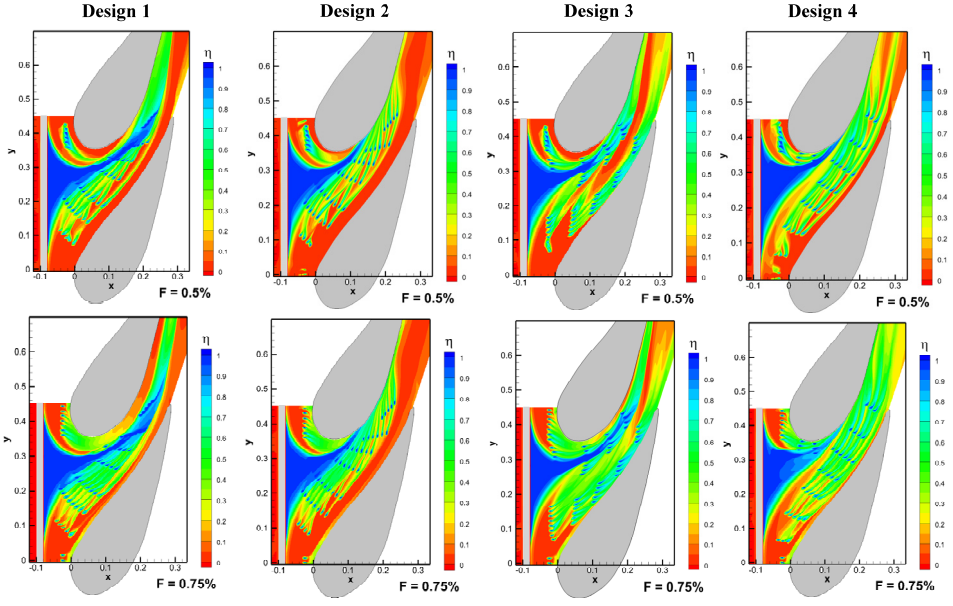


Figure 5.19 Contours of film cooling effectiveness on the endwall for different designs at various coolant mass flow rate ratios.

Figure 5.20 displays 3-D streamlines originating from the endwall film cooling holes for different designs at mass flow rate ratio = 0.75%. This figure shows how the coolant flows on the endwall interact with the mainstream horseshoe vortices. The velocity is increased in the streamwise direction. In Design 1 and Design 2, the streamlines approach the suction side. In Design 3 and Design 4, some streamlines can be found at the junction part of pressure side and endwall, while it is difficult to find such in Design 1 and Design 2.

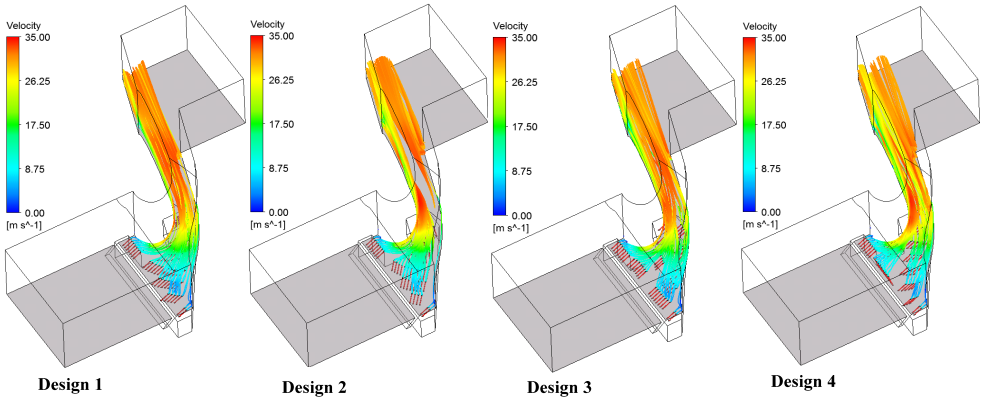


Figure 5.20 Development of three-dimensional streamlines originating from the film cooling holes on the endwall.

The averaged film cooling effectiveness on the endwall and vane surfaces is compared in Table 5.3 for all the cases. From the Table, Design 3 and Design 4 have larger averaged endwall film cooling effectiveness compared with Design 1 and Design 2. In Design 2, the averaged film cooling effectiveness on the suction side is larger than other cases. With the increased film cooling mass flow ratio, the overall film cooling effectiveness is increased for all the cases. Design 4 provides high averaged film cooling effectiveness and has advantages in removing the high temperature region on the endwall. It is recommended for the pattern of endwall film cooling.

Table 5.3 Comparison of film cooling effectiveness

| | Film mass flow rate ratio F = 0.5 | | | Film mass flow rate ratio F = 0.75 | | |
|---|---|---|---|---|---|---|
| | Endwall$\times 10^3$ | Pressure side$\times 10^3$ | Suction side$\times 10^3$ | Endwall$\times 10^3$ | Pressure side$\times 10^3$ | Suction side$\times 10^3$ |
| Design 1 | 204.75 | 0.13 | 17.27 | 226.96 | 23.68 | 23.11 |
| Design 2 | 167.96 | 0.15 | 47.19 | 181.66 | 24.75 | 80.88 |
| Design 3 | 213.55 | 13.85 | 36.71 | 243.83 | 44.84 | 44.85 |
| Design 4 | 208.78 | 0.19 | 58.00 | 258.13 | 28.27 | 78.38 |

# 6 Conclusions and Future Work

**The main conclusions emerging from this work are:**

1. Study about pocket cavity and outlet guide vane

- The smaller fillet radius provides a higher heat transfer peak value with a stronger recirculating flow inside the pocket cavity. However, the pocket cavity with the larger fillet radius can reduce the peak heat transfer values but increase the overall averaged heat transfer value of the pocket cavity surface with weakened strength of recirculating flows. (**Paper I**)
- The high Nusselt number regions upstream of the symmetrical vane are caused by flow impingement on the leading edge of the symmetrical vane and the generated horseshoe vortices. Compared with the case of the symmetric vane placed on the smooth surface, the high Nusselt number region around the symmetrical vane is decreased when the pocket cavity is placed upstream. When the distance between the pocket cavity and the symmetric vane is large, the effect of the pocket cavity is weakened. The separated flows on the endwall caused by the pocket cavity weaken the flow impingement on the symmetrical vane and lead to decreased heat transfer. (**Paper II**)
- With different flow attack angles, the high Nusselt number regions around the OGV are changed. When the flow attack angle is changed to -30º, the high Nusselt number regions are greatly enlarged not only in the suction side but also in the pressure side with strengthened flow impingement on the vane surfaces. The pocket cavity weakens the flow impingement on the vane surfaces and the effect is more obvious as the pocket cavity is placed close to the vane. On the other hand, the heat transfer distribution over the pocket surface is also affected by the location of the vane. When the vane is placed close to the pocket cavity, the heat transfer over the pocket surface is greatly enlarged. (**Paper III**)

2. Study about internal cooling using ribbed channels

- Truncated ribs can reduce the pressure loss penalty without reducing the heat transfer enhancement in the tested channels. By changing the configurations to staggered arrangements, the heat transfer can be further enhanced associated with a moderate pressure drop. The truncated ribs generate transverse vortices at the truncation gaps and reduce the recirculating flow behind the ribs. (**Paper IV**)
- Compared with the normal rib, the low heat transfer behind the ribs is greatly improved by the perforated ribs with a slightly reduced pressure drop. This phenomenon is more obvious when the perforation ratio is large. The local heat

transfer field is enhanced by about 10-24% and the overall heat transfer is enhanced by about 4-8%. Therefore, the overall thermal performance factors are improved in the perforated cases. A more uniform heat transfer field is also obtained by the perforated ribs with the reduced recirculating flows. (**Paper V**)

3. Study about endwall film cooling

- The film cooling holes, upstream the leading edge of a vane, have cooling effects on both the vane surfaces and the endwall. When the blowing ratio is increased, the cooling effectiveness on the vane surfaces is increased more quickly and becomes dominant. One single row of cylindrical holes (Case 1) and two rows of compound angle holes with staggered arrangement (Case 5) have relatively high overall averaged cooling effectiveness compared with other cases at different blowing ratios. Case 5 provides good coolant coverage on both the pressure side and the suction side and relatively good overall film cooling effectiveness which is not so affected by the changing of the blowing ratios. (**Paper VI**)
- The designs based on pressure coefficient distributions (Design 1 and Design 2) force the coolant flows from pressure side to suction side with no big change of the original pressure field. The design based on the streamline distributions (Design 3) has good coolant coverage on the endwall, even in the tough region, i.e., the junction part of pressure side and endwall. The design based on heat transfer coefficients (Design 4) also gives relatively large coolant coverage and is very helpful to reduce local high temperature region on the endwall. **(Paper VII)**

**Potential for future work**

- Using porous media or lattice structures in the leading edge of the vane to enable transpiration cooling.
- Apply new design concept in the arrangement of endwall film cooling holes, such as fractal theory.

# References


[1] L. Wang, B. Sunden, V. Chernoray, H. Abrahamsson, Endwall heat transfer measurements of an outlet guide vane at on and off design conditions, ASME Turbo Expo 2013: Turbine Technical Conference and Exposition, American Society of Mechanical Engineers, 2013, pp. V03CT14A017-V003CT014A017.

[2] C. Wang, L. Luo, L. Wang, B. Sunden, V. Chernoray, C. Arroyo, H. Abrahamsson, Experimental and numerical investigation of outlet guide vane and endwall heat transfer with various inlet flow angles, International Journal of Heat and Mass Transfer 95 (2016) 355-367.

[3] J.C. Han, S. Dutta, S. Ekkad, Gas Turbine Heat Transfer and Cooling Technology, CRC Press, 2012.

[4] J.C. Han, J.S. Park, Developing heat transfer in rectangular channels with rib turbulators, International Journal of Heat and Mass Transfer 31 (1988) 183-195.

[5] T.M. Liou, J.J. Hwang, Effect of ridge shapes on turbulent heat transfer and friction in a rectangular channel, International Journal of Heat and Mass Transfer 36 (1993) 931-940.

[6] R.J. Goldstein, Film cooling, Advances in Heat Transfer, Vol. 7, Elsevier, 1971, pp. 321-379.

[7] S. Ito, R. Goldstein, E. Eckert, Film cooling of a gas turbine blade, Journal of Engineering for Power 100 (1978) 476-481.

[8] D.G. Bogard, K.A. Thole, Gas turbine film cooling, Journal of Propulsion and Power 22 (2006) 249-270.

[9] S. Friedrichs, Endwall film cooling in axial flow turbines, University of Cambridge, 1997.

[10] L. Luo, C. Wang, L. Wang, B. Sunden, S. Wang, Endwall heat transfer and aerodynamic performance of bowed outlet guide vanes (OGVs) with on-and off-design conditions, Numerical Heat Transfer, Part A: Applications 69 (2016) 352-368.

[11] S. Lorenz, D. Mukomilow, W. Leiner, Distribution of the heat transfer coefficient in a channel with periodic transverse grooves, Experimental Thermal and Fluid Science 11 (1995) 234-242.

[12] T. Adachi, H. Uehara, Correlation between heat transfer and pressure drop in channels with periodically grooved parts, International Journal of Heat and Mass Transfer 44 (2001) 4333-4343.

[13] M. Greiner, P. Fischer, H. Tufo, Two-dimensional simulations of enhanced heat transfer in an intermittently grooved channel, ASME Journal of Heat Transfer 124 (2002) 538-545.

[14] A. Jaurker, J. Saini, B. Gandhi, Heat transfer and friction characteristics of rectangular solar air heater duct using rib-grooved artificial roughness, Solar Energy 80 (2006) 895-907.

[15] S. Eiamsa-Ard, P. Promvonge, Thermal characteristics of turbulent rib-grooved channel flows, International Communications in Heat and Mass Transfer 36 (2009) 705-711.

[16] D. Lorenzini-Gutierrez, A. Hernandez-Guerrero, J.L. Luviano-Ortiz, J.C. Leon-Conejo, Numerical and experimental analysis of heat transfer enhancement in a grooved channel with curved flow deflectors, Applied Thermal Engineering 75 (2015) 800-808.

[17] S. Skullong, P. Promvonge, C. Thianpong, M. Pimsarn, Thermal performance in solar air heater channel with combined wavy-groove and perforated-delta wing vortex generators, Applied Thermal Engineering 100 (2016) 611-620.

[18] N. Zheng, P. Liu, F. Shan, Z. Liu, W. Liu, Heat transfer enhancement in a novel internally grooved tube by generating longitudinal swirl flows with multi-vortexes, Applied Thermal Engineering 95 (2016) 421-432.

[19] C. Bi, G. Tang, W. Tao, Heat transfer enhancement in mini-channel heat sinks with dimples and cylindrical grooves, Applied Thermal Engineering 55 (2013) 121-132.

[20] K. Bilen, M. Cetin, H. Gul, T. Balta, The investigation of groove geometry effect on heat transfer for internally grooved tubes, Applied Thermal Engineering 29 (2009) 753-761.

[21] H.V. Moradi, J.M. Floryan, Maximization of heat transfer across micro-channels, International Journal of Heat and Mass Transfer 66 (2013) 517-530.

[22] M. Ahmed, N. Shuaib, M. Yusoff, A. Al-Falahi, Numerical investigations of flow and heat transfer enhancement in a corrugated channel using nanofluid, International Communications in Heat and Mass Transfer 38 (2011) 1368-1375.

[23] A.N. Al-Shamani, K. Sopian, H. Mohammed, S. Mat, M.H. Ruslan, A.M. Abed, Enhancement heat transfer characteristics in the channel with Trapezoidal rib–groove using nanofluids, Case Studies in Thermal Engineering 5 (2015) 48-58.

[24] Y.T. Yang, H.W. Tang, B.Y. Zeng, M.H. Jian, Numerical simulation and optimization of turbulent nanofluids in a three-dimensional arc rib-grooved channel, Numerical Heat Transfer, Part A: Applications 70 (2016) 831-846.

[25] J.Y. Qian, M.R. Chen, X.L. Liu, Z.J. Jin, A numerical investigation of the flow of nanofluids through a micro Tesla valve, Journal of Zhejiang University-SCIENCE A (2018).

[26] Y. Chen, Y.T. Chew, B.C. Khoo, Enhancement of heat transfer in turbulent channel flow over dimpled surface, International Journal of Heat and Mass Transfer 55 (2012) 8100-8121.

[27] J. Liu, G. Xie, T.W. Simon, Turbulent flow and heat transfer enhancement in rectangular channels with novel cylindrical grooves, International Journal of Heat and Mass Transfer 81 (2015) 563-577.

[28] L. Wang, M. Salewski, B. Sunden, A. Borg, H. Abrahamsson, Endwall convective heat transfer for bluff bodies, International Communications in Heat and Mass Transfer 39 (2012) 167-173.

[29] T. Praisner, C. Smith, The Dynamics of the Horseshoe Vortex and Associated Endwall Heat Transfer—Part I: Temporal Behavior, ASME Journal of Turbomachinery 128 (2006) 747-754.

[30] T. Praisner, C. Smith, The dynamics of the horseshoe vortex and associated endwall heat transfer—part II: time-mean results, ASME Journal of Turbomachinery 128 (2006) 755-762.

[31] M.B. Kang, K.A. Thole, Flowfield measurements in the endwall region of a stator vane, ASME 1999 International Gas Turbine and Aeroengine Congress and Exhibition, American Society of Mechanical Engineers, 1999, pp. V003T001A054-V003T001A054.

[32] M.B. Kang, A. Kohli, K.A. Thole, Heat transfer and flowfield measurements in the leading edge region of a stator vane endwall, ASME Journal of Turbomachinery 121 (1999) 558-568.

[33] D.H. Rhee, H.H. Cho, Effect of vane/blade relative position on heat transfer characteristics in a stationary turbine blade: Part 1. Tip and shroud, International Journal of Thermal Sciences 47 (2008) 1528-1543.

[34] D.H. Rhee, H.H. Cho, Effect of vane/blade relative position on heat transfer characteristics in a stationary turbine blade: Part 2. Blade surface, International Journal of Thermal Sciences 47 (2008) 1544-1554.

[35] I. Qureshi, A.D. Smith, T. Povey, Hp vane aerodynamics and heat transfer in the presence of aggressive inlet swirl, ASME Journal of Turbomachinery 135 (2013) paper No. 021040.

[36] Q. Zhang, L. He, A. Rawlinson, Effects of inlet turbulence and end-wall boundary layer on aerothermal performance of a transonic turbine blade tip, Journal of Engineering for Gas Turbines and Power 136 (2014) paper No. 052603.

[37] S.P. Lynch, K.A. Thole, Comparison of the three-dimensional boundary layer on flat versus contoured turbine endwalls, ASME Journal of Turbomachinery 138 (2016) paper No. 041008.

[38] J. Hjärne, V. Chernoray, J. Larsson, L. Löfdahl, An experimental investigation of secondary flows and loss development downstream of a highly loaded low pressure turbine outlet guide vane cascade, ASME paper GT2006-90561 (2006).

[39] J. Hjärne, V. Chernoray, J. Larsson, L. Löfdahl, Numerical validations of secondary flows and loss development downstream of a highly loaded low pressure turbine outlet guide vane cascade, ASME Turbo Expo 2007: Power for

Land, Sea, and Air, American Society of Mechanical Engineers, 2007, pp. 723-733.

[40] V. Chernoray, S. Ore, J. Larsson, Effect of geometry deviations on the aerodynamic performance of an outlet guide vane cascade, ASME Turbo Expo 2010: Power for Land, Sea, and Air, American Society of Mechanical Engineers, 2010, pp. 381-390.

[41] H. Koch, D. Kozulovic, M. Hoeger, Outlet Guide Vane Airfoil for Low Pressure Turbine Configurations, 42nd AIAA Fluid Dynamics Conference and Exhibit, 2012, pp. 2979.

[42] H. Chung, J.S. Park, S. Park, S.M. Choi, D.H. Rhee, H.H. Cho, Augmented heat transfer with intersecting rib in rectangular channels having different aspect ratios, International Journal of Heat and Mass Transfer 88 (2015) 357-367.

[43] S. Alfarawi, S. Abdel-Moneim, A. Bodalal, Experimental investigations of heat transfer enhancement from rectangular duct roughened by hybrid ribs, International Journal of Thermal Sciences 118 (2017) 123-138.

[44] S. Abraham, R.P. Vedula, Heat transfer and pressure drop measurements in a square cross-section converging channel with V and W rib turbulators, Experimental Thermal and Fluid Science 70 (2016) 208-219.

[45] W. Yang, S. Xue, Y. He, W. Li, Experimental study on the heat transfer characteristics of high blockage ribs channel, Experimental Thermal and Fluid Science 83 (2017) 248-259.

[46] P. Singh, J. Pandit, S.V. Ekkad, Characterization of heat transfer enhancement and frictional losses in a two-pass square duct featuring unique combinations of rib turbulators and cylindrical dimples, International Journal of Heat and Mass Transfer 106 (2017) 629-647.

[47] P. Singh, S. Ekkad, Experimental study of heat transfer augmentation in a two-pass channel featuring V-shaped ribs and cylindrical dimples, Applied Thermal Engineering 116 (2017) 205-216.

[48] L. Wang, B. Sunden, Experimental investigation of local heat transfer in a square duct with continuous and truncated ribs, Experimental Heat Transfer 18 (2005) 179-197.

[49] T.M. Liou, S.W. Chang, Y.A. Lan, S.P. Chan, Y.S. Liu, Heat transfer and flow characteristics of two-pass parallelogram channels with attached and detached transverse ribs, ASME Journal of Heat Transfer 139 (2017) paper No. 042001.

[50] A. Kumar, R. Chauhan, R. Kumar, T. Singh, M. Sethi, A. Sharma, Developing heat transfer and pressure loss in an air passage with multi discrete V-blockages, Experimental Thermal and Fluid Science 84 (2017) 266-278.

[51] T.M. Liou, S.H. Chen, Turbulent heat and fluid flow in a passage disturbed by detached perforated ribs of different heights, International Journal of Heat and Mass Transfer 41 (1998) 1795-1806.

[52] R. Kukreja, S. Lau, Distributions of local heat transfer coefficient on surfaces with solid and perforated ribs, Journal of Enhanced Heat Transfer 5 (1998) 9-21.

[53] O. Sara, T. Pekdemir, S. Yapici, M. Yilmaz, Heat-transfer enhancement in a channel flow with perforated rectangular blocks, International Journal of Heat and Fluid Flow 22 (2001) 509-518.

[54] J.M. Buchlin, Convective heat transfer in a channel with perforated ribs, International Journal of Thermal Sciences 41 (2002) 332-340.

[55] S. Chamoli, ANN and RSM approach for modeling and optimization of designing parameters for a V down perforated baffle roughened rectangular channel, Alexandria Engineering Journal 54 (2015) 429-446.

[56] D. Sahel, H. Ameur, R. Benzeguir, Y. Kamla, Enhancement of heat transfer in a rectangular channel with perforated baffles, Applied Thermal Engineering 101 (2016) 156-164.

[57] A. Hasanpour, M. Farhadi, K. Sedighi, Experimental heat transfer and pressure drop study on typical, perforated, V-cut and U-cut twisted tapes in a helically corrugated heat exchanger, International Communications in Heat and Mass Transfer 71 (2016) 126-136.

[58] A. Kumar, S. Chamoli, M. Kumar, S. Singh, Experimental investigation on thermal performance and fluid flow characteristics in circular cylindrical tube with circular perforated ring inserts, Experimental Thermal and Fluid Science 79 (2016) 168-174.

[59] R. Kumar, A. Kumar, R. Chauhan, R. Maithani, Comparative study of effect of various blockage arrangements on thermal hydraulic performance in a roughened air passage, Renewable and Sustainable Energy Reviews 81 (2018) 447-463.

[60] B. Sunden. A. Saidi, Numerical simulation of turbulent convective heat transfer in square ribbed ducts, Numerical Heat Transfer: Part A: Applications 38 (2000) 67-88.

[61] Y.L. Lin, T.P. Shih, M. Stephens, M. Chyu, A numerical study of flow and heat transfer in a smooth and ribbed U-duct with and without rotation, ASME Journal of Heat Transfer 123 (2001) 219-232.

[62] K. Wongcharee, W. Changcharoen, S. Eiamsa-ard, Numerical investigation of flow friction and heat transfer in a channel with various shaped ribs mounted on two opposite ribbed walls, International Journal of Chemical Reactor Engineering 9 (2011).

[63] D.H. Kim, B.J. Lee, J.S. Park, J.S. Kwak, J.T. Chung, Effects of inlet velocity profile on flow and heat transfer in the entrance region of a ribbed channel, International Journal of Heat and Mass Transfer 92 (2016) 838-849.

[64] T. Gao, J. Zhu, C. Liu, J. Xu, Numerical study of conjugate heat transfer of steam and air in high aspect ratio rectangular ribbed cooling channel, Journal of Mechanical Science and Technology 30 (2016) 1431-1442.

[65] L. Marocco, A. Franco, Direct numerical simulation and rans comparison of turbulent convective heat transfer in a staggered ribbed channel with high blockage, ASME Journal of Heat Transfer 139 (2017) paper No. 021701.

[66] B.V. Ravi, P. Singh, S.V. Ekkad, Numerical investigation of turbulent flow and heat transfer in two-pass ribbed channels, International Journal of Thermal Sciences 112 (2017) 31-43.

[67] N.Y. Alkhamis, A.P. Rallabandi, J.C. Han, Heat transfer and pressure drop correlations for square channels with V-shaped ribs at high Reynolds numbers, ASME Journal of Heat Transfer 133 (2011) paper No. 111901.

[68] S. Ekkad, J.C. Han, A review of hole geometry and coolant density effect on film cooling, ASME 2013 Heat Transfer Summer Conference collocated with the ASME 2013 7th International Conference on Energy Sustainability and the ASME 2013 11th International Conference on Fuel Cell Science, Engineering and Technology, American Society of Mechanical Engineers, 2013, pp. V003T020A003-V003T020A003.

[69] R.S. Bunker, A review of shaped hole turbine film-cooling technology, ASME Journal of Heat Transfer 127 (2005) 441-453.

[70] J.C. Han, S. Ekkad, Recent development in turbine blade film cooling, International Journal of Rotating Machinery 7 (2001) 21-40.

[71] K. Ghosh, R.J. Goldstein, Effect of inlet skew on heat/mass transfer from a simulated turbine blade, ASME 2011 Turbo Expo: Turbine Technical Conference and Exposition, American Society of Mechanical Engineers, 2011, pp. 1677-1687.

[72] C.C. Shiau, I. Sahin, N. Wang, J.C. Han, H. Xu, M. Fox, Turbine vane endwall film cooling comparison from five film-hole design patterns and three upstream leakage injection angles, ASME Turbo Expo 2018: Turbomachinery Technical Conference and Exposition, American Society of Mechanical Engineers, 2018, pp. V05CT19A005-V005CT019A005.

[73] A. Sinha, D. Bogard, M. Crawford, Film-cooling effectiveness downstream of a single row of holes with variable density ratio, ASME Journal of Turbomachinery 113 (1991) 442-449.

[74] W. Haas, W. Rodi, B. Schonung, The influence of density difference between hot and coolant gas on film cooling by a row of holes: predictions and experiments, ASME Journal of Turbomachinery 114 (1992) 747-755.

[75] P. Ligrani, J. Wigle, S. Jackson, Film-cooling from holes with compound angle orientations: part 2—results downstream of a single row of holes with 6d spanwise spacing, ASME Journal of Heat Transfer 116 (1994) 353-362.

[76] R. Goldstein, P. Jin, Film cooling downstream of a row of discrete holes with compound angle, ASME Turbo Expo 2000: Power for Land, Sea, and Air, American Society of Mechanical Engineers, 2000, pp. V003T001A054-V003T001A054.

[77] E. Lutum, B.V. Johnson, Influence of the hole length-to-diameter ratio on film cooling with cylindrical holes, ASME 1998 International Gas Turbine and Aeroengine Congress and Exhibition, American Society of Mechanical Engineers, 1998, pp. V004T009A001-V004T009A001.

[78] H.A. Zuniga, J.S. Kapat, Effect of increasing pitch-to-diameter ratio on the film cooling effectiveness of shaped and cylindrical holes embedded in trenches, ASME Turbo Expo 2009: Power for Land, Sea, and Air, American Society of Mechanical Engineers, 2009, pp. 863-872.

[79] W.F. Colban, K.A. Thole, D. Bogard, A film-cooling correlation for shaped holes on a flat-plate surface, ASME Journal of Turbomachinery 133 (2011) paper No. 011002.

[80] A.F. Chen, S.J. Li, J.C. Han, Film cooling for cylindrical and fan-shaped holes using pressure-sensitive paint measurement technique, Journal of Thermophysics and Heat Transfer 29 (2015) 775-784.

[81] M. Jabbari, R. Goldstein, Adiabatic wall temperature and heat transfer downstream of injection through two rows of holes, Journal of Engineering for Power 100 (1978) 303-307.

[82] B. Jubran, A. Brown, Film cooling from two rows of holes inclined in the streamwise and spanwise directions, Journal of Engineering for Gas Turbines and Power 107 (1985) 84-91.

[83] A. Sinha, D. Bogard, M. Crawford, Gas turbine film cooling: flowfield due to a second row of holes, ASME 1990 International Gas Turbine and Aeroengine Congress and Exposition, American Society of Mechanical Engineers, 1990, pp. V004T009A011-V004T009A011.

[84] P. Ligrani, J. Wigle, S. Ciriello, S. Jackson, Film cooling from holes with compound angle orientations: part 1—results downstream of two staggered rows of holes with 3d spanwise spacing, ASME Journal of Heat Transfer 116 (1994) 341-352.

[85] B. Jubran, B. Maiteh, Film cooling and heat transfer from a combination of two rows of simple and/or compound angle holes in inline and/or staggered configuration, Heat and Mass Transfer 34 (1999) 495-502.

[86] B. Jubran, A. Al-Hamadi, G. Theodoridis, Film cooling and heat transfer with air injection through two rows of compound angle holes, Heat and Mass Transfer 33 (1997) 93-100.

[87] J. Dittmar, A. Schulz, S. Wittig, Assessment of various film cooling configurations including shaped and compound angle holes based on large scale experiments, ASME Turbo Expo 2002: Power for Land, Sea, and Air, American Society of Mechanical Engineers, 2002, pp. 109-118.

[88] G. Natsui, Z. Little, J.S. Kapat, J.E. Dees, Adiabatic film cooling effectiveness measurements throughout multirow film cooling arrays, ASME Journal of Turbomachinery 139 (2017) paper No. 101008.

[89] D. Granser, T. Schulenberg, Prediction and measurement of film cooling effectiveness for a first-stage turbine vane shroud, ASME 1990 International Gas Turbine and Aeroengine Congress and Exposition, American Society of Mechanical Engineers, 1990, pp. V004T009A020-V004T009A020.

[90] S.W. Burd, T.W. Simon, Effects of Slot Bleed Injection Over a Contoured Endwall on Nozzle Guide Vane Cooling Performance: Part I—Flow Field Measurements, ASME Turbo Expo 2000: Power for Land, Sea, and Air, American Society of Mechanical Engineers, 2000, pp. V003T001A007-V003T001A007.

[91] R.A. Oke, T.W. Simon, S.W. Burd, R. Vahlberg, Measurements in a turbine cascade over a contoured endwall: discrete hole injection of bleed flow, ASME Turbo Expo 2000: Power for Land, Sea, and Air, American Society of Mechanical Engineers, 2000, pp. V003T001A022-V003T001A022.

[92] R. Oke, T. Simon, T. Shih, B. Zhu, Y.L. Lin, M. Chyu, Measurements over a film-cooled, contoured endwall with various coolant injection rates, ASME Turbo Expo 2001: Power for Land, Sea, and Air, American Society of Mechanical Engineers, 2001, pp. V003T001A025-V003T001A025.

[93] L.J. Zhang, R.S. Jaiswal, Turbine nozzle endwall film cooling study using pressure sensitive paint, ASME Turbo Expo 2001: Power for Land, Sea, and Air, American Society of Mechanical Engineers, 2001, pp. V003T001A030-V003T001A030.

[94] D. Knost, K. Thole, Adiabatic effectiveness measurements of endwall film-cooling for a first stage vane, ASME Turbo Expo 2004: Power for Land, Sea, and Air, American Society of Mechanical Engineers, 2004, pp. 353-362.

[95] C.C. Shiau, A.F. Chen, J.C. Han, S. Azad, C.P. Lee, Full-scale turbine vane endwall film-cooling effectiveness distribution using pressure-sensitive paint technique, ASME Journal of Turbomachinery 138 (2016) paper No. 051002.

[96] N. Sundaram, K. Thole, Bump and trench modifications to film-cooling holes at the vane-endwall junction, ASME Journal of Turbomachinery 130 (2008) paper No. 041013.

[97] N. Sundaram, K. Thole, Film-cooling flowfields with trenched holes on an endwall, ASME Journal of Turbomachinery 131 (2009) paper No. 041007.

[98] C. Tschierske, Non-conventional liquid crystals—the importance of micro-segregation for self-organisation, Journal of Materials Chemistry 8 (1998) 1485-1508.

[99] H. Schlichting, K. Gersten, E. Krause, H. Oertel, Boundary-layer Theory, Springer, 2016.

[100] J.H. Lienhard, A Heat Transfer Textbook, Courier Corporation, 2013.

[101] P. Spalart, W. Jou, M. Strelets, S. Allmaras, Comments on the feasibility of LES for wings, and on a hybrid RANS/LES approach, Advances in DNS/LES 1 (1997) 4-8.

[102] P. Sagaut, Large eddy simulation for incompressible flows: an introduction, Springer Science & Business Media, 2006.

[103] M.S. Gritskevich, A.V. Garbaruk, J. Schütze, F.R. Menter, Development of DDES and IDDES Formulations for the $k$-$\omega$ Shear Stress Transport Model, Flow, Turbulence and Combustion 88 (2012) 431-449.

[104] M.L. Shur, P.R. Spalart, M.K. Strelets, A.K. Travin, A hybrid RANS-LES approach with delayed-DES and wall-modelled LES capabilities, International Journal of Heat and Fluid Flow 29 (2008) 1638-1649.

[105] P.R. Spalart, S. Deck, M. Shur, K. Squires, M.K. Strelets, A. Travin, A new version of detached-eddy simulation, resistant to ambiguous grid densities, Theoretical and Computational Fluid Dynamics 20 (2006) 181-195.

[106] F.R. Menter, Two-equation eddy-viscosity turbulence models for engineering applications, AIAA Journal 32 (1994) 1598-1605.

[107] F. Menter, J.C. Ferreira, T. Esch, B. Konno, A. Germany, The SST turbulence model with improved wall treatment for heat transfer predictions in gas turbines, Proceedings of the International Gas Turbine Congress, 2003, pp. 2-7.

[108] S. Lynch, K. Thole, The effect of combustor-turbine interface gap leakage on the endwall heat transfer for a nozzle guide vane, ASME Journal of Turbomachinery 130 (2008) Paper No. 041019.

[109] D.G. Knost, Predictions and measurements of film cooling on the endwall of a first stage vane, Virginia Tech, Master thesis, 2003.

# Appended publications

## Author contribution

For all papers, the thesis author was responsible for developing the computational model, performing simulations, validating the model against experimental data, carrying out experiments as well as evaluation of data and analyzing the results as well as writing the draft papers. However, the experiments were carried out in close cooperation with another PhD student (mostly the second author). The co-authors assisted in planning, analysis and discussion and the main supervisor contributed most significantly to the revision of the papers.